INSTITUTO POLITECNICO NACIONAL

Centro de Investigación en Ciencia Aplicada y

Tecnología Avanzada Unidad Legaria

“CONTRIBUCIÓN A PRUEBAS NO DESTRUCTIVAS DE MATERIALES POR MEDIO DE TÉCNICAS FOTOTÉRMICAS”

TESIS

QUE PARA OBTENER EL GRADO DE

DOCTORADO EN TECNOLOGÍA AVANZADA

PRESENTA

ADRIAN FELIPE BEDOYA PÉREZ

CIUDAD DE MÉXICO. DICIEMBRE, 2019

INSTITUTO POLITECNICO NACIONAL

Centro de Investigación en Ciencia Aplicada y

Tecnología Avanzada Unidad Legaria

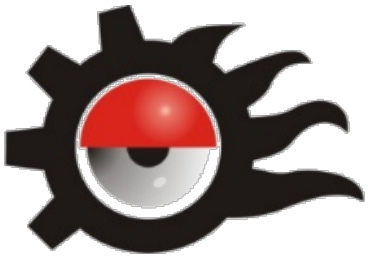

CICATA - IPN

“CONTRIBUTION TO NON-DESTRUCTIVE TESTING OF MATERIALS BY MEANS OF PHOTOTHERMAL TECHNIQUES”

THESIS

PRESENTED IN PARTIAL FULFILLMENT OF THE REQUIREMENTS

TO OBTAIN THE DEGREE OF

DOCTOR IN ADVANCED TECHNOLOGY

PRESENTED BY:

ADRIAN FELIPE BEDOYA PÉREZ

MEXICO CITY. DECEMBER 2019

UNIVERSIDAD DEL PAIS VASCO/ EUSKAL HERRIKO UNIBERTSITATEA

Escuela Técnica Superior de Ingeniería de Bilbao

“CONTRIBUTION TO NON-DESTRUCTIVE TESTING OF MATERIALS BY MEANS OF PHOTOTHERMAL TECHNIQUES”

THESIS

PRESENTED IN PARTIAL FULFILLMENT OF THE REQUIREMENTS TO OBTAIN THE DEGREE OF

DOCTOR IN PHYSICS

PRESENTED BY:

ADRIAN FELIPE BEDOYA PÉREZ

MEXICO CITY. DECEMBER 2019

RESUMEN

Este trabajo de tesis, estructurado en seis capítulos, engloba el uso y aplicaciones de algunas técnicas no-destructivas que involucran la generación y propagación de calor y la medición del campo de temperatura resultante en un medio. De aquí, en el primer capítulo se describen los fundamentos de la transferencia de calor, haciendo énfasis en las ecuaciones que rigen este fenómeno y los principales parámetros termofísicos involucrados. Entre estas ecuaciones pueden mencionarse la ley de Fourier, la de enfriamiento de Newton y la ley de Stefan-Boltzman que describen el flujo de calor en los mecanismos de conducción, convección y radiación, respectivamente, así como la ecuación de difusión de calor, que permite calcular el campo de temperatura en fenómenos no estacionarios y describir la dinámica de la transferencia de calor en un cuerpo. Esta ecuación puede escribirse como:

$$\frac{\partial^2 T}{\partial x^2}+\frac{\partial^2 T}{\partial y^2}+\frac{\partial^2 T}{\partial z^2}=\nabla^2 T=\frac{\rho c}{k}\frac{\partial T}{\partial t}=\frac{1}{\alpha}\frac{\partial T}{\partial t}$$

y es el pilar fundamental o el punto de partida de las teorías y técnicas que fueron usadas en este trabajo. En esta ecuación, *k* es la ***conductividad térmica*** que mide la habilidad de un cuerpo para conducir el calor, cuyas unidades son $Wm^{-1}K^{-1}$, α es la ***difusividad térmica*** que mide la tasa de propagación de calor a través del cuerpo, sus unidades son m^2s^{-1}, ρ es la densidad y c es el ***calor especifico*** ($JKg^{-1}K^{-1}$), definido como la cantidad de calor requerido para incrementar en un grado de temperatura una unidad de masa. En el caso particular en que un cuerpo homogéneo e isótropico semi-infinito es calentado periódica y uniformemente en su superficie por la absorción de un haz de luz monocromático de intensidad $I=\frac{1}{2}I_0(1+cos\,\omega t)$, la solución de la ecuación de difusión de calor en la dirección *x*, sujeta a una condición de flujo en la superficie, se puede expresar como:

$$T(x,t)=\frac{I_o}{2\sqrt{\rho ck\omega}}e^{-x\sqrt{\frac{\omega}{2\alpha}}}e^{j\left(\omega t-x\sqrt{\frac{\omega}{2\alpha}}-\pi/4\right)}=\frac{I_o}{2e\sqrt{\omega}}e^{-x\sqrt{\frac{\omega}{2\alpha}}}e^{j\left(\omega t-x\sqrt{\frac{\omega}{2\alpha}}-\pi/4\right)}$$

Esta ecuación representa la distribución de la temperatura a través del cuerpo en cualquier instante de tiempo en la dirección *x*. $e = \sqrt{\rho c k}$ es la ***efusividad térmica*** ($Ws^{1/2}m^{-2}K^{-1}$), que indica la habilidad del cuerpo para intercambiar calor o energía con el ambiente.

En este manuscrito los parámetros térmicos e, k y α fueron medidos en diferentes medios y usando diferentes técnicas cuyo potencial de aplicación está direccionado a los procesos de certificación y control de calidad en distintos campos de la industria.

En el segundo capítulo se describen las técnicas que fueron utilizadas, que son:

- La fotoacústica
- La fotopiroeléctrica
- La termografía infrarroja
- El método del alambre caliente transitorio.

El tercer capítulo tiene por objetivo medir las propiedades térmicas de mezclas liquidas de heptano/isooctano en función de su índice de octanaje (OI, por sus iniciales en inglés), que estima el rendimiento real auto-detonante del combustible en los motores modernos, así como la conductividad térmica de las componentes puras en fase gaseosa de algunos alcanos, con el fin de contribuir en las normas de certificación del índice de octanaje. Para esto, se midió la k a través del método del hilo caliente transitorio (Transient Hot Wire, THW) y la e por medio de la técnica fotopiroeléctrica frontal (Front Photopyroelectric, FPPE). Luego, α y $C = \rho c$ fueron calculadas utilizando las relaciones $\alpha = (k/e)^2$ y $C = e^2/k$, respectivamente, donde C es la capacidad calorífica por unidad de volumen. Se evaluó el comportamiento de los parámetros térmicos en función del IO considerando como valores limites el IO del heptano que es igual a 0 y del isooctano que es igual a 100. Se midieron diferentes mezclas de estos alcanos variando la fracción de masa del isooctano en heptano en 0, 20, 40, 60, 80 y 100 %, que además corresponden en número con el IO de cada mezcla. Las curvas obtenidas con los parámetros térmicos medidos y calculados para cada fracción de masa del isooctano en heptano demostraron la sensibilidad de los mismos a la detección de posibles asociaciones moleculares en las mezclas binarias de hidrocarburos líquidos.

También se muestra en este capítulo que la THW es adecuada para estudiar el efecto sobre la conductividad térmica de aire saturado con vapor de diferentes hidrocarburos (n-alcanos). Se muestra que existe una proporcionalidad entre la conductividad térmica de este vapor en función del número de átomos de carbono que componen la cadena molecular.

El objetivo del cuarto capítulo es medir la efusividad térmica y espectros de absorción óptica en el infrarrojo de muestras de aceite de café orgánico y convencional con el fin de encontrar posibles criterios de discriminación entre estos tipos de muestras. Los parámetros térmicos guardan una estrecha relación con las características morfo-anatómicas de un material de origen vegetal las cuales a su vez son parcialmente definidas por el proceso de producción agrícola al que es sometido. La efusividad térmica es un parámetro que ha sido usado para caracterizar la calidad de algunos alimentos. Por lo tanto, inicialmente se hizo un análisis del perfil de ácidos grasos mediante cromatografía de gases, así como un análisis físico-químico de densidad e índice de acidez para verificar la pureza del aceite extraído. Se utilizó la espectroscopia fotoacústica infrarroja por transformada de Fourier complementada con el análisis de componentes principales para identificar las posibles diferencias entre las intensidades de las bandas de absorción relacionadas con los grupos funcionales. Se midió la efusividad térmica usando la técnica FPPE, reconocida por su alta sensibilidad y precisión en la obtención de este parámetro. Se realizó una comparación entre las variables físicas de las muestras de aceite extraídas de granos de café orgánicos y convencionales, principalmente de la efusividad térmica soportada por los parámetros físico-químicos también obtenidos, lo que permitió observar ligeras diferencias entre estos tipos de muestras de aceite demostrando que este parámetro puede ser usado como un criterio de discriminación entre muestras de aceite extraído de café cultivado en diferentes tipos de agriculturas como son la convencional y la orgánica.

El quinto capítulo tiene por objetivo determinar el ancho de una interface o grieta entre dos medios diferentes a través de su resistencia térmica de contacto usando termografía infrarroja Lock-in con calentamiento puntual, así como la conductividad térmica de fluidos (gases y líquidos) que llenan la interface. Para ello, inicialmente se propuso una

expresión analítica para la temperatura superficial de los dos medios (de conductividad y difusividad térmica diferentes) cuando uno de ellos es iluminado por un láser enfocado y modulado en intensidad. Se realizó un análisis de cómo las conductividades térmicas de los dos medios afectan la sensibilidad para determinar la resistencia térmica de contacto, considerando un medio con valor de conductividad térmica superior e inferior respecto de la conductividad térmica del medio sobre el cual incide el haz del láser. Utilizando una cámara infrarroja, se obtuvieron los termogramas de amplitud y fase de la temperatura superficial de los dos medios con un espesor de interfaz calibrado. Ajustando un perfil de amplitud de temperatura a la expresión analítica fue posible obtener el valor de resistencia térmica de la interfaz. Este valor nos permitió encontrar el ancho de la interfaz utilizando la conocida relación $R_{th} = L/k_{aire}$, donde R_{th} es la resistencia térmica, L el espesor de la interfaz y k_{aire} es la conductividad térmica del aire. Los valores obtenidos coinciden con los valores nominales de la calibración validando la expresión analítica que se propone. Por otro lado, aprovechando la definición de R_{th}, se propone un método para medir la conductividad térmica de fluidos (gases y líquidos) contenidos en la interfaz. Inicialmente se hicieron simulaciones numéricas para evaluar la sensibilidad de la discontinuidad del campo de temperatura a la conductividad térmica del fluido que llena la interfaz entre dos materiales de iguales propiedades físicas, esto por simplicidad en el caso práctico. A través del análisis de sensibilidad se estableció un material ideal que permitiera hacer mediciones de conductividad térmica de fluidos que estuvieran en el rango de 0.01 a 1$Wm^{-1}K^{-1}$, rango en que se encuentra este parámetro en la mayoría de los fluidos. Se propuso una interfaz en forma de cuña para hacer las mediciones a diferentes espesores en un solo experimento, haciéndolo más eficiente y reduciendo el error experimental en comparación a una interfaz completamente paralela. El procedimiento experimental consistió en medir la R_{th} de la interfaz en cuña en diferentes puntos a lo largo de la misma (esto es, a diferentes espesores) mediante el método de termografía infrarroja Lock-in con calentamiento puntual a temperatura ambiente y presión atmosférica. Posteriormente los valores nominales del espesor son representados en función de la resistencia térmica en una curva L Vs. R_{th}, de la cual se obtiene una relación lineal cuya pendiente es el valor de la conductividad térmica del fluido (k_{fluido}) que llena la

interfaz. El método se comprobó llenando la interfaz con los fluidos: aire, etilenglicol y agua, que son regularmente usados como fluidos de calibración en otras técnicas de caracterización térmica. Los resultados obtenidos de conductividad térmica concuerdan con los valores reportados para estos fluidos validando el método.

Finalmente, el sexto capítulo de este manuscrito tiene por objetivo medir la difusividad térmica en el plano de muestras solidas en movimiento a velocidad constante usando termografía infrarroja. Esta dinámica de movimiento imita el caso de la producción en línea en fábricas en la que esta propiedad térmica podría ser utilizada como parámetro de control de calidad. El experimento consiste en calentar continuamente la muestra en movimiento con un láser puntual enfocado, que permanece en reposo, y registrar la temperatura de la superficie de la muestra mediante una cámara infrarroja. Se utilizó una expresión analítica para la temperatura superficial de la muestra en movimiento que involucra principalmente el parámetro de difusividad térmica de la muestra en las direcciones x y y. Considerando el estado estable, una velocidad constante de movimiento y el espacio de detección de la cámara infrarroja, se hicieron un conjunto de simulaciones numéricas para evaluar la forma del campo de temperatura superficial, los tiempos en los que se alcanza el estacionario y el comportamiento de los perfiles longitudinales y transversales a la dirección del movimiento. A partir de estas simulaciones se establecieron tres relaciones lineales simples cuyas pendientes son dependientes de la difusividad térmica en la dirección del movimiento de la muestra y en la dirección perpendicular a este, cada una de estas relaciones fueron establecidas independientemente y definidas como: El método de las parábolas, del perfil longitudinal y del perfil transversal. Estos tres métodos lineales tienen la ventaja de no verse afectados por las pérdidas de calor por convección y radiación, y son válidos tanto para muestras opacas como semitransparentes. Los métodos lineales permitieron establecer una relación dependiente de la velocidad para la longitud de difusión del calor a lo largo de las direcciones x y y. Se hicieron mediciones sobre un amplio conjunto de muestras de calibración evaluando diferentes regímenes de respuesta térmico y opacidad en materiales isótropos y uno anisótropo que confirmaron la validez de los métodos, que también son válidos cuando la muestra está en reposo y el láser escanea su superficie a velocidad constante.

En este manuscrito la ciencia aplicada es la principal protagonista y se centra en la aplicación de algunas técnicas no destructivas para la caracterización térmica. Estos métodos que surgen en los laboratorios de investigación buscan prosperar en aplicaciones prácticas en diferentes campos ya sea como innovaciones, nuevas tecnologías o como apoyo a los métodos ya estandarizados y regulados.

CONTENT

LIST OF FIGURES

ACKNOWLEDGEMENTS

To God for absolutely everything that has been accomplished to this day and for what is to come.

To my mother Danelly for all her support, company and constant effort in this stage and life. My strongest motivation.

To my brothers Cristian and Juan Pablo, and my third brother Felipe for always being there to listen and give advice.

To Javier, for his financial support when it was necessary.

To my advisors, Dr. Ernesto Marín and Dr. Arantza Mendioroz for their valuable friendship, support and advice.

To Dr. Agustín Salazar for his ample disposition, fundamental contributions and advice.

To Dr. Fernando Gordillo for his advice and joint work with GICADE.

To the excellent group of teachers and researchers of CICATA and the University of the Basque Country (UPV) who were always willing to provide advice, contribute ideas and laboratory work, among them: Dr. Antonio Calderón, Dr. Bruno Rojas, Dr. Salvador Alvarado, Dr. Alberto Oleaga, Dr. Enrique Cedeño, Dr. Kelly Martínez, Dr. Uriel Nogal, Dr. Yolanda Jiménez, Dr. Erich Von Borries and Dr. Nathaly Quiroz.

To my colleagues from the physics laboratory of CICATA and the photothermal techniques laboratory of the UPV, among them: Joan Jaime, Jorge Gonzales, Mateu Colom, Felix Rodriguez and Jeniffer Yeismar.

To all the human group of management staff of CICATA and the UPV for their collaboration, economic support and attention during all this time.

To CONACYT for the economic support of maintenance.

To the SIP-IPN and COFAA-IPN for the BEIFI scholarship and the economic support for the attendance to scientific events.

To my friends Hector, Lina and Melissa, always present.

To my friends in Bilbao: Nidia, Solangey and Orlando.

To the people who were there, and who were a fundamental part of my personal growth and academic formation.

And to all those who I have not mentioned but who were part of this life project and know that they are present in my life.

Many thanks to all of you.

ABSTRACT

This work is focused on the use of non-destructive techniques and methods that seek to contribute to specific applications for the industry and research fields, and it is composed of six chapters. Chapter one presents some theoretical fundaments and main concepts that are the basis of what is presented in this manuscript. Chapter two presents the principles of the methods and techniques used and their application. In the third chapter, measurements of the thermal transport properties of heptane/isooctane mixtures in the liquid phase at room temperature and atmospheric pressure were made showing the relationship between these properties and the octane number. The thermal effusivity and thermal conductivity were determined by the front photopyroelectric technique and the transient hot wire method, respectively. Then, the thermal diffusivity and the heat capacity per unit volume were calculated using the well-known relationships. The calculated thermal parameters proved to be sensitive to detect possible molecular associations in binary hydrocarbon liquid mixtures. It will also be shown in this chapter that the hot-wire technique is also suitable to study the effect on thermal conductivity of the diffusion of hydrocarbon vapor in air.

In the fourth chapter, oil samples extracted from organic and conventional coffee beans were studied in order to find a possible criterion for discrimination between these types of oil samples through the thermal effusivity, a parameter that was measured using the front photopyroelectric technique. A fatty acids profile analysis was done using gas chromatography as well as a physicochemical analysis of density and acidity index to verify the oil purity. Additionally, Mid-Infrared Fourier Transform Photoacoustic Spectroscopy aided by Principal Component Analysis was used to identify differences between the intensities of the absorption bands related to functional groups.

In the first part of the fifth chapter, a method is proposed to measure the thermal contact resistance at the vertical interface between two mediums or blocks using lock-in infrared thermography with laser spot heating. An analytical expression is proposed for the surface temperature of the two media when one of them is illuminated by a focused, intensity modulated laser. An analysis is done on how the thermal conductivities of the

two-media affect the sensitivity to determine the thermal contact resistance. Using an infrared camera, the amplitude and phase thermographs of the surface temperature of the two media with a calibrated interface thickness, were obtained. Fitting one particular temperature amplitude profile to the analytical expression it was possible to obtain the thermal resistance value of the interface. This value allowed us to find the width of the interface using the well-known relationship $R_{th}=L/k_{air}$. The values obtained were in agreement with the nominal values of calibration. Taking advantage of the R_{th} definition, in a second part of this chapter a method to measure the thermal conductivity of fluids (gases and liquids) is proposed, considering that the narrow interface between the two materials is filled by the fluid. The R_{th} is measured for different known thicknesses, L, of the fluid by lock-in infrared thermography. The thermal conductivity is obtained directly from the slope of the straight line L vs R_{th}. The method was tested by filling the interface with the fluids air, ethylene glycol and water. The results obtained agree very well with the values reported for these fluids.

Finally, in the sixth chapter an experimental setup is proposed based on infrared thermography to determine the in-plane thermal diffusivity of samples that are moving at constant velocity, imitating the case of in-line production in factories, in which this thermal property could be used like a quality control parameter. The experiment consists in heating the moving sample with a focused laser spot, which remains at rest, and recording the sample's surface temperature by an infrared camera. An analytical expression for the surface temperature of the moving sample has been obtained. Three simple linear relationships with slopes dependent on the thermal diffusivity in the direction of the sample movement and in the perpendicular direction were used. These three linear methods, which are not disturbed by heat losses by convection and radiation, are valid for both opaque and semitransparent samples. Measurements performed on calibrated samples confirm the validity of the methods, which are also valid when the sample is at rest and the laser spot scans its surface at constant velocity.

INTRODUCTION

The present work was done towards obtaining the PhD degree in *Advanced Technology* by the **Centro de Investigación en Ciencia Aplicada y Tecnología Avanzada (CICATA)-IPN**, Mexico City-Mexico, and the PhD degree in *Physics* by the **Universidad del País Vasco (UPV/EHU)**, Bilbao-Spain. Two of the eight study semesters were spent at the UPV/EHU and the other six at CICATA, within the frame of a collaborative research program between both institutions. Applied science is the main protagonist of this thesis, whose goal is mainly focused on demonstrating the possibilities of different photothermal techniques to perform non-destructive characterization of samples in different fields of research and industry.

Non-destructive testing is very attractive in various fields of application because it uses methods and techniques that do not permanently affect the physical, mechanical, geometric and chemical properties of the material being tested. In other words, when the inspection, testing or evaluation process is completed the investigated material can still be used for the purpose for which it was made, unlike methods that are destructive in nature, and therefore testing is done on selected samples rather than the required one [1].

The hierarchical map shown below synthetizes the techniques used in this work and the applications for which they were applied in each chapter.

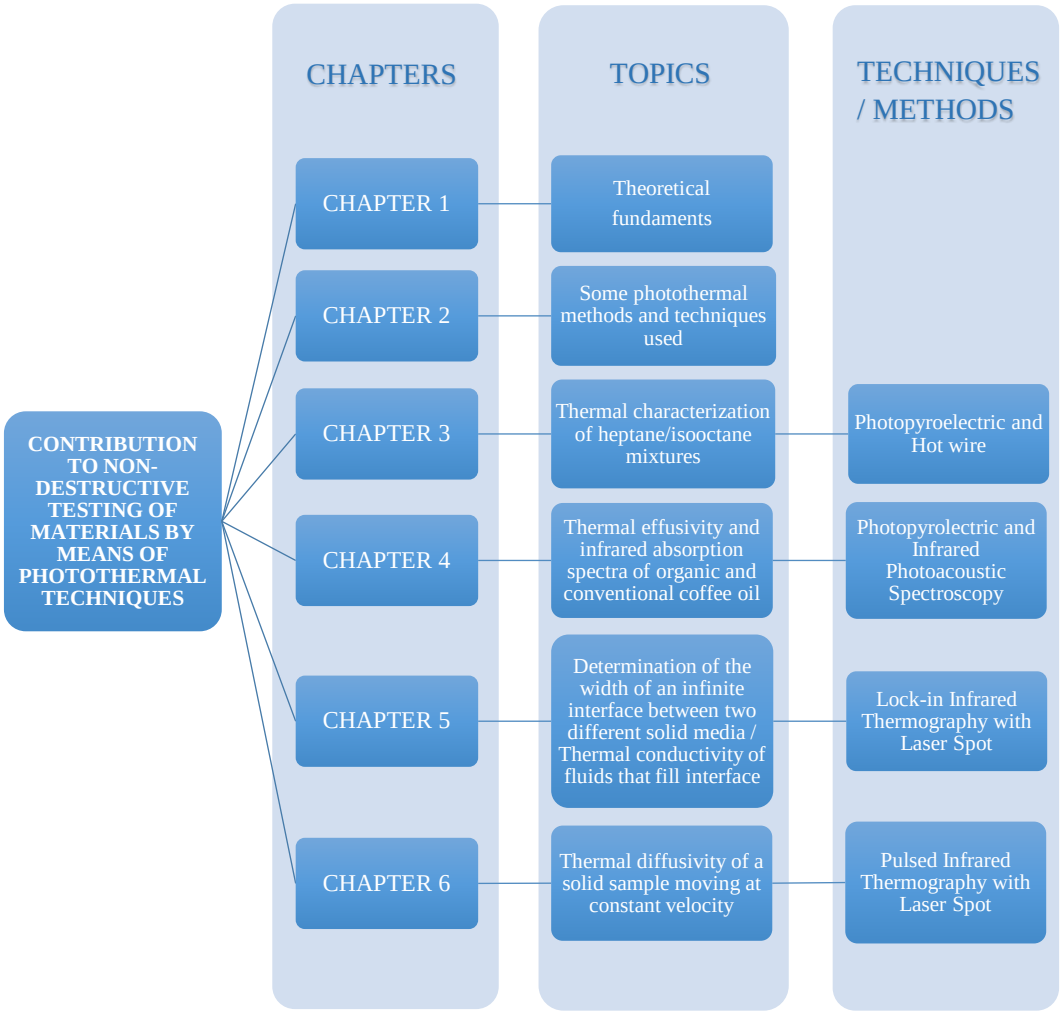

The scientific products of this thesis are:

Research articles:

1. A. Bedoya, S. Alvarado, A. Calderón, E. Marín, “Thermal transport properties of heptane-isooctane mixtures”. **Thermochimica Acta** 666, pp 190-196, 2018. **Q1** DOI: https://doi.org/10.1016/j.tca.2018.07.003 (PART OF THE CONTENT OF CHAPTER 3)

2. A. Bedoya, F. Gordillo-Delgado, Y.E. Cruz-Santillana, J. Plazas, E. Marin, “Thermal effusivity measurement of conventional and organic coffee oils via

photopyroelectric technique". **Food Research International**, 102, pp 419-424, 2017. **Q1** DOI: https://doi.org/10.1016/j.foodres.2017.09.013 (PART OF THE CONTENT OF CHAPTER 4)

3. J. González, A. Bedoya, A. Mendioroz and A. Salazar, "Measuring the thermal resistance of vertical interfaces separating two different media using lock-in infrared thermography with laser spot heating". **International Journal of Thermal Sciences** 135, pp 410-416, 2018. **Q1** DOI: https://doi.org/10.1016/j.ijthermalsci.2018.09.026 (PART OF THE CONTENT OF CHAPTER 5)

4. A. Bedoya, J. González, A. Mendioroz and A. Salazar, "Measuring the thermal resistance of vertical interfaces separating two different media using lock-in infrared thermography with laser spot excitation". **QIRT 2018 Proceedings**, pp 806-807, 2018. DOI: https://doi.org/10.21611/qirt.2018.100 (PART OF THE CONTENT OF CHAPTER 5)

5. A. Bedoya, J. González, J. Rodríguez-Aseguinolaza, A. Mendioroz, A. Sommier, J.C. Batsale and C. Pradere, A. Salazar, "Measurement of in-plane thermal diffusivity of solids moving at constant velocity using laser spot infrared thermography". **Measurement** 134, pp 519-526, 2018. **Q1** DOI: https://doi.org/10.1016/j.measurement.2018.11.013 (PART OF THE CONTENT OF CHAPTER 6)

6. L. Gaverina, M. Bensalem, A. Bedoya, J. Gonzalez, A. Sommier, J.L. Battaglia, A. Salazar, A. Mendioroz, A. Oleaga, J. C. Batsale, C. Pradere, "Constant Velocity Flying Spot for the estimation of in-plane thermal diffusivity in anisotropic materials". **International Journal of Thermal Science** 145, pp 1-13, 2019. **Q1** DOI: https://doi.org/10.1016/j.ijthermalsci.2019.106000 (PART OF THE CONTENT OF CHAPTER 6)

7. A. Bedoya J. Gonzalez, A. Mendioroz, C. Pradere, A. Sommier, J.C. Batsale, A. Salazar, "Flying-spot thermography: measuring the in-plane (an)isotropic thermal diffusivity of large and complex parts". **Proceedings Thermosense:**

Thermal Infrared Applications XLI 11004, 2019. DOI: https://doi.org/10.1117/12.2518623 (PART OF THE CONTENT OF CHAPTER 6)

8. A. Bedoya, M. Colom, A. Mendioroz, A. Salazar, E. Marín, “Measurement of the thermal conductivity of fluids using laser spot lock-in thermography”. **Measurement (submitted for publication)** (PART OF THE CONTENT OF CHAPTER 5)

9. M. Colom, A. Bedoya, A. Mendioroz, A. Salazar, “Measuring the in-plane thermal diffusivity of moving samples using laser spot lock-in thermography”. **International Journal of Thermal Science**. **(submitted for publication)** (PART OF THE CONTENT OF CHAPTER 6)

GENERAL OBJECTIVE

To demonstrate that photothermal methods such as the photoacoustic, the photopyroelectric and the IR thermography techniques are suitable for non-destructive characterization of materials in applications related to certification and quality control of products.

PARTICULAR OBJECTIVES

- To measure the thermal properties of heptane/isooctane mixtures in the liquid as a function of its octane number, as well as the gas phases of the pure components, in order to achieve certification rules for octane number rating.
- To measure the thermal effusivity and optical absorption spectra in the IR of organic and conventional coffee oil samples in order to find a possible criterion for discrimination between these types of oil samples using photothermal techniques.
- To determine the width at the vertical interface or crack between two different media using LIT with laser spot heating through its thermal contact resistance, as well as the thermal conductivity of fluids (gases and liquids) than fill the narrow interface.
- To measure the in-plane thermal diffusivity of solid samples in motion at constant velocity using infrared thermography.

CHAPTER 1

THEORETICAL FUNDAMENTALS

This chapter shows the fundamental concepts behind this work. It gives a brief description of the heat transfer mechanisms by conduction, convection and radiation, as well as the equation of heat diffusion and the thermophysical parameters involved in it.

1.1 About heat transfer

Heat transfer can be defined as energy in transit due to a temperature difference. [2]. This process always occurs from the hottest to the coldest region and stops when both reach an equilibrium temperature. There are three heat transfer mechanisms, namely conduction, convection, and radiation, which are described by Fourier's law, Newton's cooling law (for natural convection), and Stefan-Boltzman's law, respectively. A combination of these heat transfer mechanisms may even be present in one medium [3].

1.2 Heat transfer by the conduction mechanism

When there is a temperature difference in a body a transfer of energy is generated from the most energetic particles to the adjacent less energetic ones, product of their interactions. Conduction takes place in different phases of a substance, in solids, liquids and gases. In the last two it is due to collisions and the diffusion of molecules during their movement and in solids it is mainly due to the vibration of atoms and molecules in the crystalline network or to the movement of electric charge carriers [3], e.g. electrons. The way to quantify this heat transfer mechanism was proposed empirically by mathematician Joseph Fourier in 1822 in his book *Théorie Analytique de la Chaleur* [4]. He proposed a law that bears his name *Fourier's law*, which states that the heat flux per unit area or heat flux density [Wm^{-2}] resulting from thermal conduction is proportional to the magnitude of the temperature gradient and opposite to it in sign. If we call the constant of proportionality, *k*, then

$$q_{cond} = -k\frac{dT}{dx} \qquad [\mathrm{Wm^{-2}}] \tag{1.1}$$

where *k* is called ***Thermal Conductivity*** and is a measure of a material's ability to conduct heat. Its units are $\mathrm{Wm^{-1}K^{-1}}$. This transport parameter takes a characteristic value for each material. Equation 1.1 tell us that if the temperature decreases with *x*, *q* will be positive-it will flow in the *x*-direction. If *T* increases with *x*, *q* will be negative-it will flow opposite the *x*-direction. Equation 1.1 is the one-dimensional form of Fourier's law[5].

For one-dimensional steady state conduction in extended samples of homogeneous and isotropic materials and for small temperature gradients, Fourier's law can be integrated in each direction to its potential form. In rectangular coordinates it reads:

$$q_{cond} = k\frac{T_2 - T_1}{x_2 - x_1} = \frac{k}{L}\Delta T = \frac{\Delta T}{R_{th}} = h_{cond}\Delta T \tag{1.2}$$

(the signus minus was eliminated because only the magnitude of the heat flux density was considered here). Here T_1 and T_2 represent two planar isotherms at positions x_1 and x_2, respectively, with $L = x_2 - x_1$, and R_{th} is called the ***thermal resistance***. The parameter $h_{cond} = {}^{k}/_{L} = 1/R_{th}$ has been incorporated as the *Conduction Heat Transfer coefficient*.

1.3 Heat transfer by the convective mechanism

Consider a cool gas flows past a warm body. The fluid immediately adjacent to the body forms a thin slowed-down region called a boundary layer. Heat is conducted into this layer, which sweeps it away and, farther downstream, mixes it into the stream. We call such processes of carrying heat away by a moving fluid convection. Thus, convection is the transfer of energy between a solid surface and an adjacent moving fluid. In the absence of any massive movement of fluid, the heat transfer that occurs is by conduction only. In 1701, Isaac Newton considered the convective process and suggested that the cooling would such that

$$\frac{dT_b}{dt} \propto T_b - T_\infty \tag{1.3}$$

where T_b is the body temperature and T_∞ that of the oncoming fluid. This statement suggests that energy is flowing from the body. But if the energy of the body is constantly replenished, the body temperature need not change, then the heat flux will be

$$Q \propto T_b - T_\infty \qquad [\mathrm{W}] \tag{1.4}$$

This equation can be rewritten in terms of $q = Q/A$ as

$$q_{conv} = h_{conv}(T_b - T_\infty) \qquad [\mathrm{Wm^{-2}}] \tag{1.5}$$

This is the steady-state form of *Newton's Law* of cooling, as it is usually quoted [5]. The constant h_{conv} is the *Convective Heat Transfer Coefficient* and is a parameter that is determined experimentally, whose value depends on all the variables that influence convection, such as the geometric configuration at the surface, the nature of the movement of the fluid, its properties and its massive velocity.

1.4 Heat transfer by the radiation mechanism

Thermal radiation is the energy emitted by matter at a finite temperature. Regardless of the state of matter, radiation can be attributed to the accelerated motion of charged particles of constituent atoms or molecules. The energy of the radiation field is transported by electromagnetic waves (photons). The energy flux depends upon the temperature of the body and the nature of its surface. While the transfer of energy by conduction or convection requires the presence of a material medium, radiation doesn't. In fact, radiation transfer occurs more efficiently in the vacuum [2]. Thermal radiation occurs in a range of the electromagnetic spectrum between 0.1 to 1000 μm.

Black bodies. The black body or perfect thermal radiator is a body which absorbs all energy that reaches it and reflects nothing, but this is only an idealization, in nature there are no perfect black bodies. Suppose that a radiant heat flux density, q_{rad}, falls upon a translucent plate that is not black. A fraction A_b, called *Absorptance*, is absorbed in the body; a fraction *R*, called the *Reflectance*, is reflected from it; and a fraction *T*, called the *Transmittance*, passes through. Thus, neglecting re-emission of energy from a body by means of fluorescence or other similar process,

$$1 = A_b + R + T \tag{1.6}$$

This equation is valid for radiation of all wavelengths at any temperature:

$$1 = A_{b\lambda} + R_\lambda + T_\lambda \tag{1.7}$$

If all radiant energy incident on a black body is absorbed, then $A_b = 1$ and $R_b = T_b = 0$. Furthermore, the energy flux density emitted from a black body reaches a theoretical maximum, which is given by the *Stefan-Boltzmann law* that represents the flux of energy radiated from a black body as:

$$q_b(T) = \sigma T^4 \tag{1.8}$$

This law was established experimentally by Stefan in 1879 and explained by Boltzmann on the basis of thermodynamics arguments in 1884. Here the *Stefan-Boltzmann constant*, σ, is 5.670400x10^{-8} W/m^{2}K^4, and T is the absolute temperature. Likewise, non-black bodies emit less radiation than black bodies. Therefore, the heat flux density emitted by a real surface is less than that emitted by a black body at the same temperature, given by

$$q_{rad} = \varepsilon\sigma T^4 \tag{1.9}$$

where ε is a radiative property at the surface called *Emissivity*, with values in the range of $0 < \varepsilon \leq 1$ and is a dimensionless parameter [5].

Radiant heat exchange. Suppose a continuous energy exchange between a body of emissivity ε and temperature T_b, and an isothermal surface that surrounds it with temperature T_m. Here the radiation heat flow density is given by

$$q_{rad} = \varepsilon\sigma(T_b^4 - T_m^4) \tag{1.10}$$

but the non-linearity of the equation presented is not very convenient to manipulate in heat transfer problems. Therefore, if small differences are assumed between the body and the medium, a Taylor series expansion around the temperature of the medium allows to obtain a linear relationship of the form:

$$q_{rad} = 4\varepsilon\sigma T_b^3(T_b - T_m) = h_{rad}(T_b - T_m) \tag{1.11}$$

where h_{rad} is defined as *Radiation Heat Transfer Coefficient* [6].

1.5 Thermal contact resistance

In the event that two perfectly smooth surfaces are brought into contact, an ideal contact will occur at each point of both surfaces, in the ideal case, but in reality this assumption is not easy to achieve experimentally because even the smoothest surfaces end up being rough when examined microscopically encountering a numberless number of valleys and peaks as shown schematically in Figure 1.1.

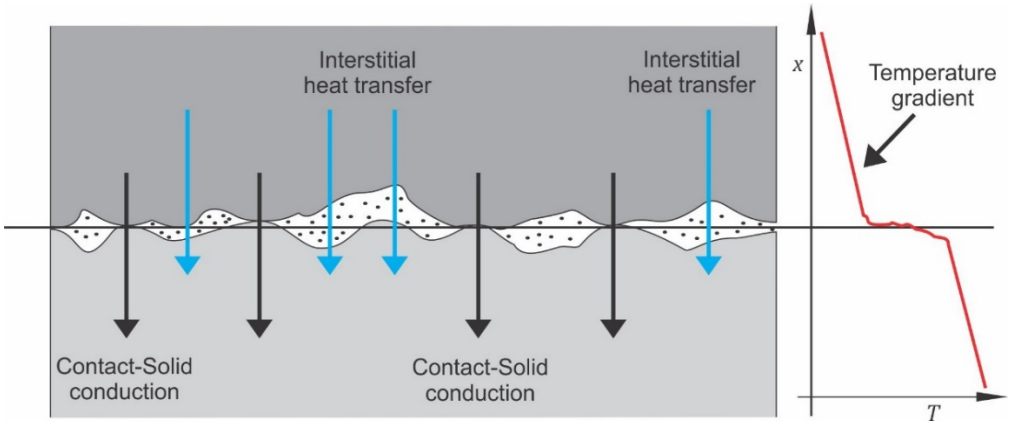

Figure 1.1 Contact Interface between two solids surfaces. Example of microscopic view.

By joining the two surfaces through compression, the peaks will form a good contact between the surfaces of the materials used, while the valleys will form air voids that can be seen as thermal insulation regions due to the low conductivity of this gas. Hence an interface between the materials is considered, and it offers some resistance to heat transfer. Thermal radiation across the gaps is inefficient. This resistance per unit area of the interface is known as ***Thermal Contact Resistance***, R_{th}. The heat transfer through the interface can be expressed by analogy to Newton's law, as

$$q_{int} = h_{th}\Delta T_{int} \tag{1.12}$$

where ΔT_{int} is the effective temperature difference at the interface. The parameter h_{th}, is the *interfacial Conductance* and can be expressed as,

$$h_{th} = \frac{q_{int}}{\Delta T_{int}} \tag{1.13}$$

and it's related to the R_{th} by

$$R_{th} = \frac{1}{h_{th}} = \frac{L}{k} \qquad [m^2KW^{-1}] \tag{1.14}$$

where L is the average gap width in the points (if known) of non-contact between the two surfaces, and k is the thermal conductivity of the air in this case. Note that R_{th} represents the thermal contact resistance per unit area. The thermal resistance for the entire interface is obtained by dividing R_{th} by the apparent area of that interface [3,5].

1.6 Heat diffusion equation

To establish the analytical expression governing heat transfer in a body subject to non-stationary heating or cooling, Fourier's law must be combined with the energy conservation law or heat flux balance, bearing in mind that temperature will depend on both spatial and time coordinates. Therefore, considering a body with isotropic thermal conductivity and assuming that there is no heat generation inside, we have in Cartesian coordinates the following expression,

$$\frac{\partial^2 T}{\partial x^2} + \frac{\partial^2 T}{\partial y^2} + \frac{\partial^2 T}{\partial z^2} = \nabla^2 T = \frac{\rho c}{k}\frac{\partial T}{\partial t} = \frac{1}{\alpha}\frac{\partial T}{\partial t} \tag{1.15}$$

This equation is known as the heat diffusion equation or the second Fourier equation; where $\alpha = k/\rho c$ is the ***thermal diffusivity***, which has units of m^2s^{-1}, and is defined as a rate of heat propagation through the body. It is also a thermal parameter of its own that is related to its thermal conductivity, ***specific heat*** (c, $JKg^{-1}K^{-1}$) and *density* (ρ, Kgm^{-3}). The specific heat is the amount of heat required to increase the temperature of a unit mass of substance by one degree. In particular, for the one-dimensional case where the heat flow is only in the x-direction, Equation 1.15 is rewritten as:

$$\frac{\partial^2 T}{\partial x^2} - \frac{1}{\alpha}\frac{\partial T}{\partial t} = 0 \tag{1.16}$$

Considering a semi-infinite solid subjected on the surface to heating by a monochromatic light beam of modulated intensity I:

$$I = \frac{1}{2} I_0 (1 + cos\, \omega t) \tag{1.17}$$

where I_0 is the intensity of light; $\omega=2\pi f$ is the angular modulation frequency and t the time; and considering that light is absorbed in its totality by the solid, the condition of continuity of flux on the surface will be:

$$-k\frac{dT}{dx}|_{x=0} = Re\left[\frac{I_o}{2}e^{j\omega t}\right] \tag{1.18}$$

Applying this condition, the solution of the one-dimensional diffusion equation is

$$T(x,t) = \frac{I_o}{2\sqrt{\rho ck\omega}}e^{-x/\mu}e^{j(\omega t - x/\mu - \pi/4)} \tag{1.19}$$

in which $\mu = (\alpha/\pi f)^{1/2}$, called ***Thermal diffusion length***, is the distance at which the wavelength decays 63% or e times from its initial value on the surface [7]. Equation 1.19 is often called a *thermal-wave*. In steady state, leaving aside the harmonic temporal dependence of T, this equation depends only on the spatial coordinate x. The amplitude and phase, considering the concept of the phasor, can be written as follows,

$$Amplitude\ (T(x)) = \frac{I_o}{2\sqrt{\rho ck\omega}}e^{-x/\mu} = \frac{I_o}{2e\sqrt{\omega}}e^{-x/\mu} \tag{1.20}$$

$$Phase\ (T(x)) = e^{-j(x/\mu + \pi/4)} \tag{1.21}$$

where $e = \sqrt{\rho ck}$ is denoted as ***thermal effusivity***, whose units are. Thermal effusivity describes a body's ability to exchange heat or energy with the environment [8,9,10]. Note that $\lambda_{tw} = 2\pi\mu$ is the wavelength of the thermal wave, so that the thermal wave is fully damped within one thermal wavelength. From Equation 1.19, if the temperature is measured as a function of frequency at a given distance from the sample´s surface, it is possible to determine the thermal diffusivity of the material. On the other hand, measurement of the surface temperature allows the thermal effusivity determination.

Another solution to the diffusion equation of particular interest in photothermal studies is the response to a short excitation pulse, from which, information about the thermal diffusivity of the material is obtained. It consists of heating the sample surface for a short time (milliseconds) with a high power (kW) and then monitoring the cooling process of the heated surface. Then, considering a semi-infinite, homogeneous and

isotropic sample which is affected by a pulse Dirac delta $\delta_{(t)}$, of energy density Q_0 (Jm^{-2}), the flow continuity condition can be written as:

$$-k\frac{dT}{dx}|_{x=0} = Q_0\delta_{(t)} \tag{1.22}$$

Under this condition the solution to Equation 1.16 has an analytical solution, in which the evolution of the temperature after the pulse can be expressed as,

$$T(x,t) = \frac{Q_o}{e\sqrt{t\pi}}e^{-x^2/\mu^2} \tag{1.23}$$

where $\mu = \sqrt{4\alpha t}$, is a measure of the depth of heat diffused into the sample at time *t* [11,6].

It is important to mention that in the photothermal experiments the amplitude of the thermal wave is often of a few mK, otherwise heating can affect the values of the parameters to be measured. Due to these small values, photothermal signals are often very polluted buy noise. Therefore, a technique to extract useful information from a very noisy environment is necessary for data acquisition: Lock-in synchronous or phase-sensitive detection.

1.7 Phase-Sensitive Detection

It is a process by means of which it is possible to recover a digital signal oscillating in time at a given frequency and that is in an environment of very low signal-to-noise ratio, rejecting any other signal that has a different frequency than the one of interest. Basically, in this process two signals are involved: the signal with the information and a reference signal (at the frequency of interest), both generally sinusoidal. This process is the basis for the operation of a Lock-in Amplifier. A trigonometric analysis of the signals shows how this signal recovery process works.

Suppose the input signal with the information has the form [12]:

$$S(t) = S\sin(\omega t + \varphi_s) \tag{1.24}$$

where S is the signal amplitude, φ is the phase. Furthermore, considering a reference signal that oscillates at the frequency of interest ω_r and a signal with a phase difference of $\pi/2$ with respect to the mentioned reference, respectively,

$$S_r(t) = S_r \sin(\omega_r t + \varphi_r) \tag{1.25}$$

$$S_r'(t) = S_r \cos(\omega_r t + \varphi_r) \tag{1.26}$$

and multiplying the Equation 1.24 by 1.25 and 1.26, we have

$$S_p(t) = S(t) * S_r(t) \tag{1.27}$$

$$S_p'(t) = S(t) * S_r'(t) \tag{1.28}$$

Now applying some trigonometric identities, you finally get it:

$$S_p(t) = \frac{S*S_r}{2}\cos([\omega - \omega_r]t + \varphi_s - \varphi_r) - \frac{S*S_r}{2}\cos([\omega + \omega_r]t + \varphi_s + \varphi_r) \tag{1.29}$$

$$S_p'(t) = \frac{S*S_r'}{2}\sin([\omega + \omega_r]t + \varphi_s + \varphi_r) - \frac{S*S_r'}{2}\sin([\omega - \omega_r]t + \varphi_s - \varphi_r) \tag{1.30}$$

The diagram in Figure 1.2 represents how this process is done, considering passive electronic elements that allow the introduction of phase shifts and the filtering of signals.

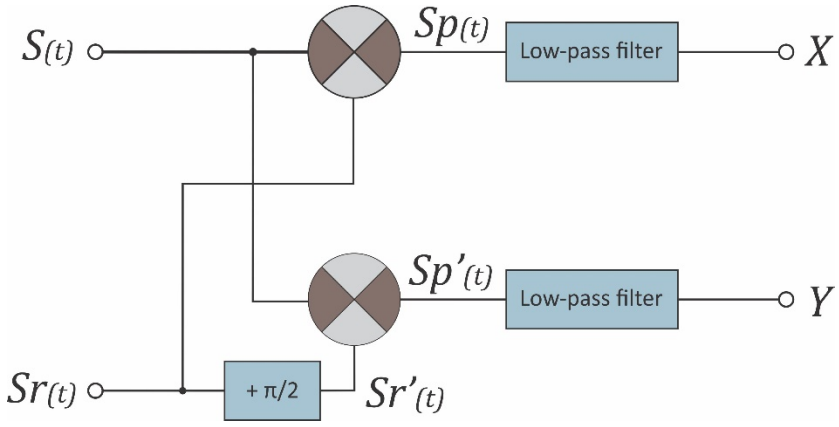

Figure 1.2 General scheme of Phase-Sensitive Detection method.

If we consider $\omega_r = \omega$, then the difference in the components in the Equations 1.29 and 1.30 will be a DC component. In addition, in the scheme a low-pass filter eliminates the higher frequency components, therefore, we could represent the signals as:

$$S_p(t) = \frac{S*S_r}{2}\cos(\varphi_s - \varphi_r) \sim S\cos(\varphi) = X \tag{1.31}$$

$$S_p{}'(t) = \frac{S*S_r{}'}{2}\sin(\varphi_s - \varphi_r) \sim S\sin(\varphi) = Y \tag{1.32}$$

Now you have two outputs, one that is proportional to the $\cos\varphi$ and the other to the $\sin\varphi$, which can be named *X* and *Y*, respectively. These two quantities represent the signal as a vector relative to the lock-in reference oscillator. *X* is called the component in phase and *Y* the component in quadrature, from which the amplitude of the resulting signal can be obtained as well as phase, as follows,

$$Amplitude = \sqrt{X^2 + Y^2} \tag{1.33}$$

$$Phase = \tan^{-1}\left(\frac{Y}{X}\right) \tag{1.34}$$

CHAPTER 2

SOME USED PHOTOTHERMAL METHODS AND TECHNIQUES

There is a universe of experimental techniques aimed at measuring thermal properties of materials, among which we can mention the photothermal methods, which are generally non-destructive and non-invasive, a particularity that makes them very attractive. These techniques offer high sensitivity for the determination of optical and thermal properties of materials, among others. They are based in a common principle of generating and detecting thermal waves, but they differ in the way of generation and detection. In this chapter the four photothermal techniques used in this work will be described, namely the photoacoustic, the front photopyroelectric method and two variants of active infrared thermography. One non-photothermal method, the hot wire technique, was also used, so that it will be described too. The mathematics involved in each case, as well as the experimental schemes that have been implemented for the development of this investigation, will be briefly discussed.

2.1 Photoacoustic Technique

This technique is based on the photoacoustic effect which was discovered in 1880 by Alexander Graham Bell [13]. This consists in the generation of an acoustic signal due to the heating of a body by the absorption of light. One of the modalities of the technique, widely used for thermal and optical characterization of materials uses a light beam modulated in intensity to generate a periodic heat flow through of the sample, which produces pressure changes in the adjacent gas through a mechanical expansion-contraction effect of the later. A basic experimental arrangement of the photoacoustic technique (PAT) based on this principle is schematically shown in Figure 2.1. In this configuration the sample is inside a sealed cell containing air or other gas. The intensity modulated beam of light impinges on a sample and generates the PA signal that is detected by a microphone already enclosed in the cell.

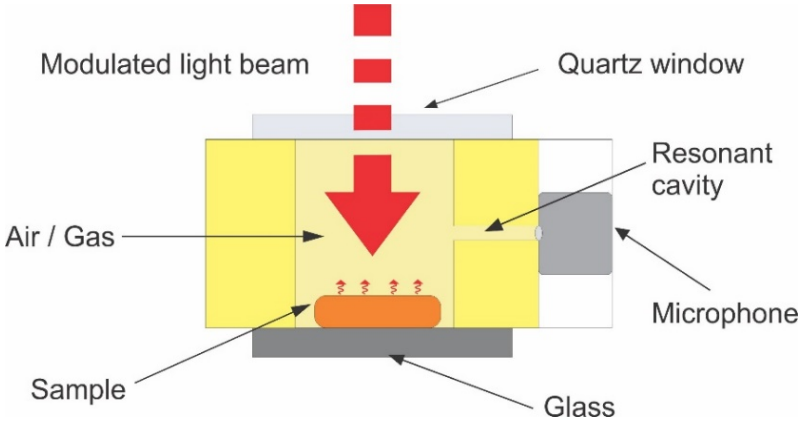

Figure 2.1 Schematic of a Closed Photoacoustic Cell.

Rosencwaig-Gersho model. The theory describing the signal obtained from the photoacoustic effect was enunciated in 1976 by Rosencwaig and Gersho and is known as the heat diffusion or the RG model [14]. It is based on the assumption that periodic heating of the surface of a sample results in a flow of heat through the sample to a gas contained in a closed cell. This model considers the one-dimensional heat flow in the airtight cell and demonstrates that only a relatively thin layer of air inside it, adjacent to the surface of the solid (sample) and of thickness equal to one thermal wave wavelength ($2\pi\mu_g$) in the gas, thermally responds to the periodic heat flow from it. This air layer is heated and cooled alternately, behaving like a vibrating piston, so that pressure changes generate an acoustic signal.

A microphone detects the average pressure generated in the cell. The sample of thickness l_s (Figure 2.2) is located in such a way that its front surface is exposed to the gas (air) inside the cell and its rear side is in contact with a backing of thickness l_b. The length of the gas column, l_g, is given by $l_g=L-l_s-l_b$, where L is the whole cell length. It is assumed that the gas and the backing material do not absorb light. The subscript i represents the solid (s), the gas (g) and the backing material (b); $\omega = 2\pi f$ denotes the angular modulation frequency of the incident light beam and its intensity is given by $I = I_0 Re(1 + e^{i\omega t})$.

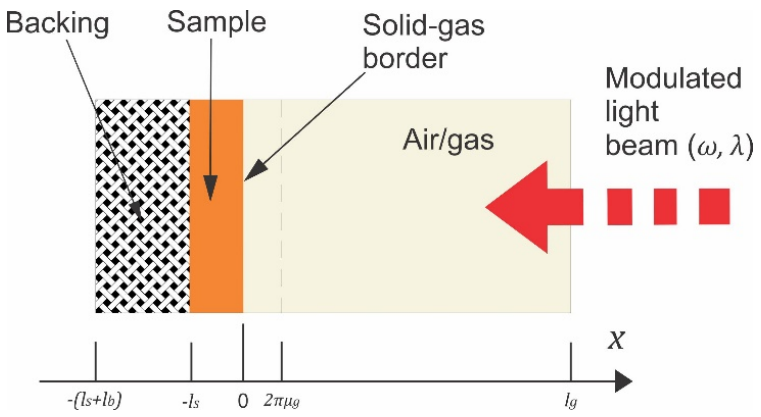

Figure 2.2 View of the cross section of the cylindrical photoacoustic cell, showing the position of the sample, and backing material.

The density of heat produced at any point *x* due to the light absorbed is given by,

$$\frac{1}{2}\beta\eta I_0 e^{\beta x}(1+\cos\omega t) \tag{2.1}$$

where β is the optical absorption coefficient of the solid sample (in cm^{-1}) for a given wavelength and η is the efficiency at which the absorbed light is converted into heat. *x* takes negative values as it extends through the solid from $x=0$ to $x=-l_s$; with light impacting on $x=0$. The equation of thermal diffusion due to the conduction mechanism in the solid can be written as,

$$\frac{\partial^2 T_s}{\partial x^2} = \frac{1}{\alpha_s}\frac{\partial T_s}{\partial t} - A\eta e^{\beta x}\left[1+e^{j\omega t}\right]; \qquad -l_s \le x \le 0 \tag{2.2}$$

where $= \beta I_0 \eta / 2k_s$. For backing and gas, the heat diffusion equations are given by:

$$\frac{\partial^2 T_b}{\partial x^2} = \frac{1}{\alpha_b}\frac{\partial T_b}{\partial t}; \qquad -l_s - l_b \le x \le -l_s \tag{2.3}$$

and

$$\frac{\partial^2 T_g}{\partial x^2} = \frac{1}{\alpha_g}\frac{\partial T_g}{\partial t}; \qquad 0 \le x \le l_g \tag{2.4}$$

Equations 2.2, 2.3 and 2.4 must be solved with the corresponding temperature and flow continuity boundary conditions,

$$T_g(0,t) = T_s(0,t) \tag{2.5}$$

$$T_b(-l,t) = T_s(-l,t) \tag{2.6}$$

$$k_g \frac{dT_g}{dx}(0,t) = k_s \frac{dT_s}{dx}(0,t) \tag{2.7}$$

$$k_g \frac{dT_b}{dx}(-l,t) = k_s \frac{dT_s}{dx}(-l,t) \tag{2.8}$$

Considering the isobaric expansion of the thin gas layer of thickness $2\pi\mu_g$ followed by an adiabatic compression of the remaining gas caused by volume variation in the cell, an analytical expression is obtained for the pressure variation inside the cell at room temperature as a function of position and time. *Q* is defined as the explicit solution obtained in x=0, thus,

$$Q = \frac{\eta\beta I_0 \gamma P_0}{2\sqrt{2}k_s l_g a_g T_0(\beta^2-\sigma_s^2)}\left(\frac{(\sigma-1)(b+1)e^{\sigma_s l_s}-(\sigma+1)(b-1)e^{-\sigma_s l_s}+2(b-\sigma)e^{-\beta l_s}}{(g+1)(b+1)e^{\sigma_s l_s}-(g-1)(b-1)e^{-\sigma_s l_s}}\right)e^{j(\omega t-\pi/4)} \tag{2.9}$$

where $b = k_b a_b/k_s a_s$; $g = k_g a_g/k_s a_s$; $\sigma = (1-j)\beta/2a_s$; $\sigma_s = (1+j)a_s$; $a_s = (\pi f/\alpha_s)^{1/2}$; k_i, a_i y α_i are the thermal conductivity, the thermal diffusion coefficient and the thermal diffusivity of the medium *i*.

With this model it is possible to do a kind of optical absorption spectroscopy if the PA signal is measured as a function of the wavelength of the incident beam. The advantages of PA spectroscopy respecting conventional optical spectroscopies are the possibility of analyzing both optically very opaque and transparent samples, its insensitivity to scattered light and the option it offers of making depth profiling using the dependence of the thermal diffusion length on light modulation frequency. Alternatively, if the wavelength of the incident beam is kept constant and the modulation frequency is varied, it is possible to obtain information concerning to the thermal properties of the sample [14].

Thermally thick and optically opaque/transparent sample. Equation 2.9 is a complicated expression to interpret due to the large number of variables involved. In order to make a simple analysis of this, the physics of the problem allows some approximations to be made by comparing the relative values of the three characteristic lengths involved, namely the thermal diffusion and the optical absorption lengths and the thickness of the sample. These have already been considered by RG. One case of

particular interest is that in which the sample is thermally thick and optically opaque/transparent, that's it, $\mu_s \ll l_s; \mu_s < \mu_\beta$ and $\mu_\beta \ll l_s / \mu_\beta > 1$, where $\mu_\beta = 1/\beta$ is the optical absorption length. Under these conditions the complex photoacoustic signal can be rewritten as:

$$Q = -\frac{I_0 \gamma P_0}{2\sqrt{2} l_g T_0} \frac{j\beta\mu_s\mu_g}{2} \left(\frac{\mu_s}{k_s}\right) \tag{2.10}$$

Here, the signal is proportional to the optical absorption coefficient of the sample, β, and therefore to its absorbance. It is also proportional to the product $\beta\mu_s$. The first proportionality means that spectroscopy is possible and the second one that only a layer of thickness μ_s contributes to the signal [15,16,17].

It is worth to be mentioned that other mechanisms [18,19] can also influence the photoacoustic signal and that other photoacoustic cell configurations can be also used. For example, if the sample substitutes the quartz window in Figure 2.1, we will have the so-called open PA cell configuration [20]. In this configuration, there is a competition between the mechanisms of heat diffusion and thermoelastic sample bending that can be used to measure, simultaneously, both the thermal diffusivity and the linear thermal expansion coefficient of the sample [21].

2.2 Photopyroelectric Technique

This photothermal technique is primarily named after the type of sensor (pyroelectric) used to detect thermal waves. The pyroelectric effect consists in the spontaneous change of polarization, $P_s(t)$, on the surface perpendicular to the polar axis of a crystal, which is proportional to the temperature variation, dT, as described by [22]:

$$dP_s(t) = -pdT(t) \tag{2.11}$$

where p is the pyroelectric coefficient of the material. In addition, from Equation 2.11, it follows that the detector can generate a current $I(t)$ given by

$$I(t) = A_p p \frac{dT(t)}{dt} \tag{2.12}$$

where A_p is the detector area. Equation 2.12 is the simplest way to represent the pyroelectricity phenomenon in terms of electric current, but it is important to note that an equivalent electric circuit allows this phenomenon to be represented in terms of a voltage generator.

This type of detectors turn out to be very efficient and sensitive to small temperature variations, so that Coufal [23] and Mandelis [24] made use of them to obtain optical absorption spectra of several samples to which a pyroelectric sensor was attached. Later, Mandelis and Zver [25] proposed the theory of photopyroelectric spectroscopy in solids, which was later approached and generalized by Chirtoc and Mihailescu (C-M) [26, who proposed a general analytical expression for the complex photopyroelectric signal in the one-dimensional case. To obtain this expression, a multilayer arrangement like that proposed by RG was considered, as shown in Figure 2.3.

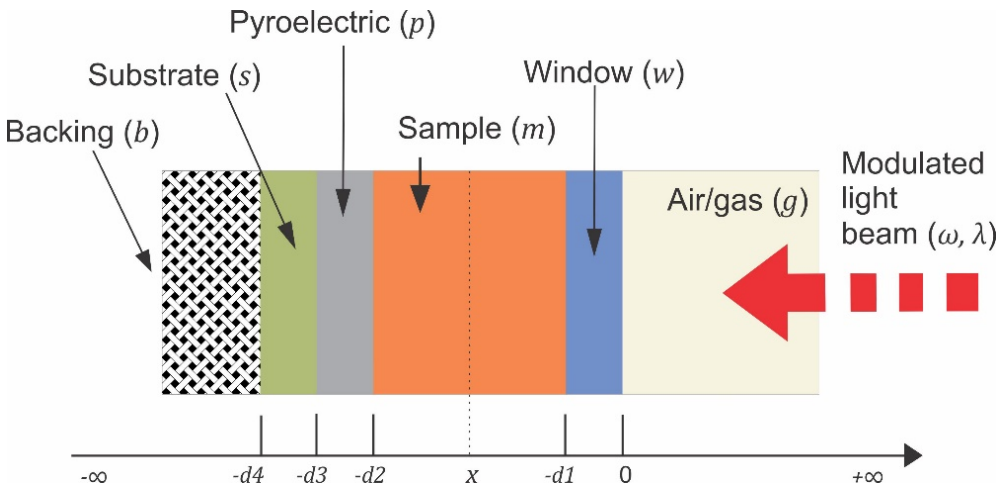

Figure 2.3 Schematic view of the cross section of the photopyroelectric cell, showing the position of the window, sample, pyroelectric sensor, substrate and backing material, in the so-called Back Detection Configuration. Metallic electrodes (not shown in the figure) are deposited on both sides of the pyroelectric sensor to measure the signal.

In this scheme, the cell is uniformly irradiated by a monochromatic light beam with wavelength λ and irradiance H_o [W/m^2], which is periodically modulated in intensity at the angular frequency ω. A thermally thin and optically opaque electrode is assumed.

The thermal wave generated in the sample by the absorption of light propagates from the sample to adjacent layers producing a periodic temperature field in the pyroelectric given by $T_p(x,t) = T_p(x)e^{i\omega t}$, which is converted into an electrical signal by the pyroelectric effect. Considering a R_eC circuit [22] (R_e is the electrical resistance and C is the electrical capacity) equivalent to the sensor that is connected in parallel with the current source (Equation 2.12), the voltage output of the pyroelectric will be:

$$V(t) = \frac{i\omega\tau_E p L_p}{\in(1+i\omega\tau_E)}\langle T_p(x)\rangle e^{i\omega t} \tag{2.13}$$

where $\tau_E = R_eC$ is the electrical time constant and $\in$ is the dielectric constant of the pyroelectric sensor. In order to find an expression for the temperature in the steady state, the following system of heat diffusion equations must be solved

$$\frac{\partial^2 T_j(x)}{\partial x^2} - \frac{i\omega}{\alpha_j}T_j(x) = 0, \quad j = g,w,p,s,b \tag{2.14a}$$

$$\frac{\partial^2 T_m(x)}{\partial x^2} - \frac{i\omega}{\alpha_m}T_m(x) = \frac{H_o\beta\eta_m}{2k_m}e^{[\beta(x+d1)]} + \frac{RH_o\beta\eta_m}{2k_m}e^{-\beta L_m}e^{[-\beta(x+d2)]} \tag{2.14b}$$

where β is the optical absorption coefficient, R is the optical reflection coefficient at the sample´s front surface and η_m is the light energy into heat conversion quantum efficiency of the sample. In Equation 2.14b, the terms on the right-hand side represent two heat sources in the sample due to the incident and reflected light waves. The boundary conditions for temperature continuity at all interfaces are,

$$T_i(i,j) = T_j(i,j), \quad (i,j) = (g,w),(w,m),(m,p),(p,s),(s,b) \tag{2.15}$$

and for the heat flux continuity,

$$k_i\frac{\partial}{\partial x}T_i(i,j) - k_j\frac{\partial}{\partial x}T_j(i,j) = 0, \quad (i,j) = (g,w),(w,m),(p,s),(s,b) \tag{2.16a}$$

$$k_p\frac{\partial}{\partial x}T_p(p,m) - k_m\frac{\partial}{\partial x}T_m(p,m) = (1-R)\left(\frac{H_0}{2}\right)\eta_r e^{(-\beta l_m)} \tag{2.16b}$$

In the above equations the term (i, j) represents the interface between regions i and j, and η_r is the light into heat conversion quantum efficiency of the sensor, which arises for the fraction of the light energy that can eventually reach it. Using Equations 2.14,

2.15 and 2.16 the following expression for the complex photopyroelectric voltage response of the multilayer system shown in Figure 2.3 is obtained:

$$V(t) = \frac{G\alpha_p \tau_E}{k_p(1+i\omega\tau_E)}\Gamma e^{i\omega t} \tag{2.17}$$

where Γ is a dimensionless factor given by [26]:

$$\begin{aligned}\Gamma = e^{-\beta l_m}\{&2\eta_m(1-r^{-2})^{-1}\left[W_+^r e^{\beta l_m} + RW_-^r e^{-\beta l_m}\right] \\ &- \left[(1-r^{-1})^{-1}\eta_m - R(1+r^{-1})^{-1}\eta_m - (1-R)\eta_r\right]W_+ M \\ &+ \left[(1+r^{-1})^{-1}\eta_m - R(1-r^{-1})^{-1}\eta_m - (1-R)\eta_r\right]W_- M^{-1}\}[S_+(P-1) \\ &+ S_-(P^{-1}-1)] \\ &\times\{\left[(b_{mp}+1)S_+P - (b_{mp}-1)S_-P^{-1}\right]W_+ M \\ &+ \left[(b_{mp}-1)S_+P - (b_{mp}+1)S_-P^{-1}\right]W_- M^{-1}\}^{-1}\end{aligned} \tag{2.18}$$

with

$$W_\pm \equiv e^{\sigma_w l_w}(b_{gw}+1)(b_{wm}\pm 1) + e^{-\sigma_w l_w}(b_{gw}-1)(b_{wm}\mp 1),$$

$$W_\pm^r \equiv e^{\sigma_w l_w}(b_{gw}+1)(b_{wm}r^{-1}\pm 1) + e^{-\sigma_w l_w}(b_{gw}-1)(b_{wm}r^{-1}\mp 1),$$

$$S_\pm \equiv e^{\sigma_s l_s}(b_{bs}+1)(b_{sp}\pm 1) + e^{-\sigma_s l_s}(b_{bs}-1)(b_{sp}\mp 1),$$

$$M \equiv e^{\sigma_m l_m},\ \ P \equiv e^{\sigma_p l_p},\ \ b_{ij} = \frac{k_i\sigma_i}{k_j\sigma_j},\ \ r \equiv \frac{\beta}{\sigma_m},\ \ G \equiv \frac{pH_0}{2\in}$$

Due to the large number of parameters present in Equation 2.18, it is difficult to obtain quantitative information about optical or thermal parameters in a simple way. In order to reduce it, C-M follow the procedure adopted by RG in which different approximations of the complex equation are made relating the thickness, optical absorption length and thermal diffusion length in each layer, as well as the relation of the thermal effusivities b_{ij} between the layers that are in contact. In this way, it was possible to demonstrate that in this experimental configuration it is possible to obtain information about β, α and e of the sample from an analysis of amplitude and phase of the pyroelectric signal [26]. This configuration is colloquially known as Back-detection (BPPE), since the temperature rise is detected by a pyroelectric sensor that is in thermal contact with the rear surface of the sample (Figure 2.3). In the particular

case where the window and substrate are thermally thick and the absorption occurs within a very thin opaque layer at the *w/m* interface (opaque sample), the expression 2.18 is reduced to [27]:

$$V(f) = \frac{2G\alpha_p\tau_E}{k_p(1+i\omega\tau_E)} * \frac{e^{-\sigma_m L_m}}{(b_{wm}+1)(b_{mp}+1)} \frac{e^{\sigma_p L_p} + R_{sp}e^{-\sigma_p L_p} - (1+R_{sp})}{e^{\sigma_p L_p} - R_{sp}R_{mp}e^{-\sigma_p L_p} + (R_{mp}e^{\sigma_p L_p} - R_{sp}e^{-\sigma_p L_p})R_{wm}e^{-2\sigma_m L_m}} \quad (2.19)$$

where $R_{ij} = (b_{ij} - 1)/(b_{ij} + 1)$; *(i, j=s ,p, m, w, g).* This equation depends only on the thermal parameters α and *e*. It is worth mentioning that the parameter R_{ij} can be strongly affected by factors such as slight misalignments and thermal mismatches between sample and sensor.

Frontal-detection (FPPE) **(**also Known as Inverse Photopyroelectric Detection) [28]. In this method the most relevant thing is that light beam falls directly on the front face of the pyroelectric sensor through the window and the samples is attached to its rear side. As shown in Figure 2.3, the sensor is in intimate contact with the substrate at the rear. The substrate in this case will be replaced by the sample, as shown in Figure 2.4.

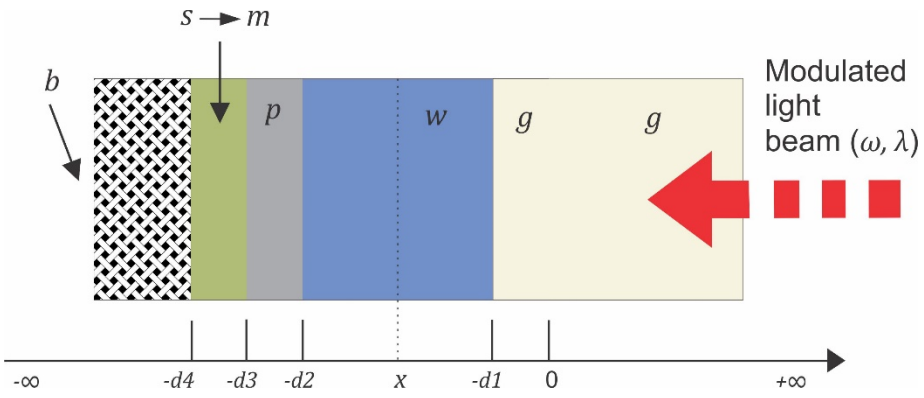

Figure 2.4 View of the cross section of the photopyroelectric cell in FPPE, showing the position of the window, pyroelectric sensor, substrate/sample and backing material.

This configuration is important because it allows studies on opaque materials, which was complicated to do in BPPE that is limited to the study of liquids, gases or semitransparent solids, ideal for the scheme considered in Figure 2.3. Maintaining the

conditions of thermally thick for the window and the substrate, the expression obtained for the voltage variation of the pyroelectric in FPPE is [29],

$$V(f) = \frac{2G\alpha_p\tau_E}{k_p(1+i\omega\tau_E)} * \frac{1}{(b_{wp}+1)} \frac{1-e^{-\sigma_p L_p}+R_{sp}(e^{-2\sigma_p L_p}-e^{-\sigma_p L_p})}{1-R_{sp}R_{wp}e^{-2\sigma_p L_p}} \quad (2.20)$$

In order to eliminate the parameters related to instrumentation and thermo-optical properties of the detection element, a normalization process is necessary. The best reference signal is obtained using air instead of the sample. Assuming then that $R_{sp} = R_{gp} = -1$, one gets for the normalized signal:

$$V_n(f) = 1 - (1 + R_{sp})e^{-\sigma_p L_p} \quad (2.21)$$

if the whose amplitude and phase signal are given by,

$$|V_n(f)| = \left\{\left[(1 + R_{sp})\sin(a_p L_p)e^{-a_p L_p}\right]^2 + \left[1 - (1 + R_{sp})\cos(a_p L_p)e^{-a_p L_p}\right]^2\right\}^{1/2} \quad (2.22)$$

and

$$\emptyset_{V_n} = arctan\left(\frac{(1+R_{sp})\sin(a_p l_p)e^{-a_p l_p}}{1-(1+R_{sp})\cos(a_p l_p)e^{-a_p l_p}}\right) \quad (2.23)$$

respectively. In a typical experiment, the amplitude and phase are measured as a function of the modulation frequency and the thermal effusivity, which is contained in the R_{sp} term, is obtained through a fitting procedure in which R_{sp} can be left as fit parameter in Equation 2.22 and 2.23. The e_s will be then calculated by:

$$e_s = e_p \frac{1+R_{sp}}{1-R_{sp}} \quad (2.24)$$

2.3 Active Infrared Thermography

Infrared thermography (IRT) consists of detecting the infrared radiation coming from a medium or body using a suitable camera, and representing it as image known as Thermogram. Although the phenomenon of infrared radiation was discovered in 1800 by Herschel, years had to pass to do research and technological developments with this type of radiation, highlighting the development of the first mono-detector IR camera in

1963 by AGA. Subsequently, since the last decade of the twentieth century there is growing interest in the field of IRT, motivated by the emergence of Focal Plane Array Cameras, which have high thermal sensitivity, and high spatial and temporal resolution [30].

The methods and techniques based on IRT can be divided into two groups: passive and active infrared thermography. In the first, a controlled external excitation source is not used to generate an additional heat flow within the body under observation, i.e. only natural heat sources are considered. In the second one, the sample under examination is heated by an external stimulus, a fact that allows studying the thermal response of the body to such stimulation. There are different variants of active IRT depending on the source of heat, which have been used in different fields of applied science to obtain qualitative and quantitative information. Active IRT is used in this manuscript for the thermal characterization of moving and static samples, as well as static interfaces.

2.3.1 Lock-in Thermography

This technique is a combination of the Phase-Sensitive Detection signal processing method mentioned in section 1.7 and Active IRT. It consists of generating a thermal wave in a material with a light beam modulated in intensity and recording the temperature field produced on its surface with the help of an infrared camera with lock-in incorporated capabilities synchronized with the light modulation frequency. A lock-in processing on each pixel of the obtained thermogram sequence is carried out giving as a final result an amplitude and phase thermogram. Lock-in thermography was first described by Carlomagno and Berardi in 1976 [31], but it was not until the 1990s when it was widely exploited with the development of the first Lock-in IR camera by Busse [32]. These cameras generally use a lock-in correlation process [11].

The signal of the lock-in correlation process can be expressed as:

$$S_{lc} = \frac{1}{t_{int}} \int_0^{t_{int}} F(t)W(t)dt \tag{2.25}$$

Where t_{int} is a finite integration time, $F(t)$ is the detected signal and $W(t)$ is the correlation function. In the discrete case (digital signal), the procedure consists of

averaging the product of the values of *F* and *W* over *n* events during a lock-in period, so that:

$$S_n = \frac{1}{n}\sum_{k=1}^{n} F_k W_k \tag{2.26}$$

The *W* correlation function is generally harmonic. That is, if the function is symmetrical and evaluated over a full period, the sum of all values is zero, suppressing the DC contribution in the S_n signal. Considering now *N* periods in a synchronous process and keeping the weights equal in each lock-in period, the lock-in correlation signal will be:

$$S_{nN} = \frac{1}{nN}\sum_{j=1}^{N}\sum_{k=1}^{n} F_{j,k} W_k \tag{2.27}$$

In camera-based systems, the camera is running at a certain frame rate, f_{fr}, converting the surface temperature distribution (in two dimensions) into an image containing the temperature information. It is important to mention that in lock-in thermography, as a rule two channels are used (in phase and quadrature) that deliver two corresponding signals from which amplitude and phase thermograms can be obtained. Figure 2.5 is a schematic of the discrete lock-in correlation process [11].

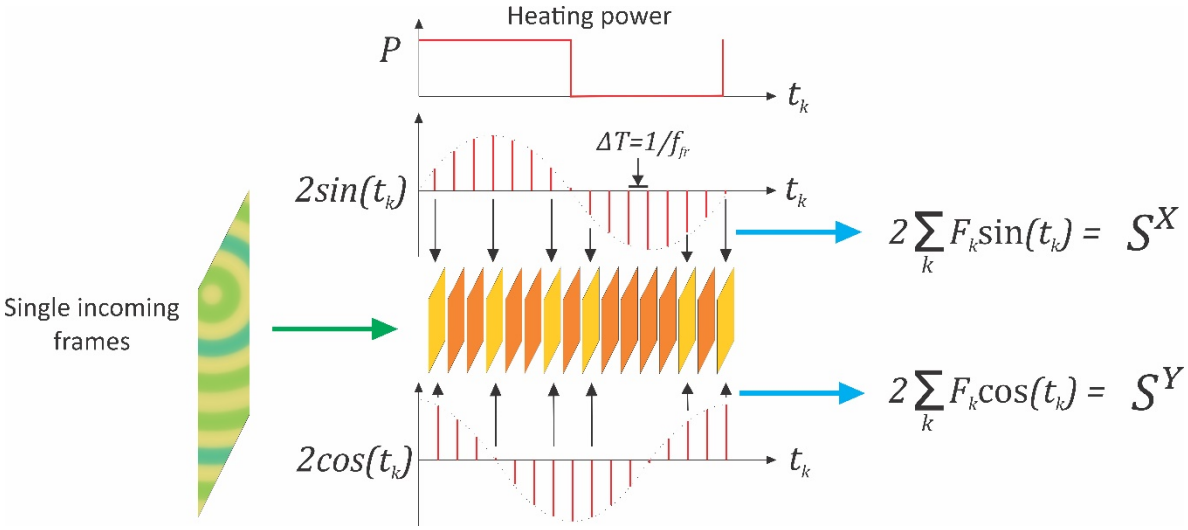

Figure 2.5 Principle of the lock-in correlation process in camera-based systems [33].

In the Figure, *P* is the maximum power of the periodic excitation source, and S^X and S^Y represent the in-phase and quadrature signals respectively from which the amplitude and phase are obtained according to Equations 1.28 and 1.29.

2.3.1.1 Thermal diffusivity by the slopes method

Using LIT it is possible to determine the thermal diffusivity parameter of slabs using the Surface Thermal Wave technique as demonstrated by Zhang and Imhof in 1996 [34]. Taking their analysis as a reference, different proposals have been made to measure this parameter using thermographic cameras, such as the one presented by Mendioroz et al [35]. These authors make a mathematical development and present linear relationships between the amplitude and phase of the signal and the distance from a localized heat source that allow to determine α_s of thin plates, considering also the heat losses on their surfaces. Consider a semi-infinite, homogeneous and isotropic slab that is illuminated with a focused beam of P_o (W) power with a Gaussian distribution of radius a (at. $1/e^2$) (Figure 2.6) that produces a heat flux on the surface of the sample at z=0 given by

$$q(r) = \frac{P_o}{\pi a^2} e^{-2r^2/a^2} \tag{2.28}$$

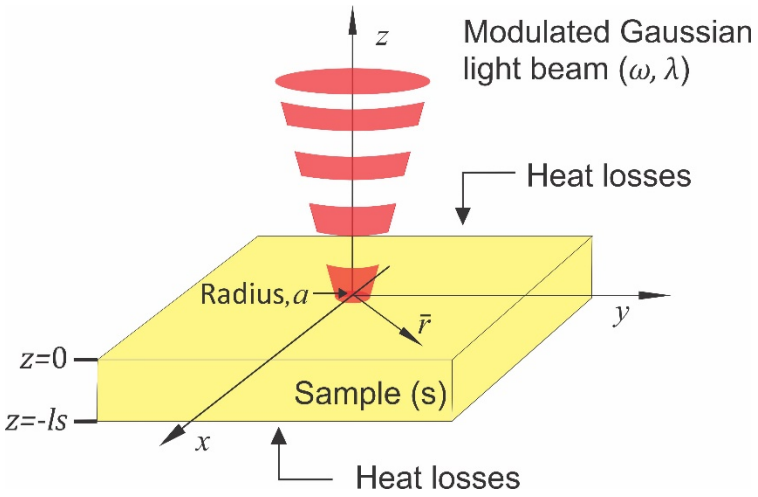

Figure 2.6 Schematic of a semi-infinite sample illuminated by a focused and modulated light beam.

The equation of heat diffusion in the sample, in the stationary state, in cylindrical coordinates r and z (without an angle dependence), is given by

$$\frac{\partial^2 T_{ac}}{\partial r^2} + \frac{1}{r}\frac{\partial T_{ac}}{\partial r} + \frac{\partial^2 T_{ac}}{\partial z^2} - \sigma^2 T_{ac} = 0; \tag{2.29}$$

where $\sigma = \sqrt{i\omega/\alpha_s}$. It is subjected to the following flow continuity conditions on both slab surfaces,

$$k_s \frac{\partial T_{ac}}{\partial z}\Big|_{z=0} + h_o T_{ac}|_{z=0} = \frac{P_o}{\pi a^2} e^{-2r^2/a^2} \tag{2.30}$$

$$k_s \frac{\partial T_{ac}}{\partial z}\Big|_{z=-l_s} - h_1 T_{ac}|_{z=-l_s} = 0 \tag{2.31}$$

where h_0 and h_1 are the heat losses transfer coefficients on the upper and lower surface of the sample, respectively, and k_s is the thermal conductivity of the sample. Considering the geometry of the problem the mentioned authors work in Hankel's space to obtain the solution of the problem. In this space, Equations 2.28 to 2.31 can be rewritten respectively as:

$$\overline{q(\delta)} = \frac{P_o}{4\pi} e^{-(\delta a)^2/8} \tag{2.32}$$

$$\frac{\partial^2 \overline{T_{ac}(\delta,z)}}{\partial z^2} - \beta_h^2 \overline{T_{ac}(\delta,z)} = 0 \tag{2.33}$$

$$k_s \frac{\partial \overline{T_{ac}}}{\partial z}\Big|_{z=0} + h_o \overline{T_{ac}}|_{z=0} = \frac{P_o}{4\pi} e^{-(\delta a)^2/8} \tag{2.34}$$

$$k_s \frac{\partial \overline{T_{ac}}}{\partial z}\Big|_{z=-l_s} - h_1 \overline{T_{ac}}|_{z=-l_s} = 0 \tag{2.35}$$

where $\beta_h^2 = \delta^2 + \sigma^2$ and δ is the Hankel's variable. The solution to Equation 2.33 is given by:

$$\overline{T_{ac}(\delta,z)} = A(\delta)e^{\beta_h z} + B(\delta)e^{-\beta_h z} \tag{2.36}$$

where the variables A and B are obtained from the boundary conditions. The temperature distribution in the sample is obtained using Hankel's inverse-transform as:

$$T_{ac(r,z)} = \int_0^\infty \delta J_o(\delta r)\overline{T_{ac}(\delta,z)}d\delta \tag{2.37}$$

where J_0 is the Bessel function of zero order. After some algebraic procedures, this equation can be rewritten as [35]:

$$T_{ac}(r,z) = \frac{P_o}{4\pi k_s}\int_0^\infty \delta J_o(\delta r)\frac{e^{-(\delta a)^2/8}}{\beta_h} \times \left[\frac{(1+H_1)e^{\beta_h l_s}e^{\beta_h z}+(1-H_1)e^{-\beta_h l_s}e^{-\beta_h z}}{(1+H_0)(1+H_1)e^{\beta_h l_s}-(1-H_0)(1-H_1)e^{-\beta_h l_s}}\right] d\delta \quad (2.38)$$

in which $H_0 = h_0/k_s\beta_h$and $H_1 = h_1/k_s\beta_h$. In the above equations the heat conduction to the gas was neglected due to its low thermal conductivity, i.e. only heat losses by convection and radiations have been considered.

As well as in the approximate cases presented in the Photoacoustics and Photopyroelectric technique (Section 2.1 and 2.2), the following particular situations are of interest here for the measurement of the thermal diffusivity:

Thermally thin slab. i.e $l_s \ll \mu_s$, therefore, $e^{\pm\sigma l_s} = 1 \pm \sigma l_s$ or $e^{\pm\beta_h l_s} \approx 1 \pm \beta_h l_s$ and $h_0 = h_1 = h$. The Equation 2.38 reduces to:

$$T_{ac}(r) = \frac{P_o}{4\pi k_s l_s}\int_0^\infty \delta J_o(\delta r)\frac{e^{-(\delta a)^2/8}}{\beta'^2_h}\, d\delta \quad (2.39)$$

with $\beta'^2_h = \delta^2 + \sigma'^2$ and σ'^2=$\sigma^2 + (2h/k_s l_s)$. Note that the temperature oscillation does not depend on *z*. Now considering a very focused excitation beam (*a*=0) and using an asymptotic approximation for large *r* values ($r \to \infty$), the Equation 2.39 is rewritten as,

$$T_{ac-thin}(r \to \infty, a = 0) = \frac{P_o}{4\pi k_s l_s}\sqrt{\frac{\pi}{2}}\frac{1}{\sqrt{\sigma'_R + i\sigma'_I}}\frac{e^{-\sigma'_R r}}{\sqrt{r}}e^{-i\sigma'_I r} \quad (2.40)$$

where σ'_R and σ'_I are the real and imaginary part of σ. As can be seen, the phase has a linear behaviour as a function of *r* whose slope is

$$m_\varphi = -\sigma'_I \quad (2.41)$$

In addition, taking the natural logarithm of the amplitude of the temperature multiplied by the $\sqrt{r}$, a similar linear behavior is obtained as in the phase but whose slope is

$$m_{\ln(\sqrt{r}T_{ac-thin}(r\to\infty,a=0))} = -\sigma'_R \quad (2.42)$$

It is important to mention that when one gets α_s with one of the Equations, 2.41 or 2.42, alone, the value obtained tends to be underestimated or overestimated,

respectively. However, the product of both slopes is independent of heat losses and allows an optimal value of α_s to be calculated from the product

$$m_{\varphi} \times m_{\ln(\sqrt{r}T_{ac-thin}(r\to\infty,a=0))} = \pi f/\alpha_s \tag{2.43}$$

Thermally thick slab. *i.e* $l_s \gg \mu_s$, therefore, $e^{-\sigma l_s} \approx 0$ or $e^{-\beta_h l_s} \approx 0$. Equation 2.38 reduces to:

$$T_{ac-thick}(r, z=0) = \frac{P_o}{4\pi k_s}\int_0^{\infty} \delta J_o(\delta r)\frac{e^{-(\delta a)^2/8}}{\beta_h+\frac{h_0}{k_s}}\, d\delta \tag{2.44}$$

The Equation 2.44 has no analytical solution even by doing *a*=0. Through numerical simulations considering the absence of heat losses one comes to the conclusion that the phase has a linear behavior as a function of *r*, whose slope is:

$$m_{\varphi} = -\sqrt{\pi f/\alpha_s} \tag{2.45}$$

Likewise, the natural logarithm of the amplitude of the temperature multiplied by *r* as a function of *r* is linear with a slope:

$$m_{\ln(r*T_{ac-thick}(r,z=0))} = -\sqrt{\pi f/\alpha_s} \tag{2.46}$$

It is important to mention that the effect of heat losses in thick samples is small even for samples with low thermal conductivity. Only at very low frequencies, less than 0.1 Hz, these losses should be considered [35,36].

2.3.1.2. Infinite vertical interface

In this section we present a method to measure the contact thermal resistance produced by an infinite interface vertical, using LIT with laser spot heating. The main basis of this method is to produce a heat flux across the interface that in turn causes an asymmetry in the temperature field at the surface of the material induced by the effect of the interface (also called Crack), that acts as a thermal resistance. The contact thermal resistance assigned to the vertical interface causes a partial blockage of the heat flow when the laser Spot is focused near the crack. This method has been of interest to different authors since the 1990s, who have introduced multiple variations of it with specific applications for the characterization of geometric parameters of a crack using

continuous, pulsed and modulated excitation. In the case of Gaussian point excitation using LIT, Pech-May *et al* obtained a semi-analytical solution for infinite vertical interfaces using the Hankel transform [37]. They propose a semi-infinite and opaque material with an infinite vertical interface placed in plane *y*=0. The surface of the sample is illuminated by an ideal laser spot modulated in frequency, $P(t) = \frac{1}{2}P_0[1 + \cos(\omega t)]$. The center of the spot laser is located at a distance *d* from the interface (0, *d*, 0), as shown in Figure 2.7. Adiabatic conditions are assumed on the sample surface, so heat losses to the surrounding air are neglected.

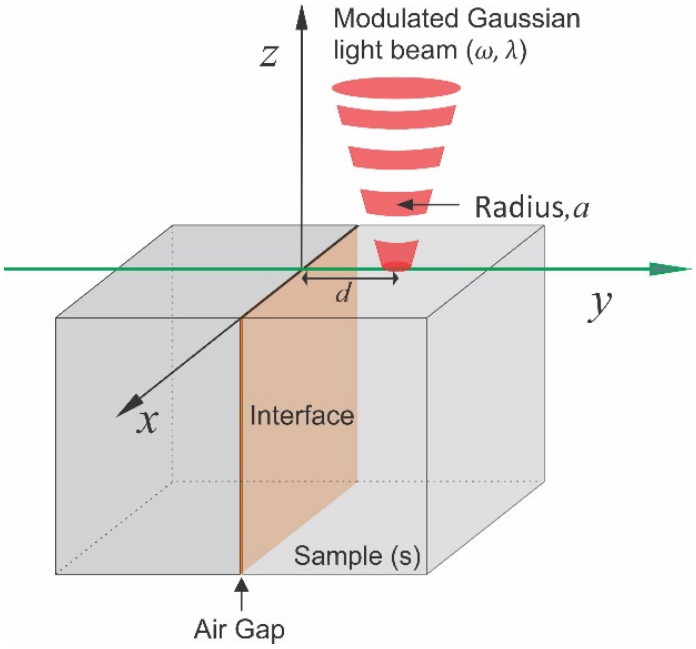

Figure 2.7 Schematic of an infinite vertical interface inside a material being illuminated with a focused and modulated laser beam.

First, authors consider that the medium is infinite, i.e. there is no surface and that the excitation is point-like. Expressions for the spherical thermal wave $T(x, y, z)$ generated by the excitation and the waves scattered by the interface, $T(x, y, z)_+$ and $T(x, y, z)_-$, are given by:

$$T(x, y, z) = \frac{P_o}{4\pi k_s}\frac{e^{-\sigma R_c}}{R_c} = \frac{P_o}{4\pi k_s}\int_0^\infty \delta J_o(\delta r)\frac{e^{-\beta_h|y-d|}}{\beta_h}\, d\delta \qquad (2.47)$$

$$T(x, y, z)_+ = P_o\int_0^\infty \delta J_o(\delta r)Ae^{-\beta_h y}\, d\delta; \qquad y > 0 \qquad (2.48)$$

$$T(x,y,z)_- = P_o \int_0^\infty \delta J_o(\delta r) B e^{\beta_h y}\ d\delta; \qquad y<0 \qquad (2.49)$$

where $R_c = \sqrt{x^2+(y-d)^2+z^2}$ and $r = \sqrt{x^2+z^2}$. Expression 2.47 represents a spherical wave in Hankel's space. The material temperature for $y>0$ and $y<0$, is given by $T_+(x,y,z) = T(x,y,z) + T(x,y,z)_+$ and $T_-(x,y,z) = T(x,y,z) + T(x,y,z)_-$, respectively. To determine the constants *A* and *B* in Equations 2.48 and 2.49, the conditions of continuity of heat flow and discontinuity of the temperature at the interface will be:

$$-k_s \frac{\partial T_+}{\partial y}\Big|_{y=0} = -k_s \frac{\partial T_-}{\partial y}\Big|_{y=0} \qquad (2.50)$$

$$(T_+ - T_-)_{y=0} = R_{th} k_s \frac{\partial T_+}{\partial y}\Big|_{y=0} \qquad (2.51)$$

where R_{th} is the thermal contact resistance of the interface or crack that is related to the thickness of the air gap according to Equation 1.13. Now, the presence of the surface of the sample is taken into account by applying the image method (assuming adiabatic conditions at the surface) that means having a laser spot of double power. Finally, a real circular Gaussian spot of a maximum power P_o and radius *a* is considered, for which the temperature inside the sample becomes the sum of the contribution of each point of the Gaussian spot weighted by its intensity.

$$T_\pm(x,y,z) = \frac{P_o}{\pi^2 a^2 k_s} \int_{-\infty}^{\infty}\int_{-\infty}^{\infty} dx_0 dy_0\ e^{-\frac{2\left[x_0^2+(y_0-d)^2\right]}{a^2}} \times \left[\frac{e^{-\sigma R_d}}{R_d} \pm k_s R_{th} \frac{y_0}{|y_0|} \int_0^\infty \delta J_o(\delta r_d) \frac{e^{-\beta_h(|y_0|+|y|)}}{2+k_s R_{th}\beta_h}\ d\delta\right] \qquad (2.52)$$

where $R_d = \sqrt{(x-x_0)^2+(y-y_0)^2+z^2}$ and $r_d = \sqrt{(x-x_0)^2+z^2}$. Equation 2.52 needs to be analyzed with numerical methods. In order to reduce the computational cost, a temperature profile along the *y*-axis is considered, *i.e.* perpendicular to the interface and through the center of the laser spot [11,37]:

$$T_\pm(0,y,0) = \frac{P_o}{\pi^2 a^2 k_s} \int_{-\infty}^{\infty}\int_{-\infty}^{\infty} dx_0 dy_0\ e^{-\frac{2\left[x_0^2+(y_0-d)^2\right]}{a^2}} \frac{e^{-\sigma R_1}}{R_1}$$

$$\pm\frac{P_o}{4\pi k_s}k_s R_{th}\int_0^{\infty} e^{-\frac{(\delta a)^2}{16}} I_0\left[\frac{(\delta a)^2}{16}\right]\frac{e^{-\frac{a^2{\beta_h}^2}{8}-\beta_h d-\beta_h|y|}}{2+k_s R_{th}\beta_h}$$

$$\times\left[1-Erfc\left(\frac{a^2{\beta_h}^2-4d}{2\sqrt{2}a}\right)-e^{2\beta_h d}Erfc\left(\frac{a^2{\beta_h}^2+4d}{2\sqrt{2}a}\right)\right]\delta d\delta \qquad (2.53)$$

Here $R_1=\sqrt{{x_0}^2+(y-y_0)^2}$, I_0 is the modified Bessel function of zero order and *Erfc* is the complementary error function. A numerical simulation allows to extract information about the amplitude and phase of Equation 2.53, from which the R_{th} value of the interface is mainly obtained due to the abrupt discontinuity of the temperature in the plane y=0 as shown in Figure 2.8.

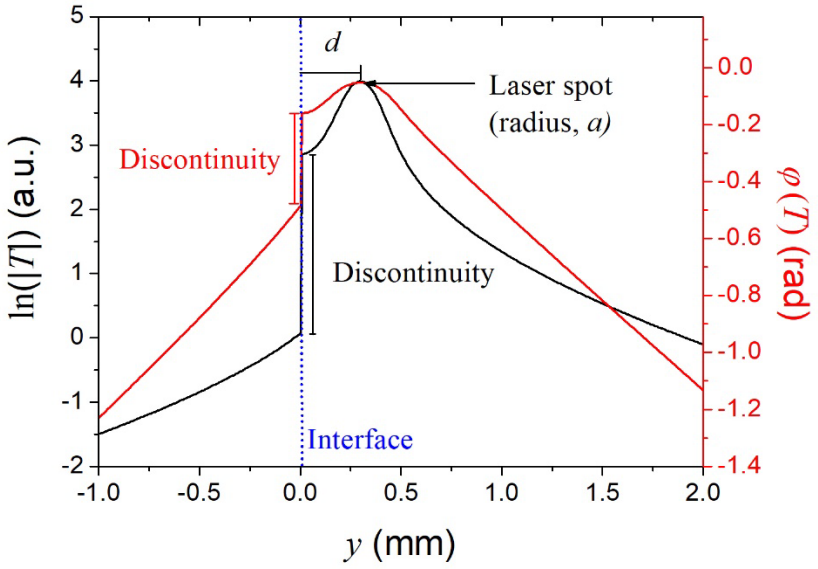

Figure 2.8 Numerical simulation curves of the natural logarithm of the temperature amplitude and phase showing the abrupt discontinuity of the temperature profile along the *y* axis. Simulation parameters were k_s = 15 W/mK, $\alpha_s = 4\times10^{-6}$ m^2/s, $R_{th} = 3.85\times10^{-5}$ m^{2}K/W, a = 150 µm, d = 300 µm and P_o = 300 mW.

2.3.2 Pulsed Infrared Thermography with Laser Spot

It is a method that allows to measure the in-plane thermal diffusivity of a material, on which a focused Gaussian pulse impinges generating a temperature gradient in the surface plane. In 2001, Cernushi *et al* demonstrated that by monitoring the time evolution of the spatial distribution of temperature on the rear surface of an isotropic

and semi-infinite slab, it is possible to obtain the thermal diffusivity of that plane. This is achieved by analyzing some spatial temperature profiles taken at different fixed times after the excitation pulse. These profiles, which must pass through the center of the laser spot, are fitted to a Gaussian function from which the time dependent standard deviation term is obtained. The square of this term depends linearly on time with a slope proportional to the in-plane thermal diffusivity [38,39,11].

Based on these works, Pech-May *et al* generalized the method considering (an)isotropic, semi-infinite and semitransparent/opaque slabs [40]. They started from a semi-transparent slab that is illuminated by a focused pulsed light beam and included effects of multiple reflections, heat losses by convection and radiation on the slab surfaces and transparency at infrared wavelengths.

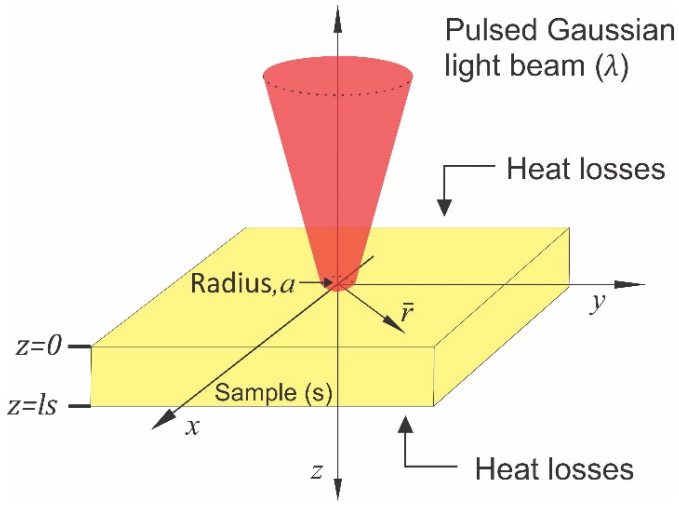

Figure 2.9 Schematic of a semi-infinite sample illuminated by a focused pulsed light beam.

They then considered a semitransparent anisotropic slab of thickness l_s, as shown in Figure 2.9, illuminated by a circular Gaussian source of radius a (defined as the distance at which the intensity is reduced by a factor of $1/e^2$) and intensity P_o. According to Beer-lambert's law and considering multiple reflections of the incident beam, the power distribution inside the sample will be:

$$P_0 = \frac{P_0(1-R)(e^{-\beta z}+Re^{-2\beta l_s}e^{\beta z})}{1-R^2e^{-2\beta l_s}} \tag{2.54}$$

On the other hand, the equation of heat diffusion in terms of Laplace in Cartesian coordinates for the slab on which P_o falls, is given by:

$$k_x \frac{\partial^2 \bar{T}}{\partial x^2} + k_y \frac{\partial^2 \bar{T}}{\partial y^2} + k_z \frac{\partial^2 \bar{T}}{\partial z^2} - s\rho c\bar{T} = -\frac{\overline{P_0} e^{-2(x^2+y^2)/a^2}(1-R)\beta(e^{-\beta z} - Re^{-2\beta l_s} e^{\beta z})}{2\pi a^2(1-R^2 e^{-2\beta l_s})} \quad (2.55)$$

where $\bar{T}$ is the Laplace transform of the sample temperature, *s* is the Laplace variable and $\overline{P_0}$ is the Laplace transform of the excitation beam. Considering a delta pulse function, $P_o(t) = P_o\delta(t)$, whose Laplace transform is $\overline{P_0}(s) = Q_0$, the general solution to Equation 2.54 can be written as:

$$\overline{T(x,y,z,s)} = \int_{-\infty}^{\infty}\int_{-\infty}^{\infty} d\lambda_f d\eta_f e^{-i(\lambda_f x + \eta_f y)} [Ae^{\beta_f z} + Be^{-\beta_f z} + Ce^{-\beta z} + Ee^{\beta z}] \quad (2.56)$$

where $\beta_f = \sqrt{\frac{\alpha_x {\lambda_f}^2 + \alpha_y {\eta_f}^2 + s}{\alpha_z}}$; being λ_f and η_f the Fourier variables and α the thermal diffusivity. The coefficients *C* and *E* are given by:

$$C = \frac{Q_0}{2\pi k_z} \frac{(1-R)\beta}{({\beta_f}^2 - \beta^2)} \frac{e^{-({\lambda_f}^2 + {\eta_f}^2)a^2/8}}{(1-R^2 e^{-2\beta l_s})}$$

$$E = -\frac{Q_0}{2\pi k_z} \frac{(1-R)\beta R e^{-2\beta l_s}}{({\beta_f}^2 - \beta^2)} \frac{e^{-({\lambda_f}^2 + {\eta_f}^2)a^2/8}}{(1-R^2 e^{-2\beta l_s})}$$

The constants *A* and *B* in Equation 2.56 are determined from the boundary conditions on the sample surfaces,

$$k_z \left.\frac{\partial \bar{T}}{\partial z}\right|_{z=0} - h\bar{T}|_{z=0} = 0 \quad (2.57)$$

$$k_z \left.\frac{\partial \bar{T}}{\partial z}\right|_{z=l_s} + h\bar{T}|_{z=l_s} = 0 \quad (2.58)$$

After applying the boundary conditions, the expression of the temperature inside the sample in terms of Laplace is given by:

$$\overline{T(x,y,z,s)} = \frac{Q_0}{4\pi^2 k_z} \frac{(1-R)\beta}{(1-R^2 e^{-2\beta l_s})} \int_{-\infty}^{\infty}\int_{-\infty}^{\infty} d\lambda_f d\eta_f e^{-i(\lambda_f x + \eta_f y)} \frac{e^{-({\lambda_f}^2 + {\eta_f}^2)a^2/8}}{({\beta_f}^2 - \beta^2)} \times$$

$$\left[\frac{A_0 e^{\beta_f z}+B_0 e^{-\beta_f z}}{E_0}+e^{-\beta z}-Re^{-2\beta l_s}\left(\frac{A_1 e^{\beta_f z}+B_1 e^{-\beta_f z}}{E_0}+e^{\beta z}\right)\right] \tag{2.59}$$

where,

$$A_0 = e^{-\beta_f l_s}\left(\beta_f-\frac{h}{k_z}\right)\left(\beta+\frac{h}{k_z}\right)+e^{-\beta l_s}\left(\beta_f+\frac{h}{k_z}\right)\left(-\beta+\frac{h}{k_z}\right),$$

$$B_0 = e^{\beta_f l_s}\left(\beta_f+\frac{h}{k_z}\right)\left(\beta+\frac{h}{k_z}\right)+e^{-\beta l_s}\left(\beta_f-\frac{h}{k_z}\right)\left(-\beta+\frac{h}{k_z}\right),$$

$$A_1 = e^{-\beta_f l_s}\left(\beta_f-\frac{h}{k_z}\right)\left(-\beta+\frac{h}{k_z}\right)+e^{\beta l_s}\left(\beta_f+\frac{h}{k_z}\right)\left(\beta+\frac{h}{k_z}\right),$$

$$B_1 = e^{\beta_f l_s}\left(\beta_f+\frac{h}{k_z}\right)\left(-\beta+\frac{h}{k_z}\right)+e^{\beta l_s}\left(\beta_f-\frac{h}{k_z}\right)\left(\beta+\frac{h}{k_z}\right),$$

$$E_0 = e^{-\beta_f l_s}\left(\beta_f-\frac{h}{k_z}\right)^2-e^{\beta_f l_s}\left(\beta_f+\frac{h}{k_z}\right)^2$$

Now, if the sample is semitransparent to infrared spectrum, the signal obtained by the IR detector is not only due to the surface of the sample but also because the bulk. Defining γ_e as the effective infrared absorption coefficient of the sample, the signal obtained in Laplace terms will be:

$$T(x,y,z,s) = A_2\int_0^{ls}\gamma_e\, e^{-\gamma_e z}\overline{T(x,y,z,s)}dz \tag{2.60}$$

where A_2 is a variable that depends on several parameters involved in the experimental methodology. Substituting the Equation 2.59 in 2.60 and applying the inverse Laplace transform to that expression, the IR signal obtained by the detector for an anisotropic sample becomes [41],

$$T(x,y,0,t) = \frac{2Q_0(1-R)}{\pi}A(t)\frac{e^{-\frac{2x^2}{a^2+8\alpha_x t}}}{\sqrt{a^2+8\alpha_x t}}\frac{e^{-\frac{2y^2}{a^2+8\alpha_y t}}}{\sqrt{a^2+8\alpha_y t}} \tag{2.61}$$

in which the function $A(t)$ depends on the relatives values of the characteristic lengths of the sample (thickness, optical absorption length and thermal diffusion length). The cases of particular interest are:

Thermally thick and optically opaque sample.

$$A(t) = \frac{1}{e_z}\left[\frac{1}{\sqrt{\pi t}} - \frac{h}{e_z} e^{(h/e_z)^2} Erfc\left(\frac{h}{e_z}\sqrt{t}\right)\right] \quad (2.62)$$

Thermally thin and optically opaque sample.

$$A(t) = \frac{1}{\rho c l_s} e^{-\frac{2ht}{\rho c l_s}} \quad (2.63)$$

Thermally thick and optically semi-transparent sample.

$$A(t) = \frac{1}{\rho c}\frac{\beta\gamma}{\beta+\gamma} \quad (2.64)$$

It is important to mention that in the case of isotropic samples the thermal diffusivity and conductivity are the same in all directions ($\alpha_x = \alpha_y = \alpha_z$; $k_x = k_y = k_z$), so that Equation 2.61 remains valid.

In-plane Thermal diffusivity. The $T(x, y, 0, t)$ signal suggests a Gaussian profile along the *x,y* axes whose radius is given by ${a_i}^2 = a^2 + 8\alpha_i t$, with *i*=*x* and *y*. The in-plane thermal diffusivity of the sample along its main axes *x, y*, is obtained from the curve ${a_i}^2$as a function of *t* (Different times after the laser pulse), which turns out to be a straight line whose slope will be $m = 8\alpha_i$. This method is valid for homogeneous and in-homogeneous slabs regardless of their optical properties and thickness, and it is not affected by heat losses due to convection and radiation mechanisms.

2.4 Transient Hot Wire Method

The Transient Hot Wire (THW) is part of a group of methods that employ a transient heat flow to determine the thermal conductivity, *k*, of a substance. It is based on heat transfer by conduction and has been extensively applied to the study of liquids, powders and gases since1931, when it was proposed by the first time by Stalhane and Pyk [42]. In this method, the heat is supplied by a controlled source to the material to be studied and measurement of the temperature change caused by dissipation of heat through the material allows to determine the thermal transport properties of the material [43]. Specifically, the THW consists of a cylindrical container in which the substance to be investigated is located and on which an electrical conductive wire with known

properties is immersed (Figure 2.10). A constant electric current is passed over it, producing a Joule heating effect. The heat is dissipated to the sample by conduction and it is possible to determine the *k* of the substance by analyzing the temperature of the wire (sensor and heat source) as a function of time [44].

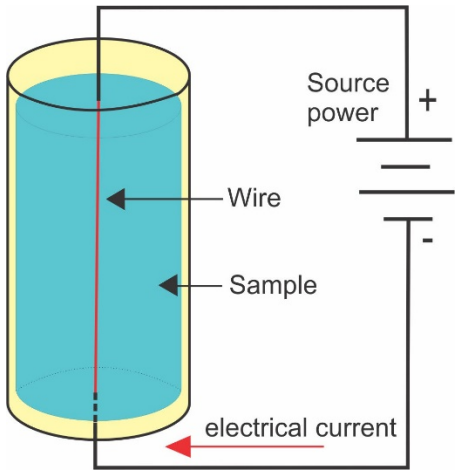

Figure 2.10 Cylindrical container cross-section view.

Hot wire model. The theory describing the heat transfer that takes place in the THW considers an infinitely long and thin linear heat source, with a uniform temperature distribution that transfers heat by conduction to a homogeneous and infinite medium. Starting from Equation 1.15 and re-expressing it in cylindrical coordinates for the radial coordinate *r*, one has:

$$\frac{1}{r}\frac{\partial}{\partial r}\left(r\frac{\partial T}{\partial r}\right) = \frac{1}{\alpha}\frac{\partial T}{\partial t} \tag{2.65}$$

here, $T = T_o + \Delta T$ is the temperature of the substance at time *t*, T_0 is the initial temperature, and ΔT is the temperature variation of the substance when it is heated. The boundary conditions of the problem will be:

$$\lim_{r_a \to 0}\left\{r_a\left(\frac{\partial T}{\partial t}\right)\right\} = -\frac{q_l}{2\pi k} \qquad t = 0; r_a = 0 \tag{2.66}$$

$$\lim_{r_a \to \infty}\{\Delta T(r_a, t)\} = 0 \qquad t \geq 0; r_a = \infty \tag{2.67}$$

where q_l is the heat flux per unit length. The solution to Equation 2.65 subjected to the boundary conditions given by Equations 2.66 and 2.67 is well known. For sufficiently large measuring times, such that $t>>r_a^2/\alpha=\tau$, where r_a is the radius of the wire, and neglecting heat losses by convection and radiation, the temperature variation as a function of time is given by:

$$\Delta T(t) = \frac{q_l}{4\pi k}\left[\ln\left(\frac{4\alpha t}{{r_a}^2}\right) - \gamma\right] \tag{2.68}$$

here γ=0,5772 is Euler's constant. The wire can act as a temperature sensor if its electrical resistance is measured according to

$$R(t) = R_o(1 + \mathcal{J}\Delta T) \tag{2.69}$$

in which $\mathcal{J}$ is the temperature coefficient of the electrical resistance and R_o is the initial resistance of the wire. If a constant electric current, I, circulates through the wire over time, there is a heating of the wire and therefore variations in its resistance, which by *Ohm's law* will produce voltage variations over time. The latter will be given by:

$$V(t) = R(t)I = R_o\big(1 + \mathcal{J}\Delta T(t)\big)I = Vo + R_o I\mathcal{J}\Delta T(t) \tag{2.70}$$

where $V_o=R_0 I$. Now, substituting Equation 2.69 in 2.70, we have:

$$\Delta V(t) = V(t) - Vo = R_o I\mathcal{J}\frac{q_l}{4\pi k}\left[\ln\left(\frac{4\alpha t}{{r_a}^2}\right) - \gamma\right] \tag{2.71}$$

where $q_l=I^2R_o/L_w$, and L_w is the length of the wire. From Equation 2.71 it can be seen that the slope of the linear region of the curve $\Delta V(t)$ Vs. $\ln(t)$, is:

$$m = \frac{I^3 R_0^2 \mathcal{J}}{4\pi k L_w} \tag{2.72}$$

A multi-current approach described elsewhere [44] is used here to allow that the selected linear region is the one that matches the conditions imposed by the theoretical model associated to the technique. In this approach, the ΔV as a function of $\ln(t)$ curves are recorded for several values of the electrical current, I. Then, the slopes m of the linear regions of these curves are calculated and plotted as a function of I in a double logarithmic graph. If, according to Equation 2.72 the slope of this graph is near to three,

then one can be sure that the selected linear regions in the curves of ΔV versus $\ln(t)$ are those in which the conditions imposed by the theoretical model are well satisfied. One can see from Equation 2.72 that the m versus I^3 graph becomes a straight line with a slope given by

$$b = \frac{R_0^2 \mathcal{J}}{4\pi k L_w} \tag{2.73}$$

from which the thermal conductivity can be obtained straightforwardly if R_0, L_w, and $\mathcal{J}$ are well known.

CHAPTER 3

THERMAL CHARACTERIZATION OF HEPTANE/ISOOCTANE MIXTURES

3.1 Particular objective.

To measure the thermal properties of heptane/isooctane mixtures in the liquid as a function of its octane number, as well as the gas phases of the pure components, in order to achieve certification rules for octane number rating.

3.2 Introduction.

The third chapter of this manuscript was motivated by the importance of the thermal properties of n-alkenes (C_nH_{2n+2}) in the petrochemical industry for the optimization of combustion processes and energy efficiency. For example, the development of a standard fuel rating system is based upon the fuel detonation characteristics on a special single engine with a variable compression ratio. Two pure substances were arbitrarily chosen to calibrate the test machines, namely isooctane (n=8, one of the branched carbon chain isomers of octane, the straight chain of 8 carbon atoms with no branching) and heptane (n=7), to which “octane” numbers of 100 and 0 have been assigned [45], respectively, being “octane” a general term used to indicate a fuel ability to resist engine knock. The sensitivity of the fuel rating parameters on the thermodynamic parameters has inspired the use of thermal properties, in particular the thermal diffusivity, as figure of merit for fuel characterization. Cardoso *et al* [46] and Lima *et al.*[47] used a thermal wave interferometer (TWI) or thermal wave resonator [48] to measure the thermal diffusivity of the air/fuel vapors mixtures (hexane/isooctane) that then correlated with the octane number [6]. The use of hexane instead of the widely used heptane was justified by the simple reason that a larger variation of thermal diffusivity as a function of concentration was observed for mixtures of hexane/isooctane than for mixtures of heptane/isooctane. The fact that very little

difference was observed in the value of thermal diffusivity for air saturated with the heptane and isooctane vapors is further investigated in this work by measurements of thermal conductivity for the same kind of samples. Also measurements of the thermal transport properties of heptane/isooctane mixtures in the liquid phase at room temperature and atmospheric pressure were performed. The thermal conductivity was measured using the THW method and the thermal effusivity was determined by the FPPE technique. Then, the thermal diffusivity and the heat capacity per unit volume were calculated respectively using the well-known relationships $\alpha=(k/e)^2$ and $C=e^2/k$. It is shown that a correlation between these parameters and the relative concentration of the mixtures components (i.e. the octane number) exists, and that the obtained thermal parameters proved to be sensitive to detect molecular associations in binary hydrocarbon liquid mixtures.

3.3 Experimental set-ups

3.3.1 Hot wire system

The heat source is a 76.2 µm diameter platinum wire (*Alfa Aesar*) of length L=70.5 mm, mounted on a Teflon support that is introduced into a 15 cm long and 3.54 cm diameter glass cylindrical container. For measurements in the liquid phase the whole wire is covered by the sample, whereas for vapor phase measurements 1 mL of the liquid sample are carefully deposited below the wire´s support as shown schematically in part b of the Figure 3.1.

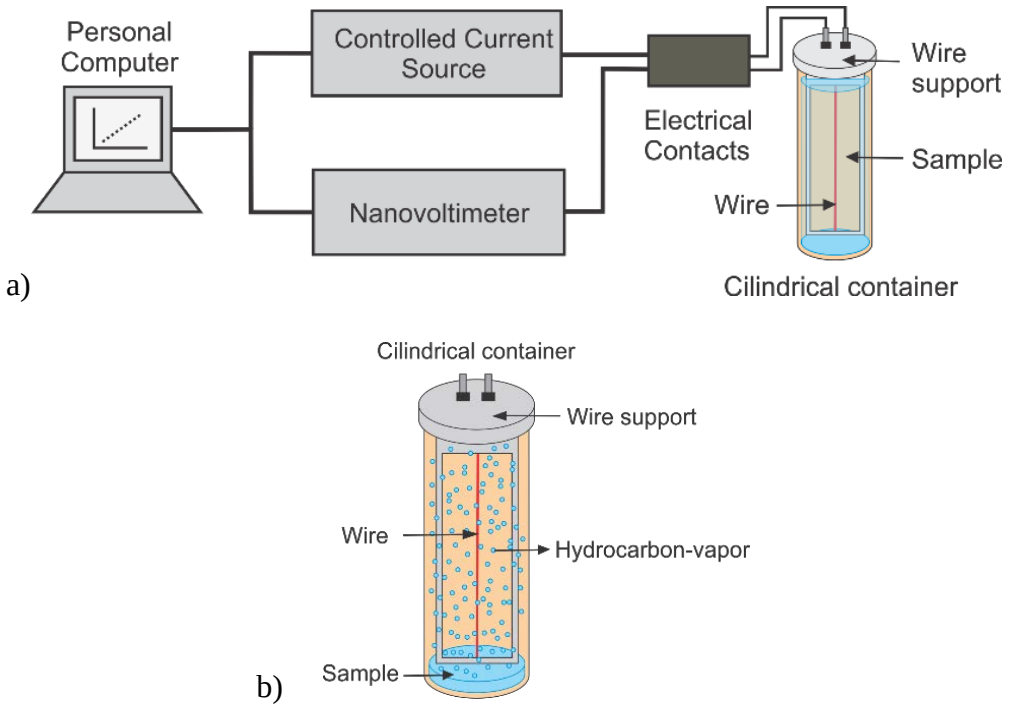

Figure 3.1 a) Schematic diagram of the experimental set-up for the hot wire system; b) Sample container for measurements in gas phase.

The wire is heated by Joule´s effect using an electrical current stabilized power supply (Keithley 2400) and the voltage drops are measured with a nanovoltmeter (Keithley 2182A). The sample container is thermally stabilized at 295 K (room temperature) using a commercial thermal bath (Julabo FP50) not shown in the Figure 3.1 The experimental system was previously tested by thermal conductivity measurements in samples of air, distilled water, glycerol, ethylene glycol and methanol (see Table 3.1). Obtained values for these well-known samples are given in Table 3.2.

Table 3.1. Samples used. All samples were used as provided, without further purification.

Chemical name	**Source** [49,50]	**Initial mole fraction purity / mol%**
Glycerol	J.T. Baker	99.9
Ethylene glycol	J.T. Baker	99.9
Methanol	J.T. Baker	99.9

n-pentane	Sigma Aldrich	98
n-hexane	Sigma Aldrich	≥ 95
n-heptane	Sigma Aldrich	99
n-octane	Sigma Aldrich	98
n-nonane	Sigma Aldrich	98
n-decane	Sigma Aldrich	98
Isooctane	Sigma Aldrich	≥ 99

Table 3.2. Thermal conductivity and effusivity measured with the Hot-wire and the Photopyroelectric Technique respectively for reference samples at room temperature, T = 295 K and atmospheric pressure, p = 0.077 MPa. The numbers after the sign ± represent the standard uncertainties. The maximum value for the relative standard uncertainty of k is 2% for the liquid samples; while this value is increased to 4% for air (it is a typical result for our hot wire experiments that uncertainties are greater for measurements in the gas phase than for liquid samples). Maximum value for the relative standard uncertainty of e is 0.6%. The thermal effusivity of air is not reported because this substance was the reference sample used for thermal effusivity measurements in liquids.

Test sample	$\boldsymbol{k}$ ($Wm^{-1}K^{-1}$)	$\boldsymbol{k_{lit}}$ ($Wm^{-1}K^{-1}$)	$\boldsymbol{e}$ ($Ws^{1/2}m^{-2}K^{-1}$)	$\boldsymbol{e_{lit}}$ ($Ws^{1/2}m^{-2}K^{-1}$)
Distilled water	0.60±0.01	0.59 [44]	1592±10	1582 [27]
Glycerol	0.289±0.005	0.288 [44]	931±5	929 [51]
Ethylene glycol	0.254±0.005	0.252 [44]	810±4	805 [27]
Methanol	0.208±0.004	0.208 [44]	621±4	626[51]
Air	0.026±0.001	0.026 [7]	--	--

3.3.2 Front Photopyroelectric configuration

Figure 3.2 shows schematically our experimental system. The radiation source is a 660 nm semiconductor laser (LASEVER LSR660ML-600) of 100 mW power, whose intensity is periodically modulated (50% duty cycle) using the TTL output of a Lock-in amplifier (SR830 - Stanford Research Systems). A thin sheet of polyvinylidene

difluoride (PVDF) polymer foil [52] (52 μm thick, thermal diffusivity $\alpha_p = 0.58 \times 10^{-7}$ m^2s^{-1} [26] and thermal effusivity e_p = 559.4 $Ws^{1/2}$ m^{-2} K^{-1} [53]) with a sputtered metallization at both sides was used as a PPE sensor. A lock-in amplifier was used for measuring the amplitude and phase of the signal as a function of the modulation frequency. The experimental system was calibrated by measuring the thermal effusivity of glycerol, distilled water, and ethylene glycol, whose thermophysical parameters are well-known (see Table 3.2 for calibration results). Sample aliquots of 500 μL were used in each measurement (the diameter and thickness of the liquid column were 0.75 cm and 1.13 cm, respectively). Measurements have been performed at room temperature (295 K) and great reproducibility was observed in a total of 10 measurements done for each sample.

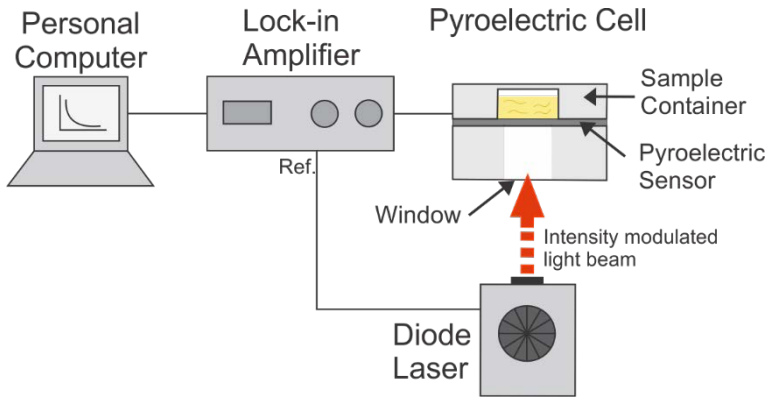

Figure 3.2 Schematic diagram for FPPE configuration.

3.4 Results and discussion

3.4.1 Measurements in the gas phase

The thermal conductivity of air saturated with vapors of n-alkanes was measured. Figure 3.3. shows results of a typical measurement for air saturated with isooctane vapor done following the multi current methodology outlined in the section 2.4. The voltage drop across the wire, ΔV, is plotted in Figure 3.3a as a function of $\ln(t)$ for several values of the heating current, I. The solid curves are the best least squares linear fit results. The slopes, m, obtained from these fits are represented in Figure 3.3b as a function of I^3. Again, the solid curve is the best least squares linear fit result, from whose slope thermal conductivity is calculated using Equation 2.73.

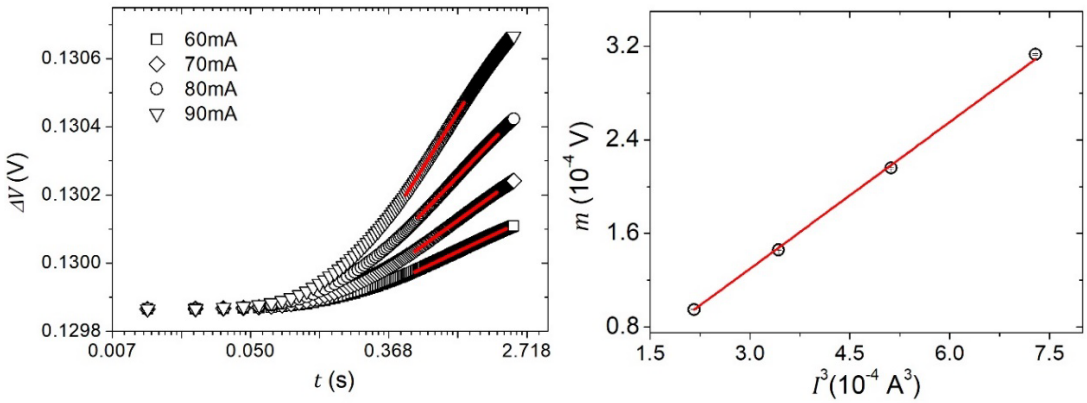

a) b)

Figure 3.3 a) Voltage drop, ΔV, as a function of $ln(t)$ for several values of the heating current, *I*. The solid curves are the best least squares linear fit results; b) The slopes, *m*, obtained from the linear fits of Figure 3.3a, as a function of I^3. The solid curve is the result of the best least squares linear fit.

The obtained thermal conductivities as a function of the number of carbon atoms in the molecular chain, *N* are shown in Figure 3.4a and in Table 3.3. It can be seen that for the normal alkanes the thermal conductivity is proportional to *N*. However, the measured thermal conductivity of isooctane (triangle in Figure 3.4a) is near the value obtained for heptane, what supports previously reported results [39]. Note that both the normal alkane pentane and the branched alkane isooctane have five carbon atoms in the straight part of their carbon chains, even though both have quite different geometries. Although heat conduction in gas mixtures is a very complicated process depending on several factors, the obtained result can be explained taking into account the fact that heat conduction in gases is dominated by molecules diffusion during evaporation, and this mechanism depends on the vapor pressure of the liquid, defined as the equilibrium pressure of a vapor above its liquid in a closed container. Reported vapor pressures of some alkanes are shown in Table 3.3. It can be seen that heptane and isooctane show very similar values of this parameter, while it is quite different for the other alkanes.

Table 3.3. Thermal conductivities, k_{vapor}, obtained for air saturated with alkanes vapors at room temperature, T = 295 K and atmospheric pressure, p = 0.077 MPa (the numbers

after the sign ± represent the standard uncertainties). The maximum value for the relative standard uncertainty is 5%. Also shown are the vapor pressures [54] of the n-alkanes and isooctane (see Table 3.1 for purities), and the estimated molar fractions in their mixtures with air. All solvents were used as provided, without additional purification. The molar fractions were estimated under the ideal gas assumption as a ratio of the partial pressure of the evaporated component and the total pressure within the closed measurement cell.

Alkane	**Vapor pressure** (kPa) (at 295K)	k_{vapor} ($\times 10^{-3}$ $Wm^{-1}K^{-1}$)	**Molar fraction in its mixture with dry air** (mol%)
n-pentane	60.5	9.0 ± 0,6	44
n-hexane	17.6	14.4 ± 0.7	18.6
n-heptane	5.22	19.0 ± 0.8	6.35
n-octane	1.55	22.0 ± 0.9	1.97
n-nonane	0.53	24.6 ± 0.8	0.68
n-decane	0.19	25.8 ± 0.9	0.25
isooctane	5.52	20 ± 1	6.69

Figure 3.4b shows the correlation existing between the measured thermal conductivity and the vapor pressure of the alkanes. It can be noticed the proximity of the points corresponding to heptane and isooctane.

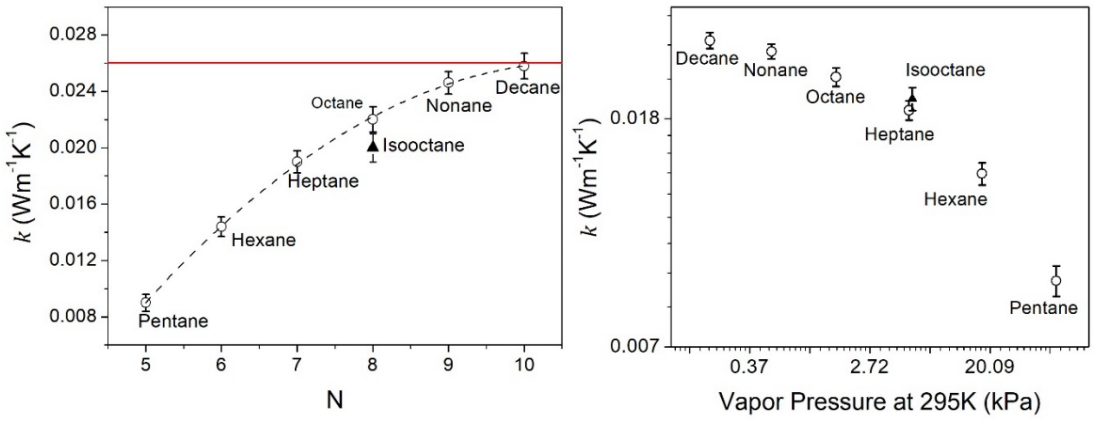

Figure 3.4 a) Thermal conductivity of air saturated with vapors of n-alkanes as a function of the number of carbon atoms in the straight part of the carbon atoms molecule chain. The value corresponding to air (solid line) is showed for comparison;

b) Thermal conductivity as a function of the vapor pressure (in a log-log scale for better visualization). A good reproducibility was observed in several measurements. Thermal conductivity uncertainties were calculated using the error due to the best least squares linear fit shown in Figure 3.3b and error propagation in Equation 2.73.

Notice that as N increases, k tends to the value corresponding to air (red line). This behavior can be explained using the same arguments given by Lima et al [55], if we consider that the measured thermal conductivity is an effective value for the vapor-air mixture and that the vapor molar concentration in air shows a considerable decrease with N. Table 3.3 also shows the calculated molar fraction in the mixtures of the hydrocarbon vapors with air in the hot wire cell with a total volume of 137.38 cm^3. For decane, this molar concentration becomes only 0.25 mol%, so that the measured conductivity is similar to that of the air (showed with a continuous line in Figure 3.4a).

3.4.2 Measurements in the liquid phase

Table 3.4 shows the measured values of thermal conductivity and effusivity, as well as the calculated values of thermal diffusivity and specific heat capacity for each isoctane mass fraction percentage in heptane, w_m, for mixtures in the liquid phase. Thermal conductivity was measured using the multicurrent approach described before for the THW method. Typical results are similar to those showed in Figure 3.3. A result of a typical FPPE measurement is shown in Figure 3.5. It is showed the normalized phase as a function of the frequency for a heptane/isooctane sample with w_m =40 w_mt%. As discussed elsewhere [29], the use of the normalized amplitude for fitting is rather complicated than fitting with the signal phase, so that the later was used here. In Figure 3.5 the red curve is the best least squares fit using Equation 2.23 leaving R_{sp} as a fitting parameter, from which sample´s thermal effusivity is calculated by means of Equation 2.24. Experimental error was obtained using the error due to curve fitting and error propagation in Equation 2.23. The very small uncertainties and the good reproducibility obtained in several repetitions are typical for measurements in liquid samples in which there is a very good thermal contact between sample and PPE detector. Literature available values at atmospheric pressure for the thermal conductivity of the pure compounds are indicated in Table 3.4. A good agreement is observed between

measured and literature reported values. The last column of the table shows values of the heat capacity per unit volume at constant pressure calculated from the available reported values of the molar capacities [56]. They are greater than our measured values, but it is worth to notice that uncertainties reported in Reference [56] span a very large range between 2 and 20 %.

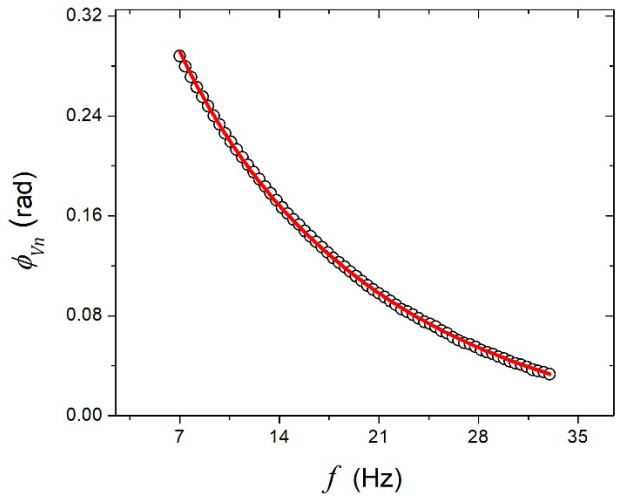

Figure 3.5 Normalized phase as a function of the light modulation frequency for a heptane/isooctane sample with w_m =40 w_mt%.

Table 3.4 Thermal properties at room temperature, T=295 K and atmospheric pressure, p =0.077 MPa for each isooctane mass fraction in heptane, w_m, for mixtures in the liquid phase. The numbers after the sign ± represent the standard uncertainties. e and k were measured by the FPPE and THW technique, respectively, while α and the C were calculated using the well-known relationships $\alpha=(k/e)^2$ and $C=e^2/k$, respectively. The maximum values for the relative standard uncertainties are 0.6%, 2%, 5%, and 3% for e, k, α and C, respectively. Literature available values are shown below the measured magnitudes for comparison.

[a] at 303 K and 0.1 MPa [57]. [b] at 298 K and 0.1 MPa [58]. [c] at 293 K and 0.1 MPa [59]. [d] at 298 K and 0.1 MPa [60]. [e] 303.6 K and 0.1 MPa [61]. [f] calculated from the values of the densities and molar heat capacities of the pure compounds and the molar heat capacities excess values reported in Ref. [56] at 298 K and 0.1 MPa.

w_m (w_mt%)	e ($Ws^{1/2}m^{-2}K^{-1}$)	k ($Wm^{-1}K^{-1}$)	α ($\times10^{-8}$ m^2s^{-1})	C ($\times10^6$ $Jm^{-3}K^{-1}$)
0	421±2	0.119±0.002 0.120±0.002 [a] 0.122±0.002 [b]	8.1±0.3	1.48±0.04 1.52 [f]
20	402±2	0.116±0.002	8.3±0.4	1.39±0.04 1.50[f]
40	385±2	0.113±0.002	8.7±0.4	1.31±0.04 1.48 [f]
60	374±1	0.107±0.002	8.1±0.3	1.31±0.03 1.47 [f]
80	367±1	0.104±0.002	8.0±0.3	1.29±0.03 1.45 [f]
100	359±2	0.096±0.002 0.095±0.002[c,] 0.095±0.001[d, e]	7.2±0.4	1.34±0.04 1.44 [f]

The graphs of thermal properties as a function of the isooctane concentration, w_m, in heptane for mixtures in the liquid phase are showed in Figure 3.6. Parts a, b, c and d correspond to thermal effusivity, conductivity, diffusivity and specific heat capacity, respectively, as a function of w_m. As mentioned before, the octane number in these mixtures correspond to the mass concentration of isooctane in heptane, being octane number 100 associated to the pure isooctane sample.

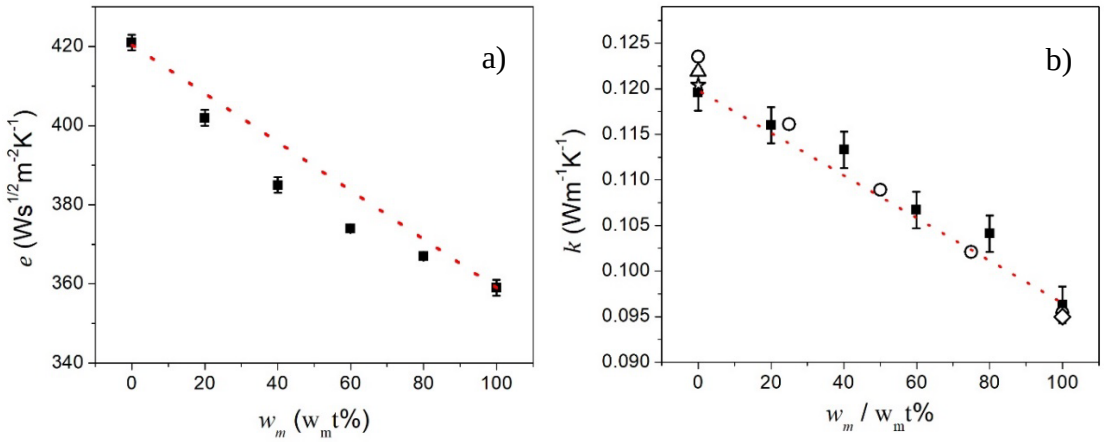

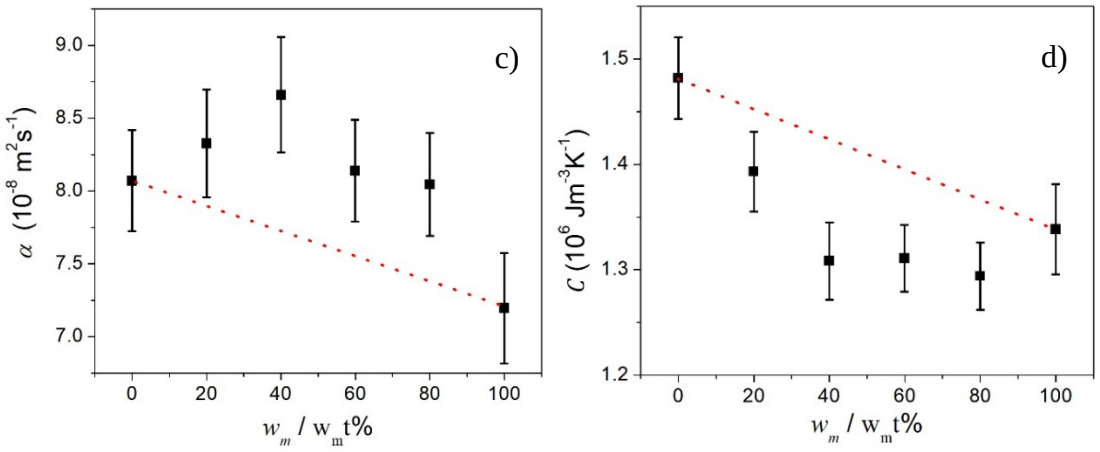

Figure 3.6 Thermal properties as a function of the isooctane mass fraction in heptane for mixtures in the liquid phase. a) *e*, b) *k*, c) α and d) *C*. ■ Experimental points, ▵ reference [57], ☆ reference [58], ◊ reference [59], ○ reference [62]. Relative uncertainties are about 2% in referenced points.

Dashed curves represent linear behavior of the thermal properties as a function of concentration expected for non-associative mixtures [63]. As it is well-known [29], concerning molecular association processes in binary liquid mixtures two classes of liquids can be defined: “interacting” and “non-interacting”. The second case leads to the so-called “non-associative” mixtures, for which values of the effective thermal properties can be calculated from those of the components using a rule of additivity, and deviations from the linearity are very small or even zero. In the case of associative mixing (interacting liquids), there is no model to predict the thermal properties behavior due to molecular associations [64] and deviations from linearity exist. As can be seen from the Figure 3.6, thermal effusivity and conductivity show a small deviation from the linearity when plotted against the relative concentration of the components, being therefore less sensitive to the effect of molecular associations than thermal diffusivity and specific heat capacity. However, although α and *C* seem to be more sensitive molecular associations, the fact that their calculated values are not so different from each other for the different concentrations indicates that these parameters do not allow to distinguish between the strength of the liquids interaction. Nonetheless, note

that the *k* and *e* measured values are different from each other at different relative concentrations of the binary liquid constituents.

Figure 3.7 shows the excess values curves for the four thermal properties calculated as

$$\frac{\Delta y_d}{y_d} = \frac{y_{lin} - y_{exp}}{y_{lin}} \tag{3.1}$$

where y_d represents the thermal property, y_{exp} is the measured value and y_{lin} the value obtained if the perfect additivity linear law for the mixtures is respected. Solid curves are only shown for visualization purposes. The observed behavior supports the idea that a process of molecular association is involved for this kind of mixture. Similar behaviors have been observed before for other liquid mixtures as a result of thermal properties measurement using the photopyroelectric technique [29,65,66,67,68].

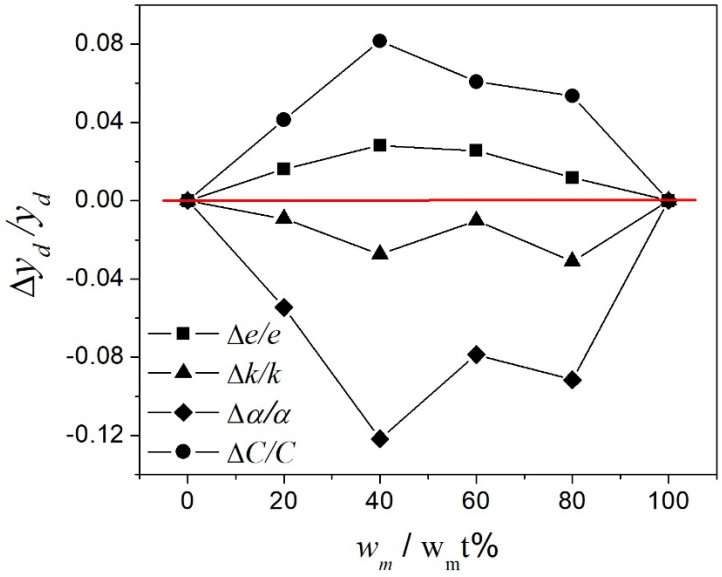

Figure 3.7 Excess values curves for the thermal properties as a function of the concentration for heptane/isooctane mixtures.

Note in Figure 3.7 that the highest excess value obtained is for the thermal diffusivity (~12%), followed by the specific heat capacity (~ 8%), while thermal effusivity and conductivity are less influenced by the excess values (only ~ 3%). This result confirms

those reported elsewhere [66] for systems that are notorious for forming molecular associations.

3.5 Conclusions

It was demonstrated that the four main transport thermal properties, namely thermal conductivity, diffusivity, effusivity and heat capacity per unit volume, allow the detection of molecular associations in binary hydrocarbon mixtures. This was proved for the case of mixtures of heptane and isooctane, substances that have been arbitrarily chosen before calibrating the octane number test machines. Indeed, a correlation has been found here between thermal properties and the octane number (namely the relative concentration of the components in the mixture). The well-known Transient hot wire technique for thermal conductivity measurements in liquids, aided with the less known front photopyroelectric technique for thermal effusivity, are good candidates for this kind of studies. It was also shown that the former technique is also suitable to study the effect on thermal conductivity of the diffusion of hydrocarbon vapor in air. We observed that the thermal conductivity of air saturated with n-alkane's vapors depends on the length of the linear chain of carbon atoms in the molecule, being almost the same for the normal alkane heptane and for the branched alkane isooctane.

CHAPTER 4

THERMAL EFFUSIVITY AND INFRARED ABSORPTION SPECTRA OF ORGANIC AND CONVENTIONAL COFFEE OIL

4.1 Particular objective.

To measure the thermal effusivity and optical absorption spectra in the IR of organic and conventional coffee oil samples in order to find a possible criterion for discrimination between these types of oil samples using photothermal techniques.

4.2 Introduction

Nowadays, the organic agriculture has a high demand due to the benefits that it offers for food safety and sustainability, due to the absence of pesticides and synthetic fertilizers [69,70]. The certification process that provides a guarantee of traceability and quality has facilitated the success of organic food in specialized markets [71]. There are companies that offer this kind of legitimization, such as Biotropico S.A., CERTIMEX S.C., SCS global services, CERES and BCS Oko-Garantie. Particularly in Colombia, the organic coffee certification improves the socioeconomic condition on the different actors in the productive chain, life quality and product sustainability [72]. Although the remunerations of organic agricultural practices are superior compared with those of conventional methods, normally the certification processes can be quite lengthy, complex and expensive, so that the potential economic profit of the small and medium producers is reduced and delayed. Due to this reason, there is a great interest for finding new certification methods [73]. In this context, the analysis of the thermophysical parameters are an alternative, since they are directly related to structure

and chemical composition of the material, which in the case of coffee beans depend on the environmental conditions, plant variety, soil types, etc [74,75,76,77].

The Thermal effusivity is a thermophysical property that plays a very important role in the thermal phenomena determining the behaviour of thermal waves at surfaces and interfaces [78] and the sample's thermal impedance value. This thermo-physical parameter has been used before to characterize the quality of foods [29,79,80], among other applications.

The PPE technique has been emerged as one of the most useful methods for thermal characterization of materials [26]. Two main configurations exist. In the First one, the back detection (BPPE) configuration, [81] an intensity modulated light beam impinges on the front surface of a sample and a pyroelectric sensor is attached to the rear side. This is a heat transmission configuration widely used for thermal diffusivity measurements. In the second variant, the FPPE, the sample is attached to the rear side of the sensor and the light beam impinges on the sensor front face, so that the sensor acts as both a source of thermal waves propagating through the sensor-sample system, and as the detector of them. Both configurations were described in section 2.2. The FPPE configuration is one of the most used techniques for measuring the thermal effusivity of liquid substances due to several factors, among them the small quantity of sample required and the excellent thermal contact achieved between sample and pyroelectric detector. This photothermal method has been used, among others, to differentiate between corn, soy and avocado vegetable oils [82,83,84]. This fact inspired the present work that explores the potential of the PPE technique for discriminating between organic and conventional coffee oils by measuring their thermal effusivity. This study is aided with measurements of the acidity index and density of the oil. The gas chromatography technique was used to identify the purity level of the extracted coffee oil and the fatty acids. Mid- Infrared Fourier Transform Photoacoustic Spectroscopy (FTIR-PAS) aided by Principal Components Analysis (PCA) [85,86] was used to find possible changes in functional groups due to the type of coffee farming.

4.3 Experimental and details

4.3.1 Coffee oil samples

Fruits from organic and conventional *Coffea arabica* plants (Caturra variety) were collected in farms, which are located in Risaralda-Colombia between 1500 and 1700 meters above the sea level. The samples were identified as shown in Table 4.1. All samples were subjected to the same wet pulping process [87] for reducing possible differences in the beans due to the post-harvest treatments. After drying process, the moisture content of the coffee beans was 12 %.

Table 4.1. Characteristics of the coffee samples.

Sample	Type of crop	Altitude (m)
C1	Conventional	1682
C2		1591
O1	Organic	1639
O2		1591

Oil extraction was made by the Soxhlet Method [88] using a SCHOTT DURAN apparatus. The coffee in parchment was dried in an air-circulating oven for 6 hours at 378 K to achieve a moisture content of 5 %. The coffee beans were grinded and then the particles with diameters between 500 and 710 μm were mechanically separated using Test Sieves ASTME11 SERIES 6083992 and 6093828, respectively; 150 g of the coffee powder and hexane (EMSURE ACS – 96%) were used in the solvent extraction method. The hexane was subsequently removed using a rotary evaporator (N-1110 EYELA). The density and acidity index were determined using the Colombia's standards NTC 336 (2016) [89] and NTC 218 (2011) [90], respectively.

4.3.2 Gas chromatography

The lipid compounds analysis of coffee oil was done using a commercial gas chromatography coupled to mass spectrometry (GC-MS - QP2010 ULTRA, SHIMADZU) with a C18 column (length: 60 mm, inner diameter: 0.32 mm) and hydrogen carry gas with flow of 40 mL min^{-1}. An initial temperature of 373 K was programmed for 4 min, after which it was elevated to 513 K at a rate of 3 K min^{-1} and kept constant for 10 min. The sample quantity was 1 μL and the volatile compounds

were determined using the library present in the device. According to the Colombian Technical Standards[91], a trans-methylation process of acid-catalyzed glycerides was applied to the sample before the measurement.

4.3.3 Fourier Transform Infrared Photoacoustic Spectroscopy (FTIR-PAS)

A commercial spectrophotometer (IR Prestige-21 – SHIMADZU) was used to obtain the optical absorption spectra in the mid-infrared range of the electromagnetic spectrum between 400 to 4000 cm^{-1}, and a commercial photoacoustic (PA) cell (MTEC300) with a KBr window was used as the signal detector. The PA cell internal chamber was purged with Helium for reducing the water vapor and CO_2 presence [92]. This enhances the signal/noise ratio and avoids spectral interferences, which ensures the reproducibility of the measurement. The oil amount deposited in the sample holder was 100 µL and 100 scans per sample were done to guarantee the data reliability. A simple schematic diagram representing the coupling of PA cell and spectrophotometer is shown in Figure 4.1.

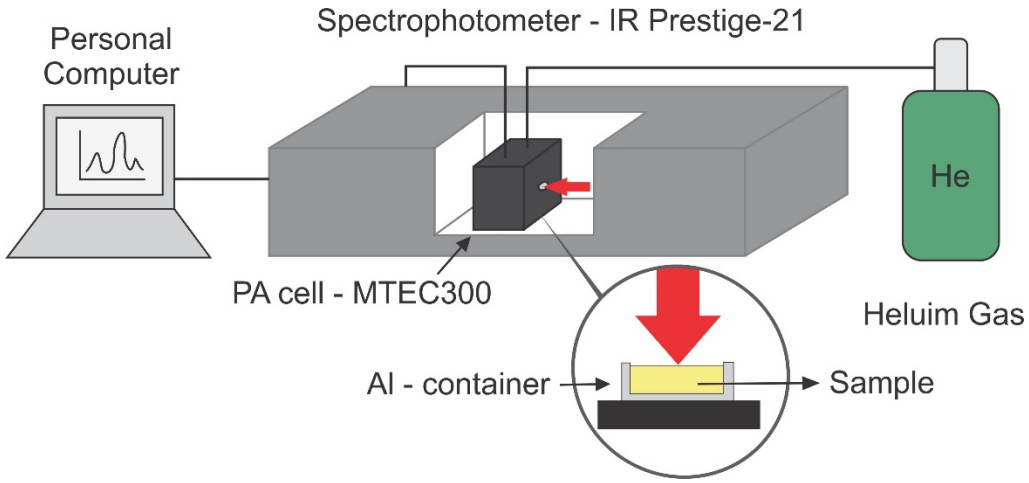

Figure 4.1 Schematic diagram of the experimental set-up for FTIR-PAS.

4.3.4 Front Photopyroelectric configuration

Figure 4.2 shows a schema of the experimental system. It is a scheme similar to the one presented in Figure 3.2, with the main difference that here an external modulator was used to modulate in intesity the light beam provided continuously by the laser. The radiation source is an Argon ion laser (Modulaser, Stellar-Pro) of 20 mW power at a wavelength of 488 nm and this light beam is modulated in intensity by an acousto-optic

modulator (MT110 A1-VIS, AA-Opto-Electronics). A thin sheet of PVDF [52] (52 µm thick, thermal diffusivity α_p = 0.58 × 10^{-7} m^2s^{-1} and thermal effusivity e_p = 559.4 $Ws^{1/2}$ m^{-2} K^{-1}) was used as PE sensor. The sputtered metallization on both sides consists of a 70 nm thick copper layer covered with a 10 nm thick nickel film, as stated by the manufacturer. A lock-in amplifier (SR830 - Stanford Research Systems) was used for measuring the amplitude and phase of the signal as a function of the modulation frequency. The experimental system was calibrated by measuring the thermal effusivity of glycerol (J.T. Baker 99.9 %), distilled water, ethylene glycol (J.T. Baker 99.9 %), and castor oil (Profinas Ltda), whose thermophysical parameters are well-known.

500 µL of oil were used in each measurement. In order to ensure reproducibility and minimal systematic error, 10 measurements per sample at room average temperature (300 K) were done.

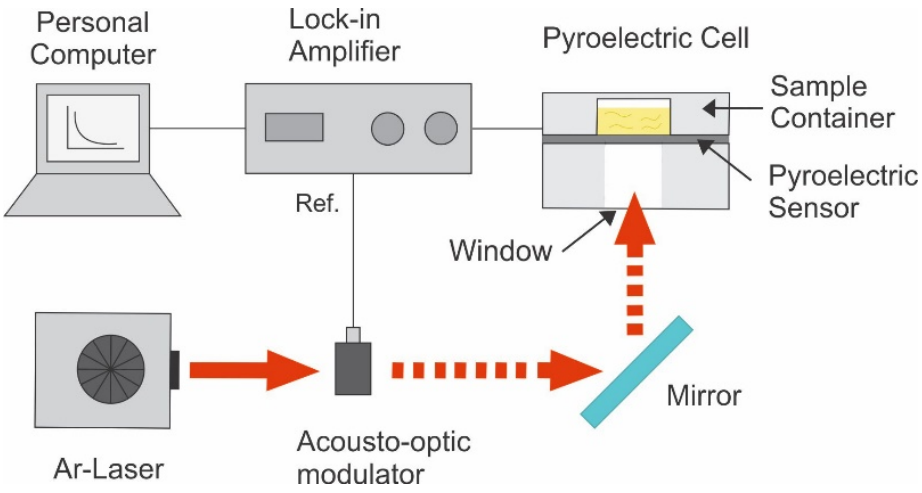

Figure 4.2 Schematic diagram for FPPE configuration using acousto-optic modulator.

4.4 Results and discussion

In all experiments described here, 10 measurements were performed for each group mentioned in Table 4.1.

4.4.1. Extraction yield

In the oil extraction from organic and conventional coffee samples (*coffea arabica* - Caturra variety) by the Soxhlet method, the minimum extraction time of five hours was

determined experimentally by considering the specific instrumental component and reagents. During this time, 70 cycles were achieved, enough to remove the solvent soluble substances. The extraction yield of each sample is shown in Table 4.2. The obtained values were between 12.6 and 14.4 %, in agreement with the reports of others authors [93,94]. The samples were stored in amber glass bottles at room temperature to prevent possible effects of photo-oxidation.

4.4.2. Density

The density of the samples was measured using a pycnometer. The obtained values are shown in Table 4.2, which are of the same order of magnitude as other reported coffee oil data [95,96].

4.4.3. Acidity index

The mass of potassium hydroxide necessary to neutralize the free fatty acids in 1g of coffee crude oil was used to find the fatty acids percentage. This procedure was done in triplicate in order to corroborate the data reproducibility. The obtained values between 1.11 and 1.27 % are shown in Table 4.2, indicating a low presence of fatty acids in all samples according to the Colombian Technical Standard NTC 218 (2011), which define a range between 1 and 4 % of fatty acids in vegetable oils with these features.

Table 4.2 Results of extraction yield, density and fatty acids percentage.

Sample	Extraction yield (%)	Density (g/mL)	Fatty acids (%)
C1	13.9	0.933±0.001	1.27±0.05
C2	14.4	0.940±0.001	1.23±0.08
O1	12.6	0.921±0.001	1.24±0.03
O2	13.5	0.927±0.001	1.11±0.08

4.4.4. GC-MS

GC-MS was used to confirm the adequate extraction of the coffee oil by means of the identification of lipid compounds. Table 4.3 shows the result of the retention time and chromatographic peak area corresponding to seven fatty acids that were identified in the samples of conventional and organic coffee oils using GC-MS.

In both cases (organic and conventional), the majority of the compounds were palmitic and linoleic fatty acids (79 % average). These values are in agreement with those reported by [97], but small differences may be related to minimum impurities in the column and perhaps to hexane (96 %-purity) traces, which would have been added in the extraction of the methyl esters.

Table 4.3. Fatty acids composition of coffee oil by GC-MS.

Maximum	Fatty acid	Average retention time (min)	Average area (%)	
			Organic coffee oil	Conventional coffee oil
1	Palmitic	33.85	42.2	41.8
2	Linoleic	39.07	37.2	37.2
3	Oleic	39.23	9.3	9.2
4	Elaidic	39.38	0.7	0.7
5	Stearic	40.04	6.9	7.5
6	Araquidic	45.78	2.9	2.9
7	Behenic	51.11	0.7	0.7

4.4.5. FTIR-PAS and PCA

There are not substantial differences between the FTIR-PAS spectra obtained for the conventional and organic coffee oil samples. A typical FTIR-PAS spectrum from an organic coffee oil sample is shown in Figure 4.3. The functional groups and modes of vibration are shown in Table 4.4, according to the most observed prominent peaks. The FTIR-PAS spectra of each sample, organic and conventional oil, showed maximum values at the same wavenumbers. The absorption bands positions in the spectra agree with those reported elsewhere [98,99,100,101].

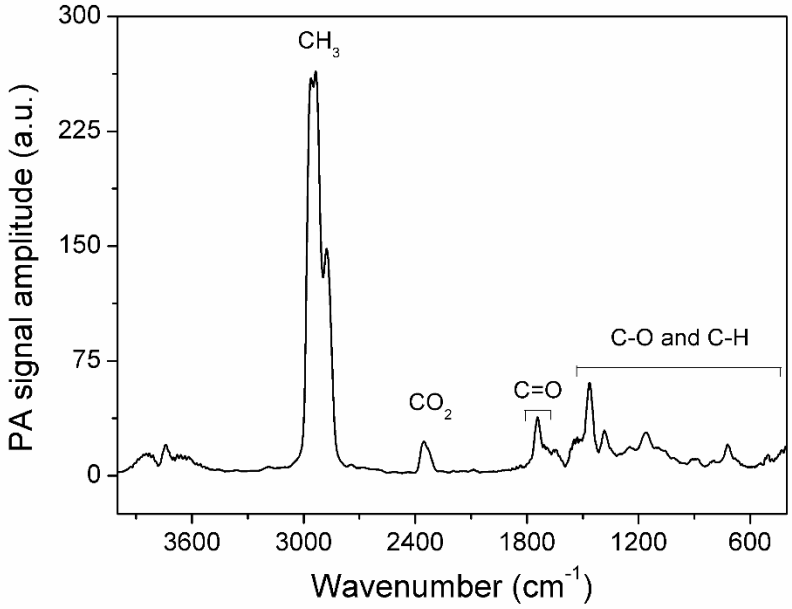

Figure 4.3 FTIR-PA spectrum obtained from an organic coffee oil sample group O2.

A weak peak between 3800 and 3100 cm^{-1} was attributed to O−H bonds, indicating the absence of free radicals and therefore low acidity. The bands between 2954 and 2854 cm^{-1} correspond to CH_3 and CH_2 groups, identifying representative linear hydrocarbon chains of the fatty acids that constitute the oil. The band at 2355 cm^{-1} was associated to CO_2. It is probably due to fails during the purging of the cell. The peak at 1747 cm^{-1} corresponds to the ester carbonyl of the triglycerides or phospholipids (C=O), while the peak at 1651 cm^{-1} can be related to the content of polyunsaturated fatty acids in the molecule. On the other hand, the "fingerprint" of the sample is within the ranges from 1500 to 800 cm^{-1}, in which small differences in the structure and constitution of the molecule are manifested [102,103]. The C−H and CH_3 bending of the methylene group are related to the absorption bands at 1465, 1377, 1240 and 1161 cm^{-1}, while the band at 1116 cm^{-1} is attributed to C−O extension of the ester group in the triglycerides molecule. Finally, the peak around 719 cm^{-1} is representative of the presence of carbohydrate radical from triglyceride structure of oils.

Table 4.4. Optical absorption bands in the mid-infrared spectral region from FTIR-PA spectra.

Absorption band (cm^{-1})	Assignments	
	Wavenumber range (cm^{-1})	Functional group
3741,3650	3800-3100	O-H (Stretching)
2954	2989−2949	-C-H (CH_3) (Stretching -asym)
2926	2949−2881	-C-H (CH_2) (Stretching -asym)
2854	2881−2780	-C-H (CH_2) (Stretching –sym)
2355	2250-2390	O=C=O (CO_2) (Stretching-asym)
1747	1850-1677	-C=O (free fatty acid) (Stretching)
1651	1667-1625	C=C (cis) (Stretching)
1465	1486-1446	-C−H (CH_2) (Scissoring)
1377	1390-1371	-C-H (CH_3) (Bending-sym)
1240	1290-1215	-C-H(CH_2) (Bending)
1161	1215-1147	-C-H (CH_2) (Bending)
1116	1127-1111	-C-O (ester) (Stretching)
719	802-630	-$(CH_2)_n$- (Rocking)

In order to visualize differences between the spectra of organic and conventional coffee oils, the PCA was applied. This statistical procedure gives an explanation to the data variance with relation to non-correlated variables called principal components. The PCA is widely used for identifying differences that are no easy to find directly in a study with multiple variables [85,102]. Considering the altitude and the farming system from twenty spectra of each sample the couples C1-O1 and C2-O2 were analyzed. From Figure 4.4 the clusters of points were identified in the score plots corresponding to the comparison of the first derivative spectra of the samples. This mathematical operation over the spectra was used to compare the shape, not the intensity, of the PA detection that can be affected by the sealing of the PA cell.

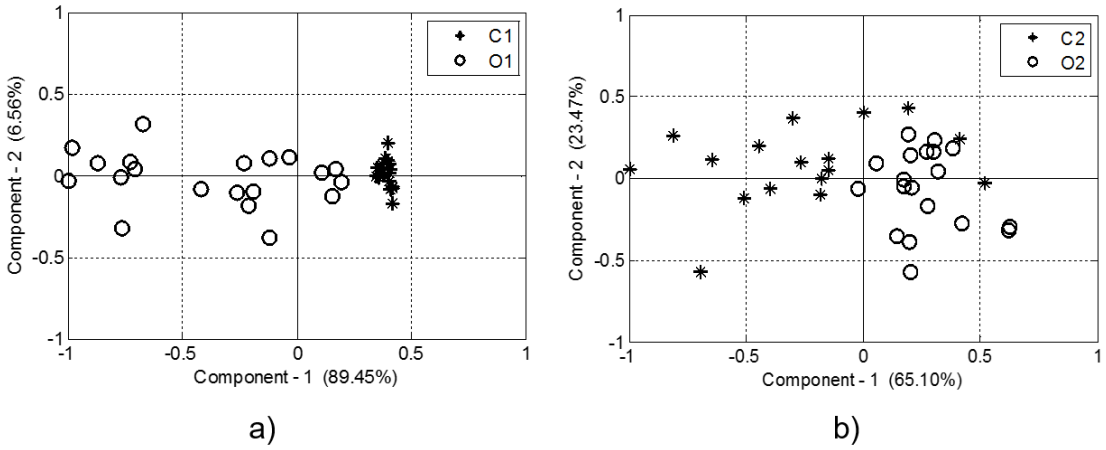

Figure 4.4 Score plots from the PCA applied to spectra of the samples: a) C1 and O1, and b) C2 and O2. * - conventional samples; o - organic samples.

Figures 4.4a and 4.4b show the distribution of the spectra in the space of the first and second component, for each pair of samples. Components 1 and 2 explain the 96 % of the variance of C1 and O1 spectra and the 89 % of the variance of C2 and O2 spectra The point clouds associated to the oil spectra of conventional and organic coffee are visibly separated.

4.4.6. Measurements of thermal effusivity with the PPE technique

The thermal effusivity of the coffee oil was measured using the procedure described in Section 4.3.4. A typical result of PPE measurement is shown in Figure 4.5. The normalized phase as a function of the frequency for an organic coffee oil sample is shown. The solid curve is the best least squares linear fit using Equation 2.23, in which R_{sp} is the only one fitting parameter, from which sample´s thermal effusivity is calculated using Equation 2.24.

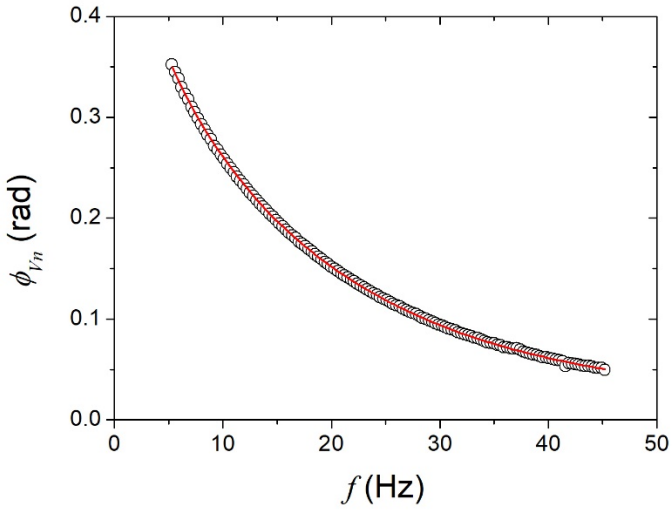

Figure 4.5 Normalized phase as a function of the light modulation frequency for an organic coffee oil sample.

Table 4.5 shows the mean values of 10 measurements of each oil sample that were extracted from organic and conventional coffee beans.

Table 4.5. Mean values of thermal effusivity of the coffee oil samples.

Sample	***e*** ($Ws^{1/2}m^{-2}K^{-1}$)
C1	604±4
C2	610±4
O1	592±3
O2	597±5

From this Table, it is possible to see that the thermal effusivity values are influenced by the farming system, organic or conventional, which could be used as support for the certification processes. To the best of our knowledge, there are no reported values of the thermal effusivity of coffee oils. However, the parameters obtained in this work are similar to those reported for castor oil (638 $Ws^{1/2}m^{-2}K^{-1}$ [104]), soy (614 $Ws^{1/2}m^{-2}K^{-1}$ [82]), grape seeds (526 $Ws^{1/2}m^{-2}K^{-1}$ [83]) and avocado (568 $Ws^{1/2}m^{-2}K^{-1}$ [82]).

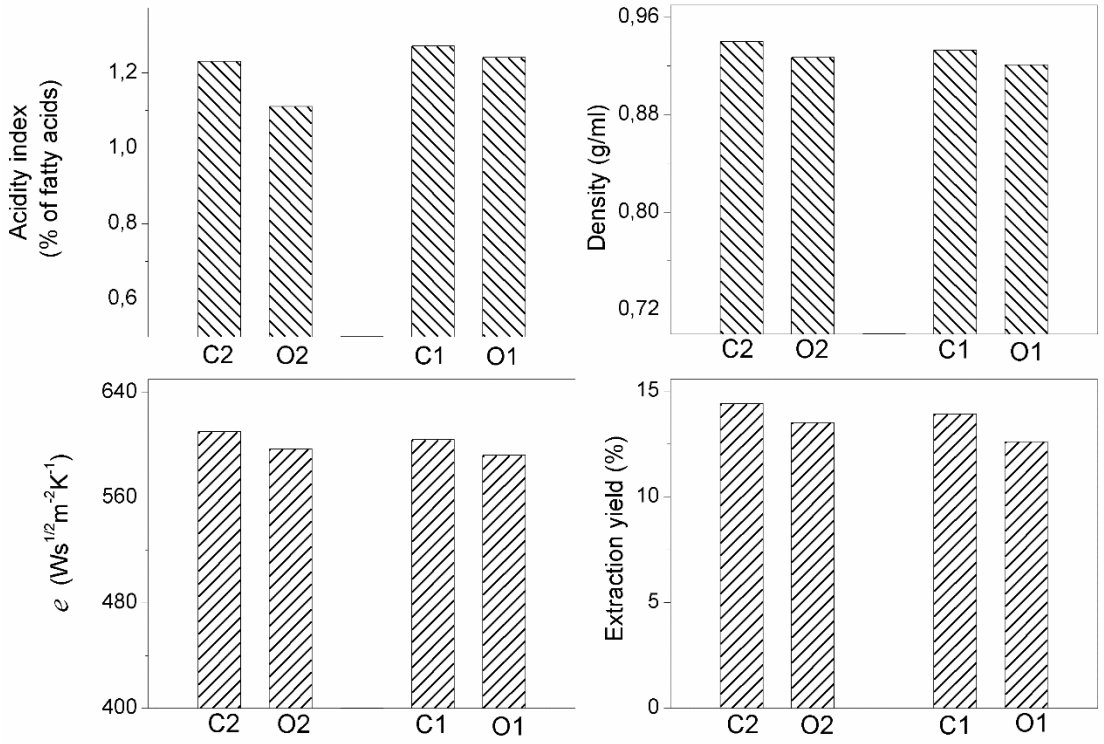

Figure 4.6 Examination of the thermal and physicochemical properties of coffee oils.

The comparative graphs in the Figure 4.6 show that the thermal effusivity, the extraction yield, the density and the acidity index of conventional coffee oil are larger than that of organic coffee oil.

4.5 Conclusions

In this work, the thermal effusivity of coffee oil is reported for the first time. The comparison of this parameter with other physicochemical properties demonstrates that it can be used as a criterion for traceability and discrimination between organic and conventional coffee. It has been also demonstrated that analyzing FTIR-PAS spectra with PCA allowed discriminating between these two kinds of samples. However, compared with IR spectroscopy, thermal effusivity measurements by the photopyroelectric method are simpler. The experimental set-up can be easily implemented in any laboratory using cheap instrumentation, samples loading and removal is simple, and the experimental set-up can be implemented in a portable

device, useful for in-field measurements. The here obtained results show the potential of the proposed procedure for the certification process of coffee.

CHAPTER 5

DETERMINATION OF THE WIDTH OF AN INFINITE INTERFACE BETWEEN TWO DIFFERENT SOLID MEDIA / THERMAL CONDUCTIVITY OF FLUIDS THAT FILL THE INTERFACE

5.1 Particular objective.

To determine the width at the vertical interface or crack between two different media using LIT with laser spot heating through its thermal contact resistance, as well as the thermal conductivity of fluids (gases and liquids) than fill the narrow interface.

5.2 Introduction

Narrow vertical cracks are difficult to detect using conventional nondestructive testing methods like Liquid Penetrant, Magnetic Particle, Eddy Currents, Industrial Radiography, Ultrasounds, and Electromagnetic Testing, among others [1]. Infrared thermography has been applied as a noncontact, nonintrusive and health safe method to detect near-surface defects by Kubiak [105]. Vibrothermography, Ultrasound excited thermography, has been widely used to detect closed fissures and characterization of shapes [106,107] but the main disadvantage of this technique is that the ultrasonic transducer must be in contact with the sample, which reduces its versatility. In a similar way, induction thermography uses electromagnetic pulses to launch eddy currents in electrical conductors. The eddy currents generate heat by resistive losses (Joule´s effect), which are larger at the crack position. The heat reaches the surface and can be detected by an infrared camera. Subsurface flaws produce local changes of the electrical current densities, which become visible in the thermographic

images [108,109]. This method is restricted to electrically conductive materials, which makes it a specific purpose technique.

Optically stimulated thermography is noncontact and applies to any kind of material, but the presence of the defect produces just a perturbation of the existing surface temperature field generated by the optical excitation. Moreover, the spatial shape of the illumination strongly affects the detectability of defects. In the case of vertical cracks, if the sample is excited by a homogeneous illumination producing a heat flux perpendicular to the sample surface, the crack will barely disperse the heat flux thus producing a negligible signature on the surface temperature distribution. Accordingly, to detect vertical cracks an asymmetry in the heat flux must be produced: this can be achieved by focusing laser spot close to the crack, whose thermal resistance partially blocks the heat flux, thus inducing an asymmetry in the temperature field at both sides of the fissure. This method was first used for imaging the presence of cracks [110,111]. In the last years, several approaches to characterize the crack (depth, length and width) have been developed. For instance, by solving numerically the heat diffusion equation in a homogeneous sample containing a vertical crack, the depth of the crack is retrieved [112,113]. On the other hand, analytical solutions of the surface temperature can be obtained for infinite cracks. By fitting the surface temperature measured by an infrared camera to the model, the thermal resistance of the crack is obtained [37].

In this chapter, the thermal contact resistance at the vertical interface between two different media was obtained following as reference the work developed by Pech-May et. al in which, they considered only one medium with an infinite vertical interface as it was shown in Section 2.3 [37, 11]. Here, the method proposed uses LIT with a laser spot heating, which provides amplitude and phase thermograms with a very low noise level. Considering an infinite interface, an analytical expression for the surface temperature is proposed. Due to the different thermal properties of the two materials, a singularity in the amplitude and phase of the temperature appears at the interface, even if the thermal contact is perfect. The lack of thermal contact at the interface adds a discontinuity in both amplitude and phase of the temperature. The goal is to measure the thermal contact resistance R_{th} at the interface, which quantifies its width through Equation 1.13. To do this, the experimental temperature profile across the interface is

fitted to the analytical model. In the same way, interfaces with previously calibrated widths were guaranteed to test the method. The agreement between the calibrated thickness and the retrieved R_{th} confirms the validity of the method, which could be useful to characterize the junction between two solids (e.g. welding) or in the quality control of contacts between different parts of composite materials.

In the second part of this chapter a method to measure the thermal conductivity of fluids (gases and liquids) using LIT with laser spot heating is proposed. This method consists of considering that the narrow interface between the two media is filled by some fluid. In the first part of this chapter it is assumed that the fluid that fills the interface that separates the two media was air. The Thermal Resistance values obtained for each calibration gap allowed to characterize its thickness using the thermal conductivity of the air in the known relation, $R_{th}=L/k_{air}$. Considering now that any fluid, other than air, completely fills the vertical interface and measuring the R_{th} across the interface at different known thicknesses, L, the thermal conductivity of the fluid can be determined from the slope of the straight line L vs R_{th}.

The most accepted method to measure the thermal conductivity of liquids and gases is the THW, described in Section 2.4. This technique shows high accuracy and it has the capacity to eliminate the errors due to convective effects that are always present in these samples, due to the existence of buoyancy forces. Among the limitations of the method are the difficulty to select the appropriate interval of the experimental curve that matches the conditions imposed by the theoretical model describing the technique, the relative high volume of sample required, the complexity of the electronic apparatuses involved and the delicacy of the thin wire that limited the commercial development of hot wire instruments [114].

LIT with laser spot heating has proven to be an efficient non-contact method to measure thermal transport properties of solids, which to the best of our knowledge has not been used for thermal characterization of gases and liquids. Therefore, the method proposed here is innovative in the measurement of this thermal parameter in fluids using LIT, which also has as its main advantage over THW the small amount of sample that is required for a measurement, around $10^{-2}cm^3$.

Here, the theoretical and experimental details behind this method are described, whose usefulness is demonstrated by measurements of the thermal conductivity of air, water and ethylene glycol, some of the most common fluids.

5.3 Infinite vertical interface between two different media

5.3.1 Theory

We consider two semi-infinite and opaque materials with an infinite vertical interface placed in plane y=0. Medium 1 is at $y < 0$ and medium 2 is at $y > 0$. The surface of medium 2 is illuminated by a laser beam of power $P(t) = \frac{1}{2}P_0[1 + \cos(\omega t)]$, modulated at a frequency f ($\omega = 2\pi f$). The center of the spot laser is located at a distance d from the interface (0, d, 0), as shown in Figure 5.1. Adiabatic conditions are assumed on the sample surface, heat losses to the surrounding air are neglected.

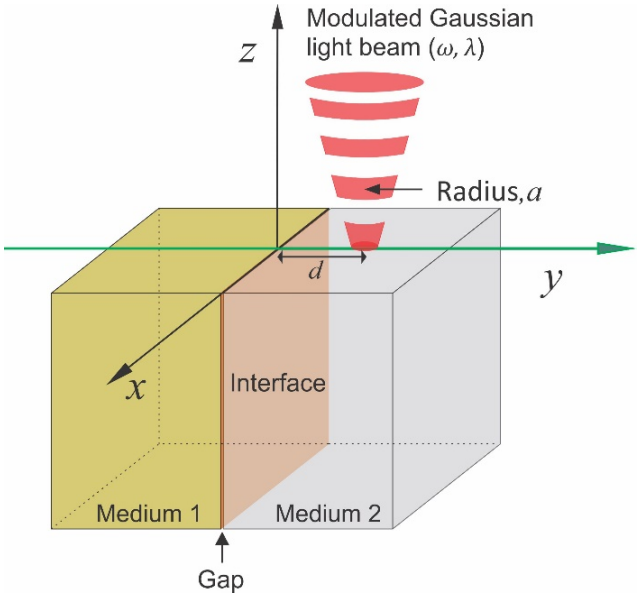

Figure 5.1 Schematic of an infinite vertical interface that divides two different media. Focused and modulated laser beam impinges in medium number 2.

We start the calculation considering that the infinite interface separates 2 infinite media. We consider a point-like heat source located in medium 2 at a distance d from the interfae. The expressions for the spherical thermal wave T generated by the excitation in medium 2 in the absence of an interface is given by [37]:

$$T(x,y,z) = \frac{P_o}{4\pi k_2}\frac{e^{-\sigma_2 R_c}}{R_c} = \frac{P_o}{4\pi k_2}\int_0^\infty \delta J_o(\delta r)\frac{e^{-\beta_2|y-d|}}{\beta_2}\, d\delta \quad (5.1)$$

And the thermal waves scattered at the interface in both media can be expressed as [37]:

$$T_-(x,y,z) = P_o \int_0^\infty \delta J_o(\delta r) A e^{\beta_1 y}\, d\delta; \qquad y < 0 \quad (5.2)$$

$$T_+(x,y,z) = P_o \int_0^\infty \delta J_o(\delta r) B e^{-\beta_2 y}\, d\delta; \qquad y > 0 \quad (5.3)$$

Where $\beta_j = \sqrt{\delta^2 + q_j^2}$, with subscript j = 1,2. Expression 5.1 represents a spherical wave in Hankel's space. The temperature of materials 1 and 2 for $y < 0$ and $y > 0$, is given by $T_1 = T_-$ and $T_2 = T + T_+$, respectively. To determine constants A and B in Equations 5.2 and 5.3, the conditions of continuity of flow and discontinuity of the temperature in the interface are considered:

$$-k_1 \frac{\partial T_1}{\partial y}\Big|_{y=0} = -k_2 \frac{\partial T_2}{\partial y}\Big|_{y=0} \quad (5.4)$$

$$(T_2 - T_1)_{y=0} = R_{th} k_2 \frac{\partial T_2}{\partial y}\Big|_{y=0} \quad (5.5)$$

By solving Equations 5.4 and 5.5 we obtain,

$$A = \frac{e^{-\beta_2 d}}{2\pi} \times \frac{1}{k_1\beta_1 + k_2\beta_2 + R_{th}k_1\beta_1 k_2\beta_2} \quad (5.6)$$

$$B = \frac{e^{-\beta_2 d}}{4\pi k_2\beta_2} \times \frac{-k_1\beta_1 + k_2\beta_2 + R_{th}k_1\beta_1 k_2\beta_2}{k_1\beta_1 + k_2\beta_2 + R_{th}k_1\beta_1 k_2\beta_2} \quad (5.7)$$

Accordingly, the temperature inside each material is given by

$$T_1(x,y,z) = \frac{P_o}{2\pi}\int_0^\infty \delta J_o(\delta r) e^{\beta_1 y} e^{-\beta_2 d} f_1(\delta)\, d\delta \quad (5.8)$$

$$T_2(x,y,z) = \frac{P_o}{4\pi k_2}\int_0^\infty \delta J_o(\delta r)\frac{e^{-\beta_2|y-d|}}{\beta_2}\, d\delta + \frac{P_o}{4\pi}\int_0^\infty \delta J_o(\delta r) e^{-\beta_2 y} e^{-\beta_2 d} f_2(\delta)\, d\delta \quad (5.8a)$$

where

$$f_1(\delta) = \frac{1}{k_1\beta_1 + k_2\beta_2 + R_{th}k_1\beta_1k_2\beta_2} \tag{5.9}$$

$$f_2(\delta) = \frac{1}{k_2\beta_2} \times \frac{-k_1\beta_1 + k_2\beta_2 + R_{th}k_1\beta_1k_2\beta_2}{k_1\beta_1 + k_2\beta_2 + R_{th}k_1\beta_1k_2\beta_2} \tag{5.10}$$

Now, we consider that a free surface is located at plane $z = 0$ and we assume adiabatic boundary conditions at the sample surface ($z = 0$). Under these hypothesis, we can apply the image method to account for the sample surface, that results in having a laser spot of double power. Finally, if we consider not an ideal point-like heat source but a real circular Gaussian spot of a maximum power P_o and radius a, then, the temperature inside the sample is the sum of the contribution of each point of the Gaussian spot weighted by its intensity.

$$T_1(x,y,z) = \frac{2P_o}{\pi^2a^2}\int_{-\infty}^{\infty}\int_{-\infty}^{\infty} dx_0dy_0e^{-\frac{2\left[x_0^2+(y_0-d)^2\right]}{a^2}}\int_0^{\infty}\delta J_o(\delta r_0)e^{\beta_1 y}e^{-\beta_2 y_0}f_1(\delta)\,d\delta \tag{5.11a}$$

$$T_2(x,y,z) = \frac{P_o}{2\pi k_2}\int_0^{\infty}\delta J_o(\delta r_1)\frac{e^{\beta_2 z}e^{-\frac{(\delta a)^2}{8}}}{\beta_2}d\delta +$$

$$+\frac{P_o}{\pi^2a^2}\int_{-\infty}^{\infty}\int_{-\infty}^{\infty} dx_0dy_0e^{-\frac{2\left[x_0^2+(y_0-d)^2\right]}{a^2}}\int_0^{\infty}\delta J_o(\delta r_0)e^{-\beta_2 y}e^{-\beta_2 y_0}f_2(\delta)\,d\delta \tag{5.11b}$$

where $r_o = \sqrt{(x-x_o)^2+z^2}$ and $r_1 = \sqrt{x^2+(y-d)^2}$. Equations 5.11 represent the temperature at any point of each material but its numerical evaluation is rather time consuming since a triple integral is concerned. By considering the surface temperature profile along the *y*-axis, i.e. perpendicular to the interface and crossing the center of the laser spot, the order of the integrals drops, drastically reducing the computing time.

$$T_1(0,y,0) = \frac{P_o}{\pi}\int_0^{\infty} e^{-\frac{(\delta a)^2}{16}}I_o\left[\frac{(\delta a)^2}{16}\right]e^{\left(\frac{a^2\beta_2^2}{8}-\beta_2 d+\beta_1 y\right)}f_1(\delta)\,\delta d\delta \tag{5.12a}$$

$$T_2(0,y,0) = \frac{P_o}{2\pi k_2}\int_0^{\infty}\delta J_o(\delta|y-d|)\frac{e^{-\frac{(\delta a)^2}{8}}}{\beta_2}d\delta +$$

$$+\frac{P_o}{2\pi}\int_0^{\infty} e^{-\frac{(\delta a)^2}{16}} I_o\left[\frac{(\delta a)^2}{16}\right] e^{\left(\frac{a^2\beta_2^2}{8}-\beta_2 d-\beta_2 y\right)} f_2(\delta)\delta d\delta \qquad (5.12b)$$

Here I_o is the modified Bessel function of order zero.

5.3.2 Simulations

The numerical simulations of Equation 5.12 are presented using two combinations of the mediums concerning their thermal properties. In the first one, the material of the medium 1 is a good thermal conductor, in relation to the material of medium 2 (intermediate thermal conductor). In second one, the material of the medium 1 is a bad thermal conductor, in relation to the material of medium 2. The properties of medium 2, k and α were selected according to a real sample of AISI-304. The properties of medium 1 were selected as those of Copper and Polyetheretherketone (PEEK), for better and worse conductors than medium 2, respectively. The simulation parameters are shown in Table 5.1. In all the simulations the illuminated material is material 2. The value of the power *Po* was chosen guaranteeing a maximum variation of temperature at the center of the spot of 15 K above the room temperature. Parameters *a*, *d*, and *f* were selected following the rule established by Pech-May in Reference [37], in which $2a \approx d \approx \mu/2$; $\mu = \sqrt{\alpha_2/\pi f}$.

Table 5.1. Values of the parameters used in the computer simulations.

Parameter	Material		
	Medium 2	**Medium 1**	
	AISI-304	**Cu**	**PEEK**
k ($Wm^{-1}K^{-1}$)	15 [115]	401[7]	0.259 [116]
α (m^2s^{-1})	4×10^{-6}[117]	117×10^{-6}[7]	0.18×10^{-6} [116]
P_0 (W)	200×10^{-3}	-	-
a (m)	150×10^{-6}		
d (m)	300×10^{-6}		
f (Hz)	3		
R_{th} (m^2KW)	$(0, 10^{-5}, 10^{-4}, 10^{-3})$		

According to Equation 1.13 and considering that the room temperature thermal conductivity of air is k_{air} = 0.025 $Wm^{-1}K^{-1}$, the R_{th} values presented in Table 5.1 correspond to air gaps widths of 0, 0.25, 2.5, and 25 μm.

Figure 5.2 shows the calculation of the natural logarithm of the temperature amplitude ln $|T|$ and the phase φ along the y axis for an AISI-304 sample in contact with PEEK material. The steel sample is illuminated by a Gaussian laser beam. Calculations have been performed using Equation 5.12 and the parameters mentioned in Table 5.1.

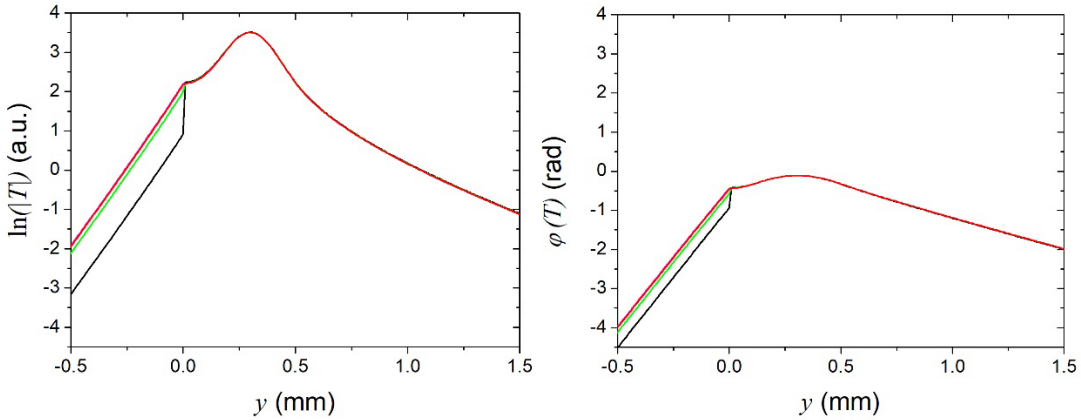

a) b)

Figure 5.2 Simulation curves of the natural logarithm of the a) temperature amplitude, ln($|T|$), and b) phase, $\varphi(T)$, along the y axis for an illuminated AISI-304 sample in contact with a PEEK sample. The effect of the thermal resistance R_{th} at the interface (y = 0) is shown. — R_{th}=0; — R_{th}=10^{-5}; — R_{th}=10^{-4}; — R_{th}=10^{-3} [m^2KW^{-1}].

In Figure 5.3, in the same way as Figure 5.2, the calculation of the natural logarithm of the temperature amplitude ln $|T|$ and the phase φ along the y axis for an AISI-304 sample in contact with Cu material is shown. It is worth noting that we are using the natural logarithm of the temperature instead of the temperature itself since the former accentuates the low temperature values (past the interface) with respect to the high temperature values (around the laser spot).

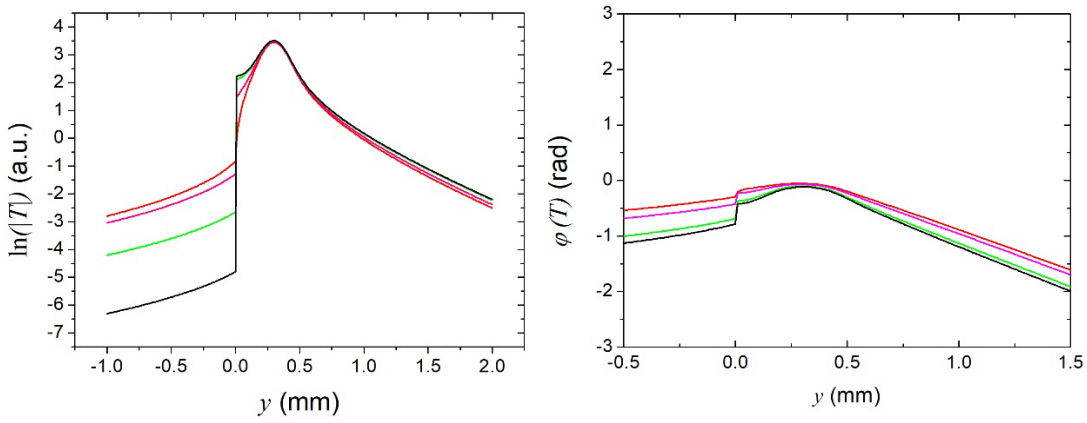

Figure 5.3 Simulation curves of the natural logarithm of the a) temperature amplitude, $ln(|T|)$, and b) phase, $\varphi(T)$, along the y axis for an illuminated AISI-304 sample in contact with a Cu sample. — R_{th}=0; — R_{th}=10^{-5}; — R_{th}=10^{-4}; — R_{th}=10^{-3} [m^2KW^{-1}].

As can be observed in Figures 5.2 and 5.3, the interface produces a singularity in both ln $|T|$ and φ even when there is a perfect thermal contact (R_{th} = 0). However, if there is a lack of adherence between the two media, an abrupt discontinuity appears. We have used the same scale level in ln $|T|$ and φ to clearly show that the jump at the interface is much higher for the former. Accordingly, in this manuscript only the amplitude of temperature will be treated in order to size the R_{th}. In this way, note that the height of the jump in ln $|T|$ increases with R_{th}.

The main difference between Figures 5.2 and 5.3 is that for a fixed value of the thermal resistance the jump in ln $|T|$ is higher if the material at the other side of the interface is a good thermal conductor than a bad thermal conductor. For instance, the thermal resistance of 10^{-5} m^2KW^{-1}, the pink lines in both figures, is barely distinguishable when material 1 is a worse thermal conductor than AISI-304, but produces a more distinguishable jump, around of 2.65 approximately if material 1 is a better thermal conductor than AISI-304. This result can be explained after analyzing Equations 5.9 and 5.10, in which the thermal resistance is correlated to k_1 and k_2 through the factor $R_{th}k_2k_1$. This means that for a fixed value of material 2, the higher the value of k_1, the lower the R_{th} value that can be detected.

5.3.2.1 Sensitivity to discontinuity

In order to quantify the height of the temperature jump or discontinuity at the interface position, expression 5.13 is used to measure the thermal contrast of this jump. Temperature logarithms are used to highlight the differences. Note that this contrast is independent of the laser power P_o.

$$\Delta = \ln\left(\left|T_{2\,(0,0,0)}\right|\right) - \ln\left(\left|T_{1\,(0,0,0)}\right|\right) \tag{5.13}$$

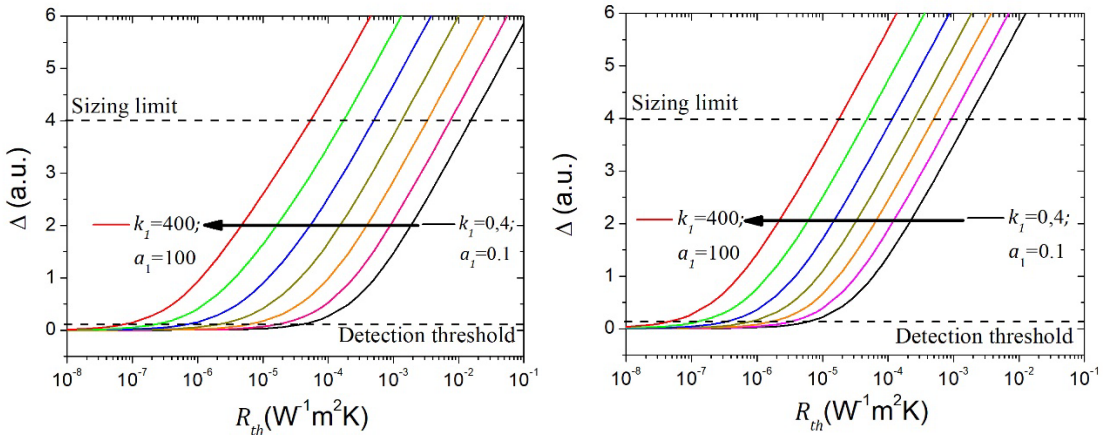

Figure 5.4 Simulation curves of the Δ as a function of R_{th}, varying the thermal properties of material 1 and keeping those of the material 2 fixed (AISI-304). The lower horizontal line indicates the threshold to detect the discontinuity at the interface and the upper one the limit to size the discontinuity. — k_1 = 0.4, α_1 = 0.1; — k_1 = 1.26, α_1=0.32; — k_1 = 4, α_1 = 1; — k_1 = 12.6, α_1 = 3.2; — k_1 = 40; α_1 = 10, — k_1 = 126; α_1 = 32, — k_1 = 400 [Wm^{-1}K^{-1}]; α_1 =100 [×10^{-6}m^{2}s^{-1}].

In Figure 5.4, simulations of the temperature contrast Δ as a function of the thermal contact resistance R_{th} are shown. Here, the thermal conductivity of material 1 varies from 0.4 (bad thermal conductors like polymers) to 400 Wm^{-1}K^{-1} (good thermal conductors like copper) in multiplying steps of $\sqrt{10}$. The corresponding thermal diffusivity also varies in steps of $\sqrt{10}$ from (0.1 to 100) ×10^{-6}m^{2}s^{-1}. k and α of material 2 were kept fixed to the AISI-304 values. In Figure 5.4a the parameters considered in

numerical calculations were taken from the Table 5.1. In Figure 5.4 it can be seen that low R_{th} is better detected (produce higher Δ) when the material 1 is a good thermal conductor than when it is an insulator or bad thermal conductor. For this reason, a thermal resistance of 10^{-5} m^2KW (equivalent to L = 0.25 μm) remains undetected when material 1 is a bad thermal conductor with k_1 = 0.1 $Wm^{-1}K^{-1}$ (Pink line in Figure 5.4a), but produces a thermal contrast as high as Δ = 2.17 for k_1 = 400 $Wm^{-1}K^{-1}$ (Red line in Figure 5.4a). On the other hand, note that for a given material 1 (a given color in Figure 5.4), there is a minimum R_{th} value below which the temperature contrast becomes negligible and therefore the discontinuity at the interface remains undetected. Taking into account the experimental noise, it was stablished a quite conservative detection threshold when the temperature contrast is Δ = 0.2 (see Figure 5.4). Finally, as R_{th} increases the temperature contrast rises monotonously, indicating that these air gaps are easily detectable. However, as high Δ means that the temperature in material 1 is very low, these wide air gaps cannot be sized precisely due to the experimental noise. Accordingly, we have stablished a sizing threshold Δ ≈ 4, which corresponds to a temperature in material 1 around 15 mK. Accordingly, for higher thermal contrasts the air gap is clearly identified but cannot be sized accurately. Figure 5.4b is a simulation in which the value of the modulation frequency was increased by two orders of magnitude, a fixed value of 100 Hz. In order to fulfill the relationship $2a \approx d \approx \mu/2$, which provides the best experimental conditions to size vertical cracks, the values of a and d were reduced one order of magnitude: a = 30 μm, d = 60 μm. As can be seen in the Figure 5.4b, the increase in frequency by two orders of magnitude, produces a displacement of the Δ to lower R_{th} values by almost one order of magnitude. This result means that high frequencies are better suited to detect and size extremely narrow discontinuities. It is important to mention that although focusing a laser to a radius of 30 μm and positioning its center at 60 μm from the interface between two media is simple, the spatial resolution of the current IR video cameras is not enough to work so close to the interface. For instance, the IR camera used in this work has a microscope lens reaching a resolution of 30 μm by pixel, which is enough to work at frequencies no greater than 10 Hz.

5.3.3 Results and discussion

In order to experimentally test the numerical simulation curves presented in Figures 5.2 and 5.3, a measurement system using LIT with focused laser beam has been implemented. Figure 5.5 is a schema representative of the experimental set-up. As excitation source, a continuous wave laser (532 nm) modulated in intensity by an Acousto-Optic Modulator (AOM) was used. The modulation frequency was f = 0.4 Hz. The laser beam is then focused onto the sample through a Germanium window and an optical arrangement. The laser power was adjusted to obtain a similar temperature rise at the center of the laser spot of about 5-10 K. The temperature field on the surface of the sample is recorded by an infrared camera (FLIR, SC7500) that uses a microscope lens to reach a spatial resolution of 30 μm (pixel size). A Lock-in module adapted to the camera allows processing thousands of thermograms, which are averaged giving amplitude and phase thermograms of the surface temperature with a low noise level. Averaging around 2×10^4 images at a frame rate of 350 images/s, the noise level of the data is kept below 1 mK. The sample is composed of two parallelepiped blocks of different material, 1 and 2. The surface of medium 2 is heated with a focused laser beam at a distance d from the interface on the sample´s x-y plane as shown in the inset.

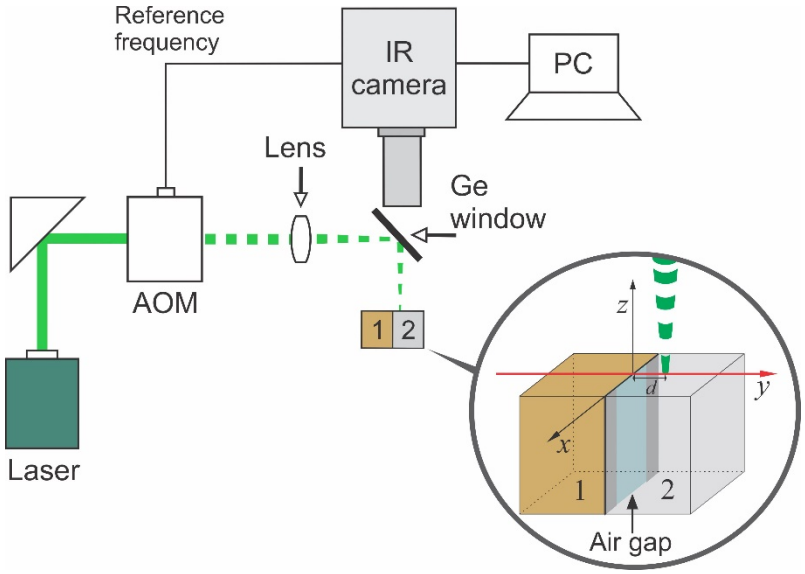

Figure 5.5 Schematic diagram for measurements of R_{th} in the interface using LIT with focused laser beam.

In practical measurements to verify the method, calibrated thermal resistances at the interface between two materials with different thermal properties were prepared. A parallelepiped block of AISI-304 stainless steel (dimensions 3x3x3cm) was put in contact under pressure with another parallelepiped piece of a different material. First, like in simulations, a bad thermal conductor, PEEK block (dimensions 3x3x0.6cm) and second, a good thermal conductor, Cu block (dimensions 3x3x3cm) were used. The surfaces in contact have mirror like finishing. In order to calibrate the air gap between the blocks, calibrated nickel tapes of micronic thickness were inserted between them as shown in Figure 5.6. In the two configurations (PEEK/AISI-304 and Cu/AISI-304) the steel piece was illuminated, as in the simulations. A thin graphite layer of a few microns thick was deposited onto the surface of the two materials in order to increase the absorption to the heating laser and to make the emissivity to infrared equal and homogenous in both materials.

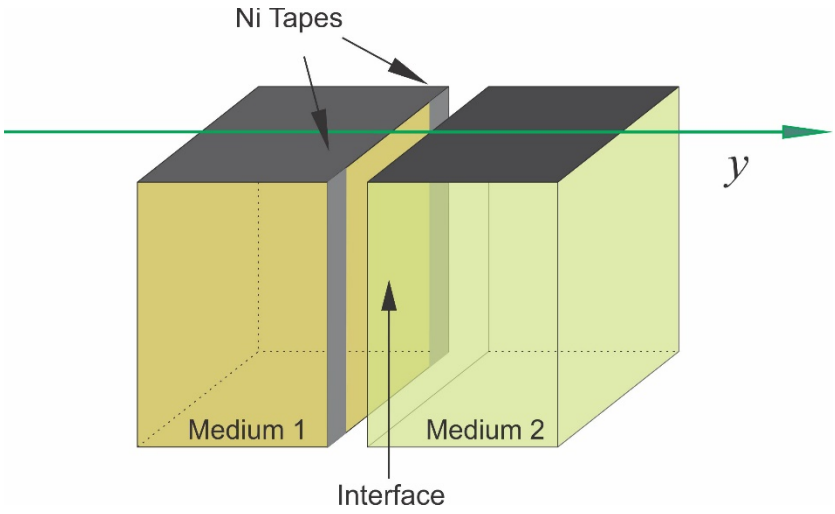

Figure 5.6 Schematic representation of an infinite interface of calibrated width.

PEEK/AISI-304 combination. All measurements in this combination have been performed under the same experimental parameters as shown in Table 5.2, which were selected according to in the conclusions of the numerical simulations.

Table 5.2. Values of the parameters used in the PEEK/AISI-304 combination.

Parameter	Value
P_0 (W)	$\approx 250 \times 10^{-3}$
a (m)	$\approx 200 \times 10^{-6}$

d (m)	$\approx 350 \times 10^{-6}$
f (Hz)	0.4

Using nickel tapes of calibrated thicknesses, different air gaps or interface widths were guaranteed as L=0, 2.5, 5, 10, 20, 30 and 40 µm. The amplitude thermogram shown in Figure 5.7a corresponds to the direct contact between the two blocks, L=0 µm.

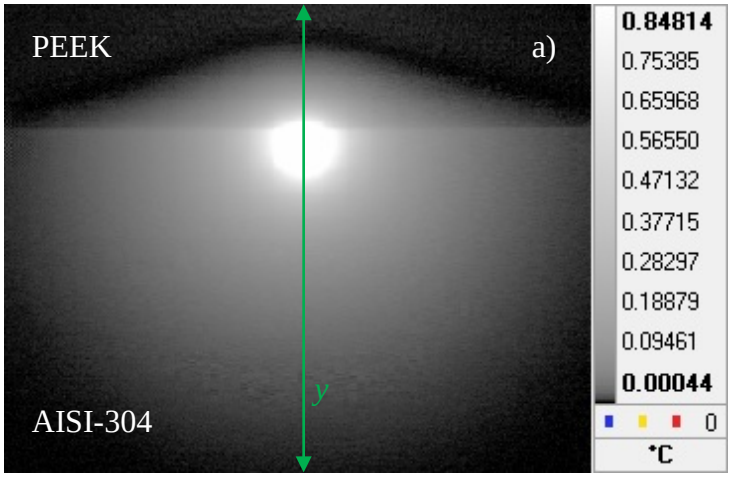

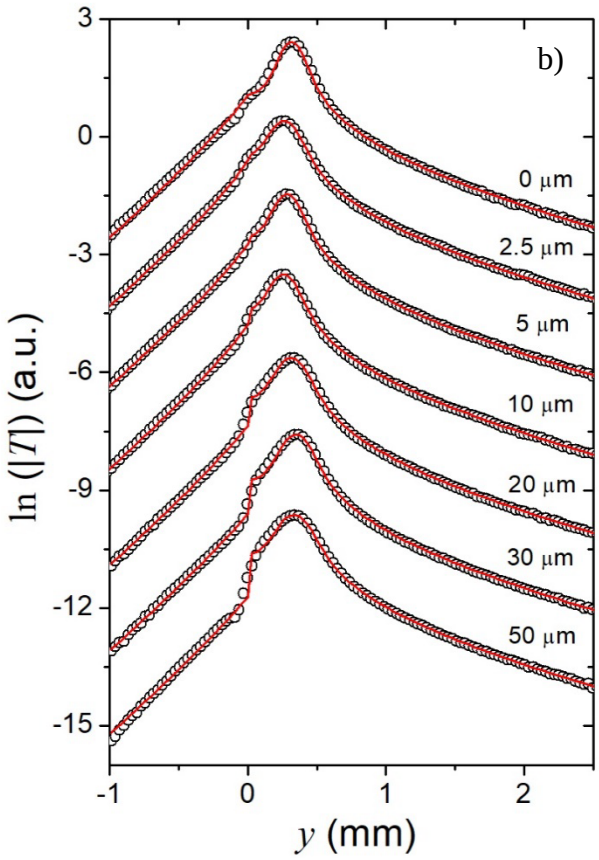

Figure 5.7 a) Amplitude thermogram at 0.4 Hz for an PEEK/AISI-304 combination at L=0 μm, and b) natural logarithm of the surface temperature amplitude along the y axis for seven interface widths.

As can be observed, there is a horizontal line at the boundary between the two materials. Unlike the case of infinite vertical cracks in the same material, where a clear line indicates a thermal discontinuity and therefore a thermal resistance [37], in the case of the junction between two different materials there is always a line indicating the transition from a material to the other one, due to the difference in their thermal properties. A comparison between the thermographs of L=0 μm and L=10 μm shows that it is visually difficult to perceive a difference between them. Accordingly, it is impossible to assess whether there is a perfect thermal contact or there is a thermal resistance between them. Then, to size the thermal resistances, the profiles of $\ln|T|$ along the y axis for all air gaps were analyzed, which are plotted in Figure 5.7b Dots are the experimental data that for each profile have been shifted to better appreciate the

jump at the interface. They exhibit a very low noise level due to lock-in averaging. Actually, at the longest distances shown in Figure 5.7b, y = -1 and 2.5 mm, the temperature is around 20 mK, but, as was said before, the noise level remains lower than 1 mK. The continuous lines are the least squares fits to Equation 5.12 using four free parameters: P_o, a, d and R_{th}. The retrieved thermal resistance values are R_{th} = $(2.3\pm2.9)\times10^{-5}$, $(1.10\pm0.17)\times10^{-4}$, $(1.64\pm0.15)\times10^{-4}$, $(3.3\pm0.2)\times10^{-4}$, $(8.4\pm0.3)\times10^{-4}$, $(1.14\pm0.05)\times10^{-3}$ and $(1.61\pm0.06)\times10^{-3}$ m^2KW^{-1}, which correspond to the following air gaps, L = 0.57±0.71, 2.8±0.4, 4.1±0.4, 8.5±0.4, 21±1, 29±1 and 41±2 μm respectively. They are in good agreement with the nominal values of the nickel tapes thicknesses, except for the case of direct contact between both blocks. Note that the uncertainty is around 5% for interface widths verifying $L \geq 10$ μm. However, as the width reduces the uncertainty increases (9%, 15% and 124% for L = 5, 2.5 and 0 μm, respectively). This is due to the reduction in the temperature contrast at the interface. In the case of direct contact (L = 0 μm), the fitting procedure is able to give a value of the thermal resistance, but the uncertainty is so high that the method cannot distinguish widths in the range 0-1 μm. This result is in agreement with the simulations given in Figure 5.2, where for temperature contrasts below 0.2 the thermal resistance cannot be detected. On the other hand, in all fittings the retrieved values of a and d are in the range d = 0.33-0.37 mm and a = 0.18-0.22 mm, which are very close to the values measured optically.

***Cu/AISI-304 combination*.** In this combination the experimental parameters used are shown in the next table,

Table 5.3 Values of the parameters used in Cu/AISI-304 combination.

Parameter	Value
P_0 (W)	$\approx250 \times 10^{-3}$
a (m)	$\approx150 \times 10^{-6}$
d (m)	$\approx300 \times 10^{-6}$
f (Hz)	0.2

In this case the nickel tapes of calibrated thicknesses, were L = 0, 1, 2.5, 5 and 10 μm. The amplitude thermogram shown in Figure 5.8a corresponds to the direct contact between the two blocks, L=0 μm.

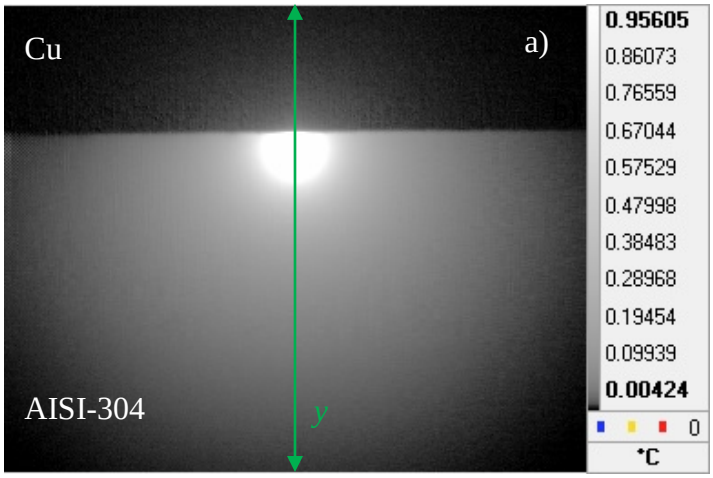
Cu
a)
AISI-304
y
0.95605
0.86073
0.76559
0.67044
0.57529
0.47998
0.38483
0.28968
0.19454
0.09939
0.00424
0
°C

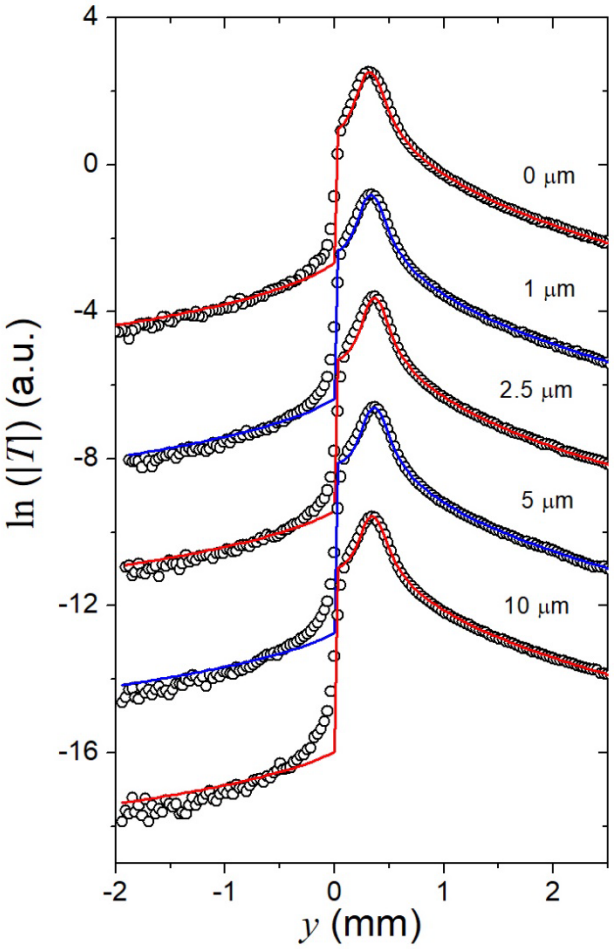
4
0
-4
-8
-12
-16
ln (|T|) (a.u.)
0 μm
1 μm
2.5 μm
5 μm
10 μm
-2
-1
0
1
2
y (mm)

Figure 5.8 a) Amplitude thermogram at 0.2 Hz for an Cu/AISI-304 combination at L=0 μm, and b) natural logarithm of the surface temperature amplitude along the y axis for five interface widths.

As before, there is a clear border indicating the change of the thermal properties between both materials, but looking at Figure 5.8a, it is not possible to evaluate whether the thermal contact is perfect. Figure 5.8b shows the temperature profiles along the y axis for five air gap widths: 0, 1, 2.5, 5 and 10 μm. Dots are the experimental data and the continuous lines are the least squares fits to Equation 5.12. Note that even for a tight contact between the two blocks (L = 0 μm) a net jump appears at the interface. This result confirms the prediction of section 5.3.2 that extremely narrow cracks are easily detected if the two materials are very good thermal conductors. The retrieved value of its thermal resistance is R_{th} = (4.3±0.4)×10^{-5} m^{2}KW^{-1}, which corresponds to an air gap of L = 1.1±0.1 μm. By fitting other perpendicular profiles on the same sample interface, widths in the range 0.7 to 1.2 μm were obtained in all cases. This is the closest interface that we can manufacture in cm-scale metallic samples. Simulations indicate that obtaining an almost perfect thermal contact in this combination using the same experimental parameters requires the interface width to be $L \leq 10$ nm (see red line in Figure 5.4a), which are not possible to machine. The fittings corresponding to the remaining samples give the following thermal resistances, R_{th} = (7.4±0.6)×10^{-5}, (9.1±0.7)×10^{-5}, (1.61±0.14)×10^{-4} and (2.4±0.3)×10^{-4} m^{2}KW^{-1}, which correspond to the following air gap widths, L = 1.86±0.16, 2.27±0.18, 4.0±0.4 and 6.1±0.6 μm respectively. In all fittings the retrieved values of a and d are in the range d = 0.27-0.33 mm and a = 0.13-0.17 mm, very close to the values measured optically. Although the retrieved values of the air gap width are good, they are worse than those obtained in the combination PEEK/AISI-304. The reason for that is associated to the temperature data in the copper region as given in Figure 5.8b. On the one hand, far away from the interface (-2 mm < y < -1 mm) the temperature level is around 10 mK for L = 0 and falls down to 3 mK for L = 10 μm. Therefore, they are noisier than in the case of PEEK. This is due to the huge jump at the interface position when material 1 is a good thermal conductor.

On the other hand, near the interface (-0.5 mm < y < 0 mm) the temperature does not exhibit the expected sharp discontinuity at the interface but a smooth transition involving around 15 pixels. This result is due to the imperfect imaging system of the IR camera (diffraction, multiple reflections or optical aberration). The so-called Point Spread Function (PSF) describes the response of an imaging system to a point source or point object, and depends on the lens quality [118]. This effect is more noticeable as the temperature difference at the interface increases. Actually, this effect is also present in the PEEK temperature data (see Figure 5.7b), but only involves 2 or 3 pixels. Accordingly, the effect of the PSF is negligible in the fittings in the PEEK/AISI-304 couple, but becomes significant in the Cu/AISI-304 ensemble. In this way, the retrieved values of the thermal resistance are less accurate as the jump at the interface increases. Both, the low temperature level together with the PSF are the reasons why we established a sizing limit in Figure 5.4, indicating it is not possible to get accurate R_{th} values when the temperature contrast verifies $\Delta > 4$. This is just what happens for $L \geq$ 5 µm in the combination Cu/AISI-304 for which the temperature contrast verifies $\Delta \approx$ 4.5-5, as can be seen in Figure 5.8b. This means that this method is not able to size air gaps thicker than 5 µm in this combination. Accordingly, the retrieved value for L=5 µm is still acceptable (L=4.0 µm), but becomes just an estimation for L=10 µm (L=6.0 µm).

5.4 Thermal conductivity of fluids that fill interface between two media

In the first part of this chapter it was demonstrated that it is possible to characterize the width of an infinite interface or crack between two media of different materials. The work was based on the one developed by Pech-May *et. al*, in which both media were of the same material. Therefore, in both works the relation $R_{th} = L/k$ was considered to obtain the widths of each calibration gap predefined by means of tapes (calibrated by manufacturer). Here the value of thermal conductivity used corresponded to the air (fluid filling the interface) and the values of R_{th} were obtained by adjusting the experimental curves to the expression 5.12, as already seen in section 5.3.3.

The simple relationship of thermal resistance to width

$$L = k_{fluid} * R_{th} \tag{5.14}$$

suggests a method for determining the thermal conductivity of a fluid that fills the interface by measurement of the slope of the (true) L Vs. (retrieved) R_{th} curve. This can be checked initially with the results obtained in section 5.3.3, in which a combination of PEEK/AISI-304 materials with different interface widths was measured. Figure 5.9 shows the nominal value of the air gap widths as a function of the retrieved thermal resistance for this system.

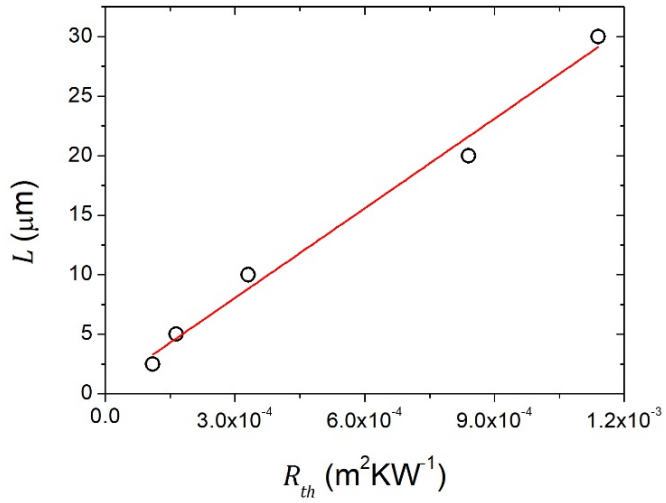

Figure 5.9 Nominal value of the air gap widths as a function of the retrieved thermal resistance for a PEEK/AISI-304 combination. The solid curve is the best linear least squares fit with a slope equal to k_{air}.

As can be seen from Equation 5.14, the slope of this curve is the air thermal conductivity, for which a value (0.0257 ± 0.0008) $Wm^{-1}K^{-1}$ was obtained, in agreement with the literature reported value, k_{air}=0.026 $Wm^{-1}K^{-1}$ [7]. The measurement uncertainty of about 3% is adequate for thermal conductivity measurements [119]. This result proves that the thermal conductivity of air can be measured using this methodology that could be used to characterize other samples that fill the interfacial cavity.

5.4.1 Numerical simulations and sensitivity analysis

Figure 5.10 shows simulation curves obtained using equation 5.12. These are calculations of the natural logarithm of the temperature amplitude ln $|T|$ along the y axis for an AISI-304/AISI-304 combination with two substances (air and water (k=0.6 $Wm^{-1}K^{-1}$ [44])) filling the interface gap. Water and air were selected as typical fluids used in THW calibration, and their thermal conductivity ratings are separated by an order of magnitude. Numerical calculations were performed for different widths of gap. Values of the parameters used in the simulations are shown in Table 5.4. A typical jump in the surface temperature profile is observed due to at the interface, which increases with the gap width. The temperature difference at the discontinuity, ΔT, is quantified in Figure 5.10 for the curves corresponding to the thinner and wider gaps. This temperature jump deserves a thorough analysis because it represents the signature of the thermal resistance that is obtained by the fitting procedure described above. Note that these values of ΔT are easily measurable by the thermographic camera (level noise around 1 mK) and that when the air gap widths vary from 5 to 70 μm there is a change in ΔT (I.e. $\Delta T_{(70\mu m)} - \Delta T_{(5\mu m)}$) of 3.3 K, a value that increases with the thermal conductivity of the substance filling the gap (reaching 9.43 K for water, as shown in Figure 5.10b). Note that, in the case of air, the drop is greater than that of water for a width of 5μm, which suggests a greater sensitivity to the width of the interface when it is very narrow. However, in both cases, the method is sufficiently sensitive over the entire range of proposed nominal widths, being able to easily recover the thermal resistance values corresponding to each gap width, as in Figure 5.9.

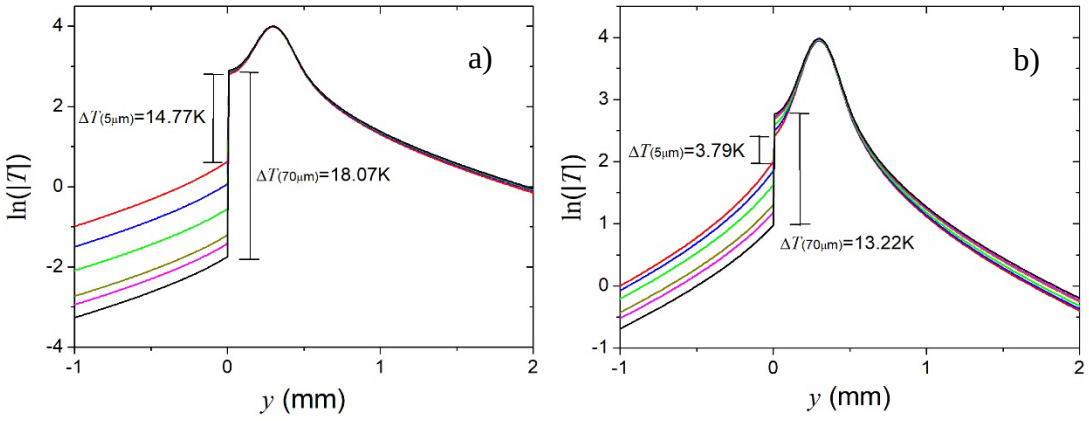

Figure 5.10 Simulation curves of the natural logarithm of the temperature amplitude, $\ln(|T|)$, along the y axis for an AISI-304/AISI-304 combination with a) air and b) water as the substance filling the gap, for different gap widths. — L=5; — L=10; — L=20; — L=40; — L=50 ; — L=70 [m^2KW^{-1}].

Table 5.4. Values of the parameters used in the numerical simulations. Different power values were chosen in each configuration to guarantee a maximum temperature on the surface of 318 K as a good practical case.

Parameter	**Material**		
	AISI-304	**PEEK**	**Al**
k ($Wm^{-1}K^{-1}$)	15 [115]	0.259 [116]	238 [7]
α (m^2s^{-1})	4×10^{-6} [117]	0.18×10^{-6} [116]	93×10^{-6} [7]
P_0 (W)	300×10^{-3}	6.8×10^{-3}	4.7
a (m)		150×10^{-6}	
d (m)		300×10^{-6}	
f (Hz)		0.5	
L (m)		$(5, 10, 20, 40, 50, 70) \times 10^{-6}$	

In order to evaluate the sensitivity of the discontinuity of the temperature to the thermal conductivity of the gap filling material, computer simulations of ΔT as a function of k are shown in Figure 5.11. Although Equations 5.12 provide the general expression of the temperature along the y-axis when the materials at both sides of the fluid are different, the methodology is simpler if the same material is used in both media (medium1 = medium 2 in Figure 5.6). Accordingly, in the following we set $\alpha_1 = \alpha_2$, and $k_1 = k_2 = k$ in Equation 5.12, and we analyze three material combinations of low,

intermediate and high conductivity: a) AISI-304/AISI-304, b) PEEK/PEEK, and c) Al/Al). Parameters used for simulations were shown in Table 5.4.

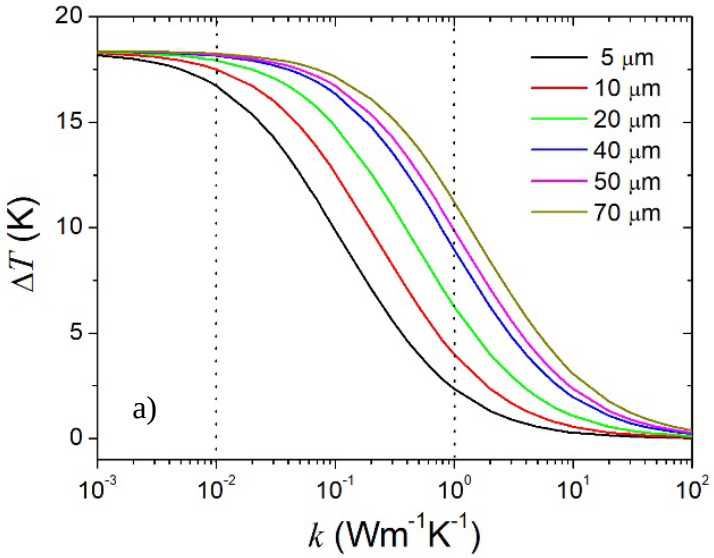

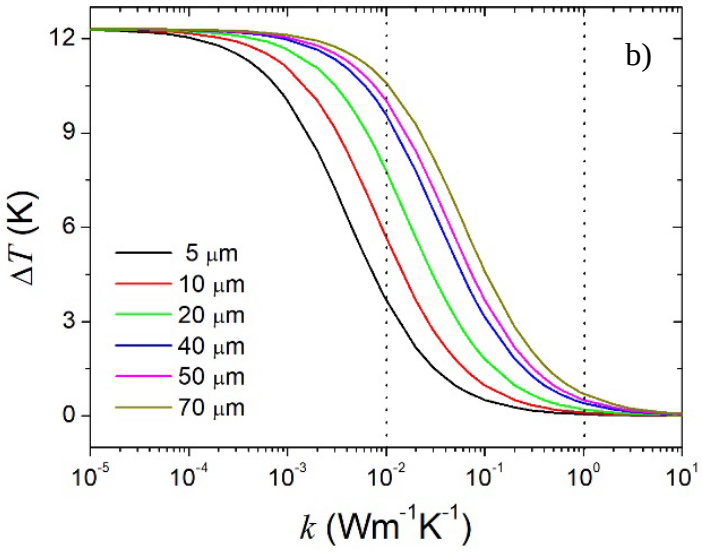

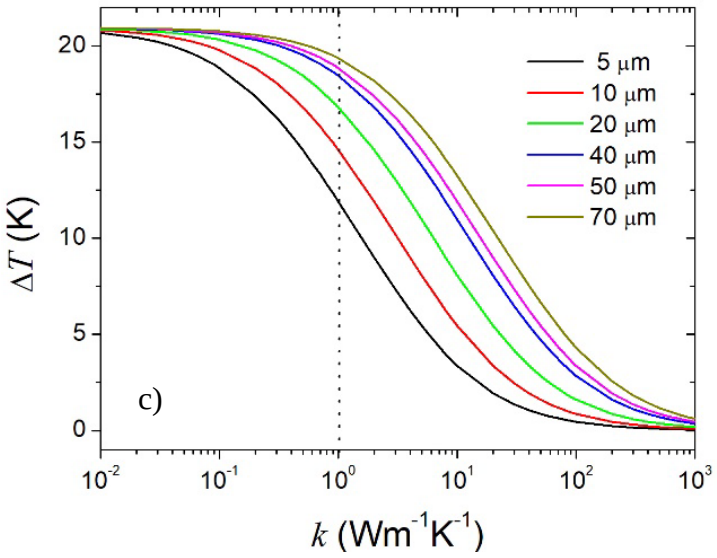

Figure 5.11 Simulation curves of ΔT versus k for experimental combinations of a) AISI-304/AISI-304, b) PEEK/PEEK and c) Al/Al. Dotted lines represent the limits of k values of interest in this work, from 1×10^{-2} to 1 $Wm^{-1}K^{-1}$, which includes the range of liquids and gases.

In Figure 5.11, the behavior of the curves at different widths are monotonous, but they move in the direction of increasing k when the width of the gap rises. This allows defining the most favorable measurement ranges of k in each configuration. Considering the range of interest, the AISI-304/AISI-304 combination presents the greatest variation of ΔT as a function of k in 5, 10, 20 and 30 μm, as shown in figure 4a. The PEEK/PEEK combination favors measurements of smaller k values between 1×10^{-1} to 1×10^{-3} $Wm^{-1}K^{-1}$. The Al/Al combination shows a wide variation range of ΔT as a function of k, showing clearly that this configuration is useful in the range from 1 to 100 $Wm^{-1}K^{-1}$. However, it is important to note that in practice it would not be advisable to use this last configuration due to the huge power that must be applied to medium 2 to obtain a good amplitude of the surface temperature field as was shown in the simulation parameters in Table 5.4.

5.4.2 Results and discussion.

As shown in Figure 5.9, the proposed method to determine the thermal conductivity of a fluid filling an interface between two media works if the materials on both sides of the interface are different. However, the implementation becomes much simpler using the same material for both regions. Therefore, considering the stiffness and final finish of the material, its thermal properties, and based on those obtained in the numerical simulation curves, the AISI-304/AISI-304 combination has been chosen for physical implementation. As the methodology has already been tested in Figure 5.9 with air, a universal and very low thermal conductivity gas, we have chosen as test materials a high thermal conductivity and universal liquid, water and ethylene glycol as an intermediate thermal conductivity liquid.

The experimental configuration consists basically of the set-up depicted in Figure 5.5, but the measurements were improved in order to achieve different widths of the interface. For this, it is proposed to generate an interface in the form of a wedge, in which the nominal values of the gap width along the *x*-axis are known. figure 5.12 shows the diagram of this configuration, which will allow continuous measurements as we move along the *x*-axis.

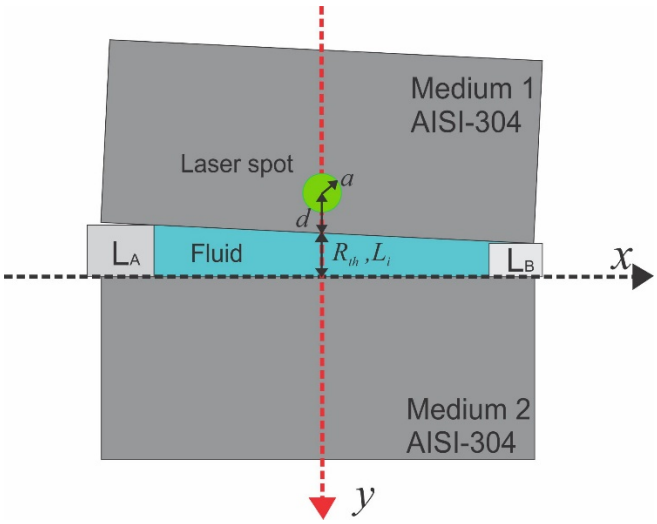

Figure 5.12 Schematic representation of an infinite interface with shape of a wedge. Showing the separating sheets (L_A and L_B) used to construct the gap between AISI-304/AISI-304 blocks.

A wedged gap in AISI-304/AISI-304 combination was obtained by sandwiching two AISI-304 sheets of different thicknesses (denoted in Figure 5.12 as L_A and L_B), between the blocks, close to the ends. A moderate pressure was applied to the blocks to maintain the different parts together but taking care to avoid false contact. The laser (Verdi-v6, COHERENT, 532nm, power up to 6W) and camera (SC7000, FLIR) positions were fixed, while the sample was displaced using a micrometer stage along *x*-axis with a 2 mm step. Due to the wedged shape of the cavity, for each position of the sample the interface width at the location of the laser spot is different. The temperature amplitudes along the transverse *y*-profile crossing the interface through the center of the laser spot were recorded for different widths L_i of the gap. Note that the wedged shape of the cavity does not affect the measured thermal resistance, as the only temperature data used to quantify the thermal resistance is the profile that crosses the center of the laser spot. Typical values of laser power, frequency, radius and distance to the interface were P_o = 200 mW, f=0.3 Hz, a = 170 µm and d = 390 µm, respectively. A layer of graphite was deposited on the surface of the sample (*x*-*y* plane) to enhance and homogenize the infrared emissivity over the entire surface, besides of increasing the absorption of the excitation beam.

Figure 5.13a shows the amplitude thermograms for a sample of water filling the interface with L_a = 75 µm and L_b = 10 µm, when the laser excites the surface at a position where the water width is L = 60 µm. The natural logarithm of the surface temperature amplitude along the *y*-axis for different widths is shown in Figure 5.13b.

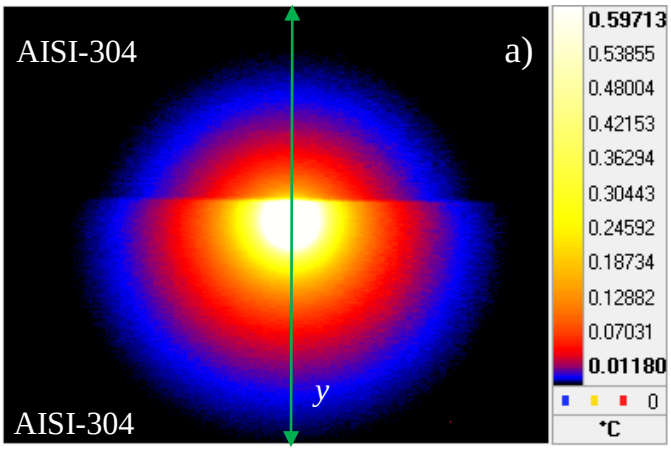

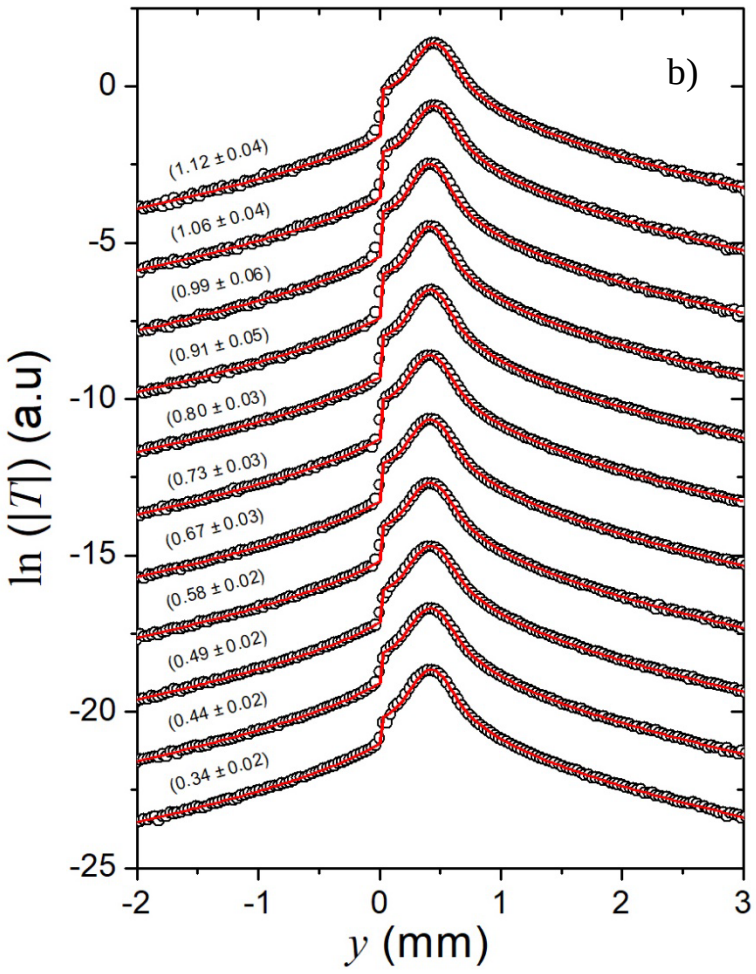

Figure 5.13 a) Amplitude thermogram at the surface for an AISI-304/AISI-304 combination whose interface is full of water and the laser is centered on the *y*-axis that crosses the interface at L=60 μm, and b) natural logarithm of the surface temperature amplitude along the *y*-axis for eleven interface widths. The inserted values are the thermal resistances ($\times 10^{-4} m^2 KW^{-1}$) retrieved from the fit to Equation 5.12.

The graphs in Figure 5.13b were shifted along the ordinate axis to better appreciate the jumps at the interface, which is placed at y = 0. In all cases the modulation frequency was at 0.3 Hz. The circles are experimental recorded data and the solid curves the best fits using equation 5.12, from which R_{th} was obtained as fitting parameter of particular interest. The parameters d, a, and P_o are of less interest, however the retrieved values allowed to verify the quality and consistency of the fitting as they were in excellent agreement with the preset experimental conditions. Similar results are shown in Figure

5.14 for ethylene-glycol (L_A = 50 μm and L_B = 20 μm). The amplitude thermogram at the surface was recorded at L = 35 μm. The curves shown in b) were taken at f = 0.3 Hz.

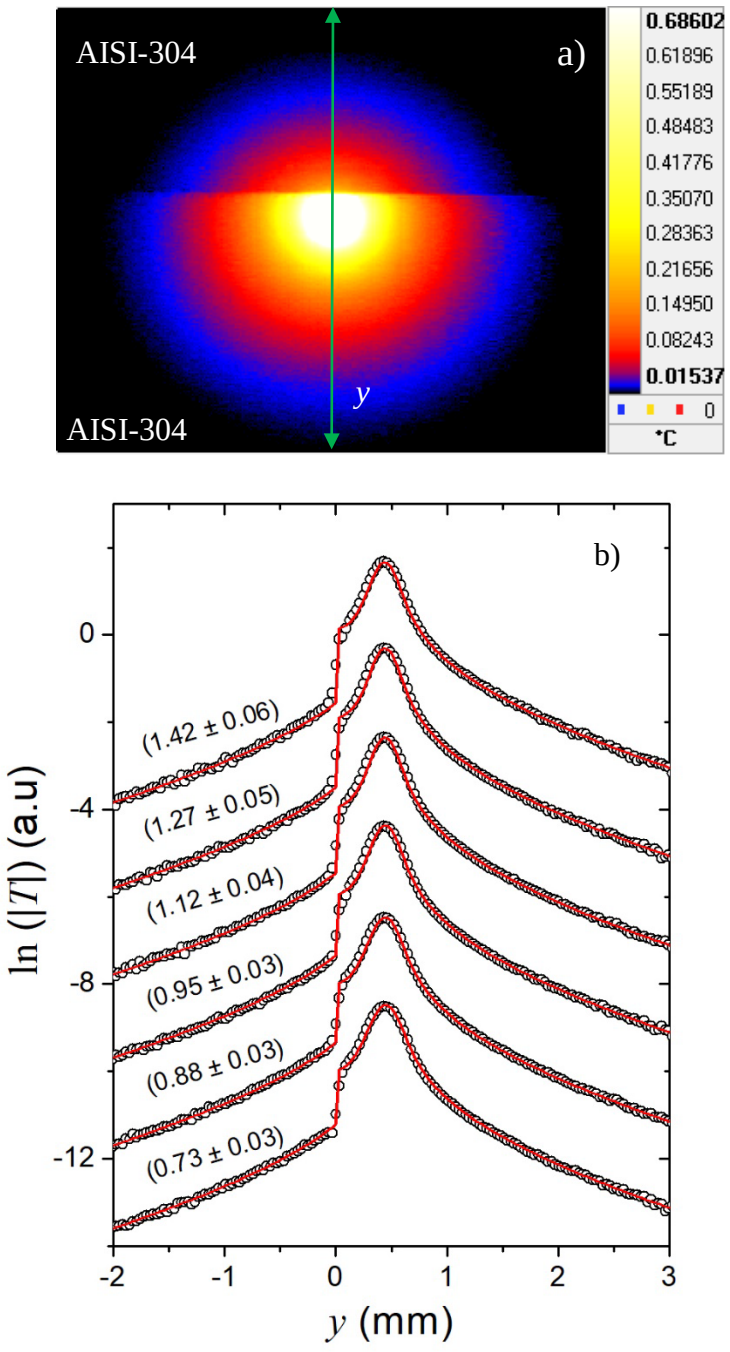

Figure 5.14 a) Amplitude thermogram at the surface for an AISI-304/AISI-304 combination whose interface is full of ethylene-glycol and the laser is centered on the

y-axis that crosses the interface at L=35 μm, and b) natural logarithm of the surface temperature amplitude along the *y*-axis for six interface widths. The inserted values are the thermal resistances ($\times 10^{-4} m^2 K W^{-1}$) retrieved from the fit to Equation 5.12.

Figure 5.15 shows the linear behavior predicted by equation 5.14 when L as a function of the retrieved thermal resistance R_{th} is plotted. Figure 5.15a is the experiment done with water and (b) with ethylene-glycol. The solid curves are the best least squares linear fits of the data from which k_{fluid} was obtained as the slope value. The obtained values were k_{water} = (0.618±0.003) $Wm^{-1}K^{-1}$ and $k_{ethylene\text{-}glycol}$ = (0.27±0.01) $Wm^{-1}K^{-1}$, which are in good agreement with literature reported ones (k_{water} = 0.6 $Wm^{-1}K^{-1}$, and $k_{ethylene\text{-}glycol}$ = 0.26 $Wm^{-1}K^{-1}$ [7,44,120]). As we can see the measurement uncertainty obtained with this improved configuration resulted in 1% and 4.6 % for the water and ethylene-glycol thermal conductivity respectively, showing the accuracy of the proposed method.

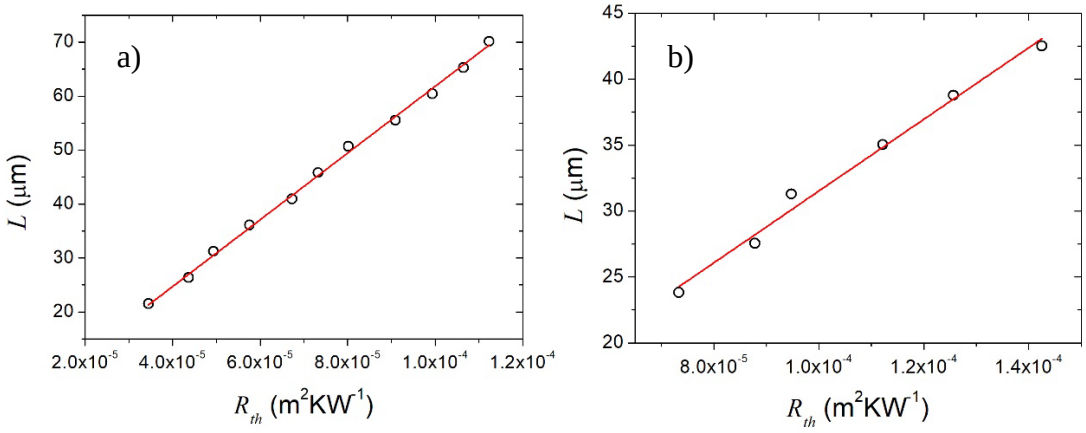

Figure 5.15 L Vs. R_{th} for an interface full of a) water and b) ethylene-glycol. The solid curves are the results of the best linear least squares fits.

5.5 Conclusions

The first part of this chapter addressed the issue of sizing the vertical interface between two different media using lock-in thermography with laser spot heating. An analytical expression for the surface temperature of the two-media when a modulated and focused laser beam impacts near the interface was proposed. The interface between the two media produces a singularity in the temperature field, just at the interface position,

due to the difference in their thermal properties. Besides, if the thermal contact between the two materials is not perfect, an abrupt discontinuity in the temperature at the interface is added. The validity of the model has been tested experimentally by performing lock-in thermography measurements on PEEK/AISI-304 and Cu/AISI-304 materials combinations with calibrated interface widths. By fitting the temperature amplitude profiles across the interface to the model, the air gap width at the interface was obtained. The good agreement between the optically calibrated width and the retrieved one confirms the validity of the method. The results indicate that it is easier to detect narrow interfaces in good thermal conductors than in insulators. Due to the diffraction limit and the especial resolution of nowadays cameras, IR thermography is restricted to size interfaces widths down to tenths of micron ($R_{th} \approx 10^{-5}$ m^2KW^{-1}). Characterizing interface widths in the nanometer scale ($R_{th} \approx 10^{-8}$-10^{-9} m^2KW^{-1}), as is the case of grain boundaries in polycristaline samples or composite materials, requires a high modulation frequencies (MHz) and a point-like laser spot. Modulated photothermal reflectance (MPR) is an ideal technique to reach the nanometer limit. It is worth mentioning that the method proposed in this manuscript is directly applicable to MPR.

On the other hand, a new methodology for thermal conductivity measurements in gases and liquids was proposed in the second part of this chapter. It uses lock-in infrared thermography with laser spot heating for straightforward measurement of the thermal conductivity of fluids that fill the interface between two solid materials. This is an accurate (measurement uncertainty can be as small as 0.5%), fast (measurement takes only some minutes) and non-contact method (both thermal excitation and detection involve electromagnetic waves) that requires very small quantity of sample (about $10^{-2}cm^3$), so that it offers significant advantages if compared to the conventional techniques for thermal characterization of fluids such as the well-established transient hot wire technique.

CHAPTER 6

THERMAL DIFFUSIVITY OF SOLIDS IN MOTION USING INFRARED THERMOGRAPHY

6.1 Particular objective.

To measure the in-plane thermal diffusivity of solid samples in motion at constant velocity using infrared thermography.

6.2 Introduction

The precise knowledge of the thermal diffusivity of materials is crucial in understanding dynamic processes in thermal engineering. During the last decades, many methods have been proposed to measure the thermal diffusivity of a wide variety of materials and shapes: bulk, thin films on substrate, free-standing films, filaments, etc [121]. In all these methods, the specimen under study remains at rest.

In this chapter it is proposed to use infrared thermography to measure the in-plane thermal diffusivity of samples that are moving at constant velocity. This proposal mimics the real case of in-line production or in-line quality control processes in factories, where heterogeneities, i.e. local changes in the properties, must be detected in real time, without stopping the production chain. Here, the experimental configuration consists in heating the sample surface by a focused laser beam while the surface temperature is recorded by an infrared camera. The method is based on analyzing the surface temperature field in natural logarithm scale. Then, three simple linear relations were found from which the thermal diffusivity can be obtained in a straightforward way, i.e. avoiding delicate multiparametric fittings.

First, analyzing the two orthogonal temperature profiles (transverse, y, and longitudinal, x, to the sample movement) that cross the centre of the laser spot, it is demonstrated that, for a thermally thick and a thermally thin sample, the natural logarithm of the temperature multiplied by the distance and the square root of the

distance from the laser spot, respectively, have a linear behavior as a function of this distance, *y* or *x*, with a different slope for each profile. These slopes are directly related to the thermal diffusivity transverse, α_y, and parallel, α_x, to the sample movement by simple formulas involving the sample velocity. The third linear relation is obtained from the analysis of the transverse profiles at a distance from the laser spot, where the $\ln(T)$ of each profile are parabolas and the inverse of the second order coefficient of these parabolas is a linear function of the distance to the laser spot, *x*, as it was demonstrated in static pulsed experiments [122]. From the slope of this straight line, the thermal diffusivity transverse to the sample movement, α_y, can be obtained by a simple relationship.

It is demonstrated that these methods are valid not only for opaque samples but also for semitransparent materials. Moreover, a significant benefit of the above mentioned linear relations is that they are not affected by heat losses by convection and radiation. To check the ability of the method, measurements on calibrated samples covering a wide range of thermal diffusivities (from insulators to good thermal conductors) were done. The results we have obtained confirm the validity of the methods to measure the thermal diffusivity accurately.

It is worth noting that these methods can be directly applied when the sample remains at rest and the laser spot scans the sample at constant velocity, a method known as Flying Spot infrared thermography proposed by Kubiak [123] and has been developed by several research groups to detect cracks in a fast manner [112,122,124,125].

6.3 Theory

Initially, the case in which the sample is at rest is considered. We deal with an anisotropic sample, illuminated by an extremely brief (Dirac) pulsed laser of energy Q_o and Gaussian profile of radius *a* (at $1/e^2$). The Cartesian reference frame coincides with the principal axes of this anisotropic slab. The heat losses by convection and radiation from the sample surface are considered. The surface temperature rise above the ambient is given by Equation 2.61 as was demonstrated in section 2.3.2, that is:

$$T(x,y,0,t) = \frac{2Q_0(1-R)}{\pi} A(t) \frac{e^{-\frac{2x^2}{a^2+8\alpha_x t}}}{\sqrt{a^2+8\alpha_x t}} \frac{e^{-\frac{2y^2}{a^2+8\alpha_y t}}}{\sqrt{a^2+8\alpha_y t}}$$

where $A(t)$ is a function that depends on the optical properties and thickness of the sample as,

(a) For an opaque and thick material: $A(t) = \frac{1}{e_z}\left[\frac{1}{\sqrt{\pi t}} - \frac{h}{e_z} e^{(h/e_z)^2 t} Erfc\left(\frac{h}{e_z}\sqrt{t}\right)\right]$

(b) For an opaque and thin material: $A(t) = \frac{1}{\rho c l_s} e^{-\frac{2ht}{\rho c l_s}}$

(c) For a semitransparent material $A(t) = \frac{1}{\rho c} \frac{\beta\gamma}{\beta+\gamma}$

Now we consider the same anisotropic sample moving to the right along the *x*-axis at constant velocity *v*, while a laser of power P_o and Gaussian profile of radius *a* (at $1/e^2$) remains at rest, as it is shown in Figure 6.1.

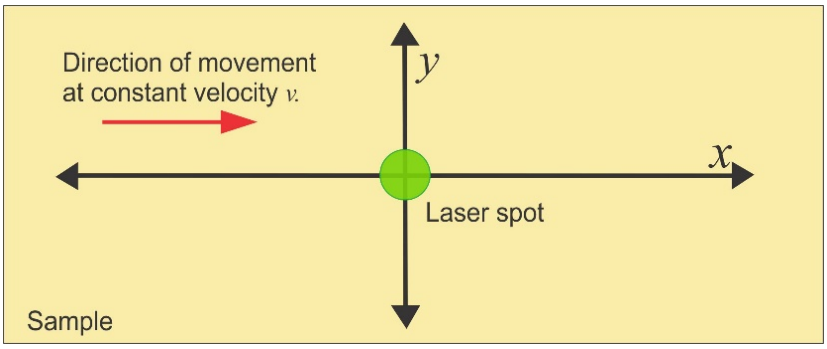

Figure 6.1 Front surface representation of a sample moving to the right at constant speed *v*, while the laser spot is at rest.

The laser is switched on at $t = 0$. The surface temperature at time t is given by the convolution integral of Equation 2.61 as,

$$T(x,y,0,t) = \frac{2Q_0(1-R)}{\pi} \int_0^t A(t-\tau) \frac{e^{-\frac{2[x-v(t-\tau)]^2}{a^2+8\alpha_x(t-\tau)}}}{\sqrt{a^2+8\alpha_x(t-\tau)}} \frac{e^{-\frac{2y^2}{a^2+8\alpha_y(t-\tau)}}}{\sqrt{a^2+8\alpha_y(t-\tau)}} d\tau \qquad (6.1)$$

6.3.1 Methods to measure the thermal diffusivity

Three methods to measure the thermal diffusivity of a sample that is moving at constant velocity are proposed by analyzing the surface temperature in logarithmic scale. The methods are valid once the steady-state has been stablished. Figure 6.2 shows the simulations, using Equation 6.1, of the time needed for the sample to reach the steady-state, t_c, as a function of the sample velocity. Calculations have been performed for four materials covering a wide range of thermal diffusivities, from thermal insulators (α = 0.1×10^{-6} m^{2}s^{-1}) to good thermal conductors (α = 100×10^{-6} m^{2}s^{-1}), using a = 0.1 mm and h = 0. As can be observed, this critical time decreases as the sample velocity rises and as the thermal diffusivity decreases. As these methods are addressed to study large surfaces in short times, we employ velocities $v \geq 2$ cms^{-1}. For these velocities, the steady-state is reached in a few seconds, even for the most conducting samples.

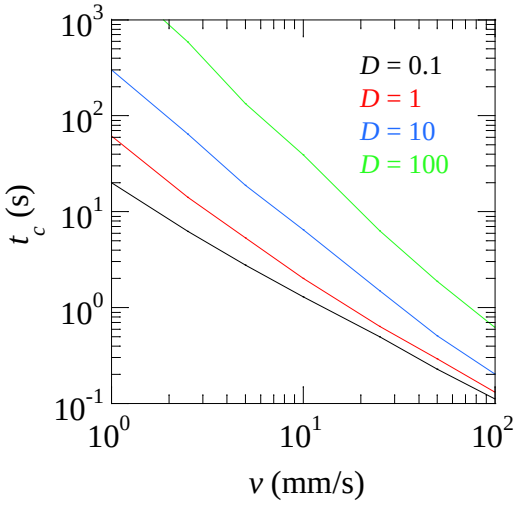

Figure 6.2 Simulations curves of t_c Vs. v in four materials of different thermal diffusivity. — α =0.1, — α =1, — α =10 and — α =100×10^{-6} m^{2}s^{-1}.

Now, simulations of the surface temperature field when the steady-state has been stablished are presented. In Figure 3a the isotherms of ln(T) for a sample (α_x = 4×10^{-6} m^{2}s^{-1}, α_y = 1×10^{-6} m^{2}s^{-1}, e_z = 3000 Ws$^{0.5}$m^{-2}K^{-1}) moving to the right at v = 2 cms^{-1} are presented. The sample is heated by a 0.1 W laser beam of radius a = 0.2 mm, which remains at rest. Simulations are performed for negligible heat losses (h = 0). In Figure 3b we show the transverse profiles of ln(T) at different longitudinal distances from the

laser spot. As can be observed, the central profile ($x = 0$) is almost linear, but the shape changes as x increases, in such a way that the transverse profiles become parabolas at long distances from the laser spot. Finally, in Figure 3c we show the central longitudinal profile ($y = 0$) of $\ln(T)$. Note the strong asymmetry of this profile in front of and behind the laser spot.

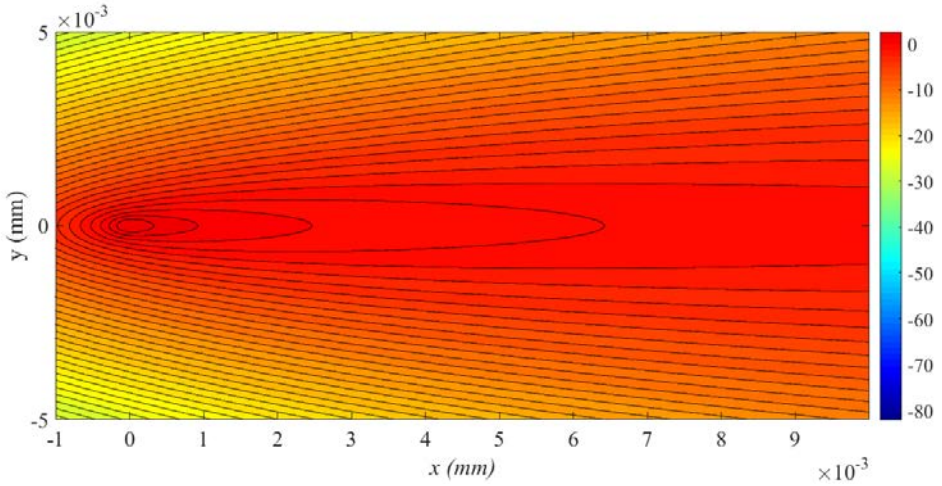

a)

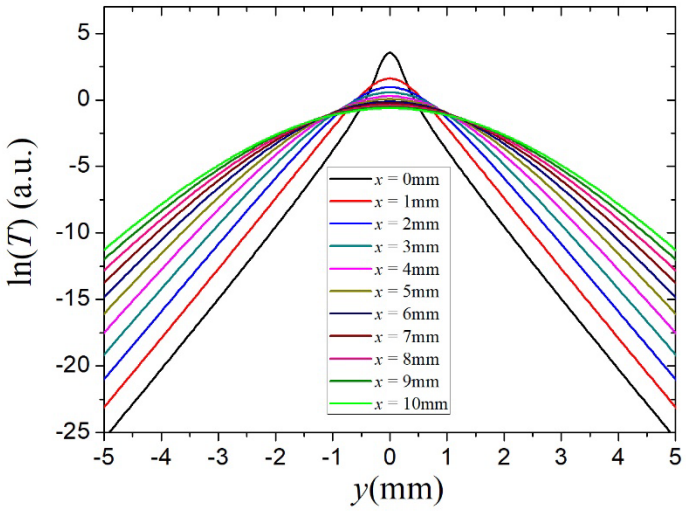

b)

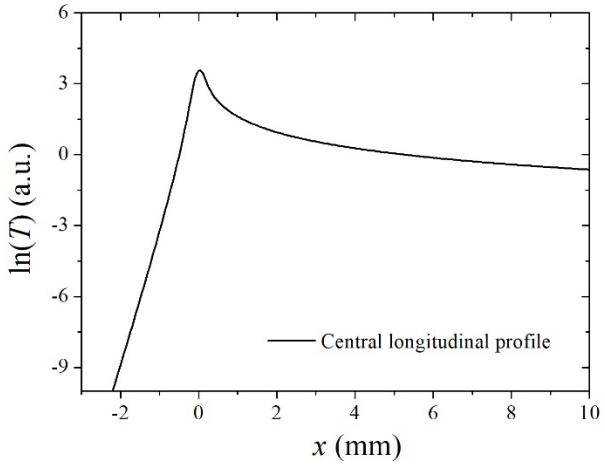

c)

Figure 6.3 a) Simulations curves of the contour plots of the natural logarithm of the surface temperature for a sample ($\alpha_x = 4\times10^{-6}$ m^{2}s^{-1}, $\alpha_y = 1\times10^{-6}$ m^{2}s^{-1}) heated by a 0.1W laser beam of radius a = 0.2 mm and h = 0, when the steady-state has been stablished. The sample is moving at v = 2 cm/s; **b**) Transverse profiles of ln(T) at several longitudinal distances, x, from the laser spot; **c**) Central longitudinal profile (y = 0) of ln(T).

In the following three methods to measure the thermal diffusivity that are based on the analysis of the shape of the central transverse profile, the central longitudinal profile and the transverse parabolas will be proposed. All of them lead to simple linear relations, which have the advantage of avoiding complex and delicate multiparametric fittings.

It is worth noting that the three methods are also valid in the experimental configuration where the sample remains at rest while the laser is moving at constant velocity along a straight line onto the sample surface. This is the so-called Flying Spot infrared thermography, which in recent years has raised the interest of the IR thermography community for quantitative characterization of large surfaces [122,124].

The central transverse profile method. The Figure 6.4a shows the simulations curves of the central (x = 0) transverse profile of the natural logarithm of the surface temperature using the Equation 6.1 for the same sample as in Figure 6.3, with a = 0 and in the absence of heat losses (h = 0). Two cases are considered. (a) If the material

is opaque and thick, we have found that the natural logarithm of the temperature multiplied by the transverse distance, $\ln(Ty)$, behaves linearly as a function of the transverse distance, *y*. (b) If the material is an opaque and thin sample, or is transparent, the natural logarithm of the temperature multiplied by the square root of the transverse distance, $\ln(Ty^{0.5})$, is a linear function of the transverse distance. The origin of the difference lies in the fact that the expression of the surface temperature for opaque and thick samples shows an additional $1/\sqrt{t}$ factor with respect to both opaque and thin and transparent samples, as can be observed in Equations 2.62 an 2.63. The slope (*m*) of these straight lines is related to the sample velocity, the transverse α_y, and the longitudinal α_y, thermal diffusivity through the simple formula:

$$m = \pm \frac{v}{2\sqrt{\alpha_y \alpha_x}} \tag{6.2}$$

In order to check the influence of heat losses on the central transverse profile, we have performed simulations for realistic values of the heat losses coefficient at room temperature. The results show that this profile remains unaffected by heat losses for values of *h* coefficient as high as 100 $Wm^{-2}K^{-1}$. We have also analyzed the effect of the laser spot radius on the linear behavior of the central transverse profiles. In Figure 4b we show simulations performed for the same thermally thick material as in Figure 4a. As can be observed, far away from the laser spot the linearity is kept with the same slope given by Equation 6.2. This conclusion is also valid for opaque and thin or transparent samples. Accordingly, the thermal diffusivity along the transverse direction with respect to the sample movement can be obtained in a simple manner using Equation 6.2.

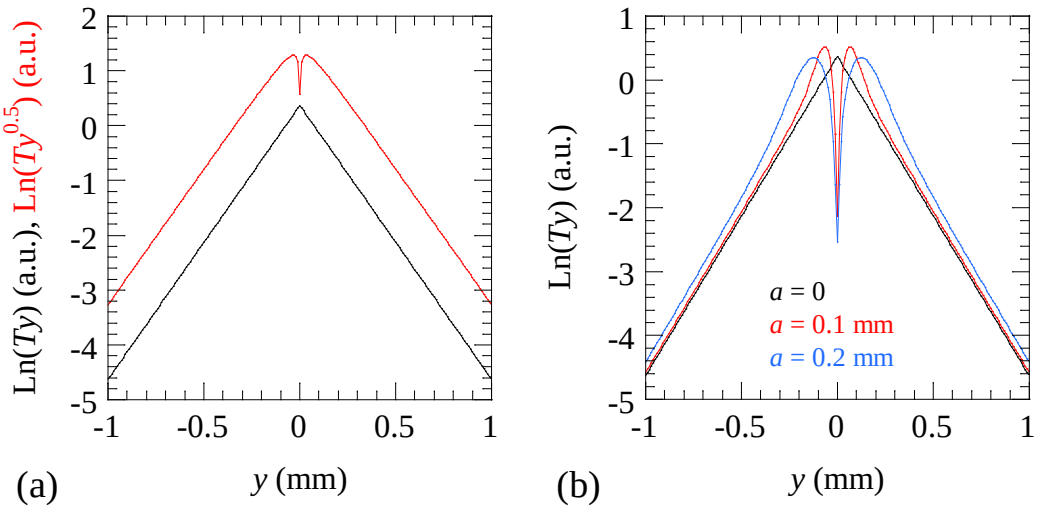

Figure 6.4 a) Simulations curves of the central transverse profile of $ln(Ty)$ for an opaque and thick sample (black curve) and $ln(Ty^{0.5})$ for an opaque and thin sample or a transparent sample (red curve). Simulations have been performed for the same sample as in Figure 6.3 with a = 0 and h = 0; **b**) Effect of the laser spot radius on the central transverse profile for opaque and thick samples.

On the other hand, the linear behavior shown in Figure 6.4a allows to define the thermal diffusion lengths (μ) along the transverse directions with respect to the laser movement as the distance with respect to the laser spot for which $\ln(Ty)$ decreases by a factor e. This transverse thermal diffusion length is given by $\mu_i = 2\alpha_i/v$ with $i = y$ and z. In particular, μ_z defines the depth penetration of the transient thermal energy in experiments with a moving sample. Accordingly, a sample behaves as thermally thick if its thickness $L > 2\mu_z$, while it behaves as thermally thin if $L < 0.5\mu_z$.

The central longitudinal profile method. Figure 6.5a shows the simulation curves of the central (y = 0) longitudinal profile of the natural logarithm of the surface temperature using Equation 6.1 for the same sample as in Figure 6.3, with a = 0 and h = 0. Unlike in the transverse profile there is no symmetry with respect to the laser position. For $x > 0$, the curve is flat and lacks information on the sample thermal diffusivity. For $x < 0$, there is a linear relation depending on the sample velocity and thermal diffusivity. As before, two cases are considered. a) If the material is opaque

and thick we have found that the natural logarithm of the temperature multiplied by the longitudinal distance, $\ln(Tx)$, behaves linearly as a function of the longitudinal distance, x. b) If the material is an opaque and thin sample, or is transparent, we have found that the natural logarithm of the temperature multiplied by the square root of the longitudinal distance, $\ln(Tx^{0.5})$, is a linear function of the longitudinal distance. The slope (m) of these straight lines is related to the sample velocity and longitudinal thermal diffusivity, x, through the simple formula:

$$m = \frac{v}{\alpha_x} \tag{6.3}$$

Simulations performed for heat losses coefficients up to h = 100 $Wm^{-2}K^{-1}$ do not reveal any change in the slope of the straight line, indicating that this method is not affected by heat losses. Moreover, the slope of the straight line is neither modified when considering a realistic non-zero laser spot radius (see Figure 5b). These evidences indicate that Equation 6.3 provides a simple and robust method to retrieve the thermal diffusivity along the sample movement direction.

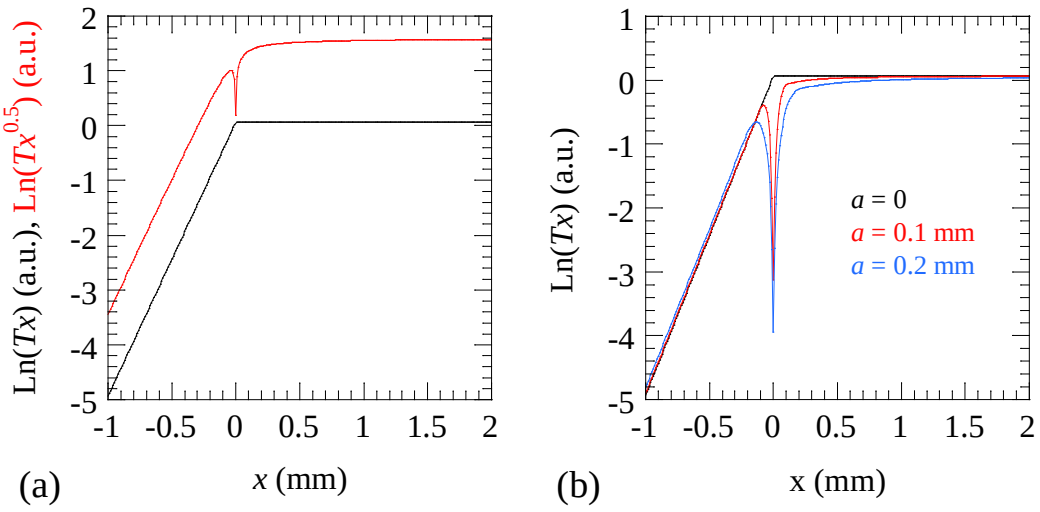

Figure 6.5 a) Simulations curves of the central longitudinal profile of $ln(Tx)$ for an opaque and thick sample (black curve) and $ln(Tx^{0.5})$ for an opaque and thin sample or a transparent sample (red curve). Simulations have been performed for the same sample as in Figure 6.3 with a = 0 and h = 0. **b**) Effect of the laser spot radius on the central longitudinal profile.

The linear behavior shown in Figure 6.5a allows us to define the thermal diffusion length along the longitudinal direction as the distance with respect to the laser spot for which $\ln(Tx)$ decreases by a factor *e*. This longitudinal thermal diffusion length is given by $\mu_x = \alpha_x/v$. Note that the depth penetration of heat in experiments with a moving sample is different in the longitudinal and transverse directions, even for isotropic samples.

The parabolas method. The Equation 2.61 gives the temperature field when the sample is heated by a brief laser pulse of Gaussian profile. According to these equations, the temperature along the *x* and *y* axes features Gaussian profiles for all times after the laser pulse and therefore the natural logarithm of the temperature profiles along the principal axes are parabolas

$$\ln\big(T(x,0,0,t)\big) = A(t) - C_x(t)x^2, \tag{6.4a}$$

$$\ln\big(T(0,y,0,t)\big) = A(t) - C_y(t)y^2, \tag{6.4b}$$

where the inverse of the second order coefficient of the parabolas is a linear function of time: $\frac{1}{C_{j(t)}} = \frac{a^2}{2} + 4\alpha_j t$ with *j* = *x* and *y*. The slope (m_j) of this linear relation gives the thermal diffusivity: $m_j = 4\alpha_j$. This method is neither affected by heat losses for *h* < 100 $Wm^{-2}K^{-1}$, and provides an efficient tool to measure the thermal diffusivity of isotropic and anisotropic solids [122]. As can be seen in Figure 6.3b, the transverse profiles of $\ln(T)$ become parabolas as we go away from the laser spot. Moreover, numerical simulations performed varying α_x, α_y, *a* and *v* show that the inverse of the second order coefficient of those parabolas verifies the same linear relation as in static flash measurements

$$\frac{1}{C_y} = \frac{a^2}{2} + 4\alpha_y t = \{x = vt\} = \frac{a^2}{2} + \frac{4\alpha_y}{v}x \tag{6.5}$$

This result indicates that the inverse of the second order coefficient of the parabolas is a linear function of the distance to the laser spot, whose slope verifies:

$$m = \frac{4\alpha_y}{v} \tag{6.6}$$

and the intercept is $a^2/2$. This linearity provides a versatile method to retrieve the transverse thermal diffusivity of a moving sample. It is worth noting that this result is valid for the three kind of materials analyzed in Equations 2.62, 2.63 and 2.64, regardless the laser power and the sample effusivity. Moreover, although heat losses reduce the temperature rise of the sample, the coefficient of the second order of the parabolas remains unaffected.

In order for the method to be applied properly we need to establish when the lateral profiles of $\ln(T)$ are parabolas satisfying Equation 6.4. In Figure 6.6 we show the comparison of the quasi-parabola obtained from Equation 6.1 and the exact parabola given by Equation 6.4. Simulations have been performed for the same sample as before ($\alpha_x = 4\times10^{-6}$ m^2s^{-1}, $\alpha_y = 1\times10^{-6}$ m^2s^{-1}, $e_z = 3000$ $Ws^{0.5}m^{-2}K^{-1}$), using the same experimental parameters (0.1 W laser beam with radius $a = 0.2$ mm, heat losses coefficient $h = 0$, velocity $v = 2$ cm/s and steady-state conditions). Two transverse profiles of $\ln(T)$ are shown: one for $x = 4$ mm and the other one for $x = 6$ mm. The continuous lines correspond to the simulation curves of Equation 6.1 and the dotted lines the simulations of Equation 6.4.

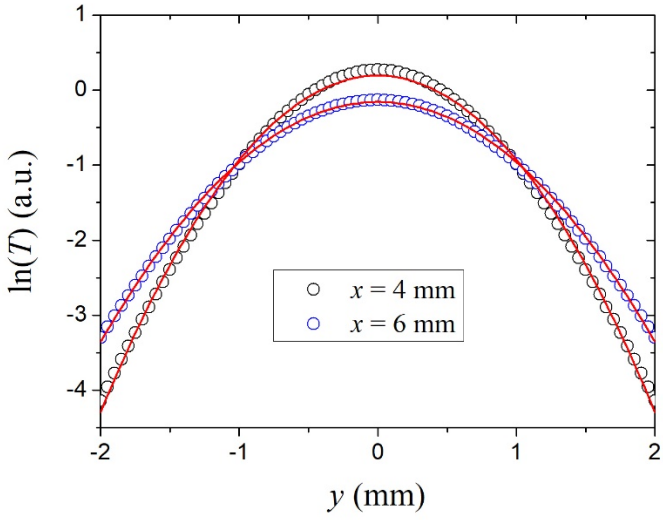

Figure 6.6 Simulations of the transverse profiles of $ln(T)$ for the same sample and experimental parameters as in Figure 6.3. Continuous lines correspond to the quasi-parabola given by Equation 6.1 and the dotted lines to the exact parabola given by Equation 6.4.

Now we want to determine the minimum distance from the laser spot, x_{min}, for which the difference between the quasi-parabola and the exact parabola is negligible. Systematic numerical simulations performed by varying α and v indicate that if the Péclet number, *Pe*, verifies

$$P_e = \frac{v x_{min}}{\alpha_x} \approx 20, \tag{6.7}$$

the difference is less than 0.05. To visualize the consequences of this result let us consider a fixed sample velocity of 2 cm/s and two materials of extreme thermal properties: a typical polymer (α = 0.1×10^{-6} m^{2}s^{-1}) and copper (α = 100×10^{-6} m^{2}s^{-1}). According to Equation 6.7, in the case of the polymer the minimum distance to the laser spot where the parabolas method can be applied is $x_{\min} \approx 0.1$ mm, whereas in the case of copper this limit rises up to $x_{\min} \approx 10$ cm. Consequently, when dealing with a good thermal conductor it is required to use a quite high sample velocity to keep $x_{\min}$ in the order of a few millimeters.

6.4 Results and discussion

An experimental scheme implemented for IR thermography measurements is shown in Figure 6.7, where the laser spot is kept fixed and the sample moves at constant velocity. A CW laser (532 nm, up to 6 W) is focused at the sample surface by means of a 10 cm focal length lens to a radius of about 200 μm. A Ge window, which reflects visible light and transmits IR wavelength, is used to prevent the scattered laser radiation from reaching the IR camera. A small mirror, glued to the Ge window, directs the laser beam onto the sample surface, perpendicularly. An IR camera (FLIR, model SC7500, 320 × 256 pixels, pitch 30 μm and spectral band from 3 to 5 μm) records the temperature field at the sample surface. An IR microscope lens is used to improve the spatial resolution of the IR camera to 30 μm, with a field of view of 9.60 mm x 7.68 mm. The sample is mounted on a dynamic system (cart + track) that is coupled to an electric engine to move the cart at constant speed in the range between 1.5 and 15 cm/s.

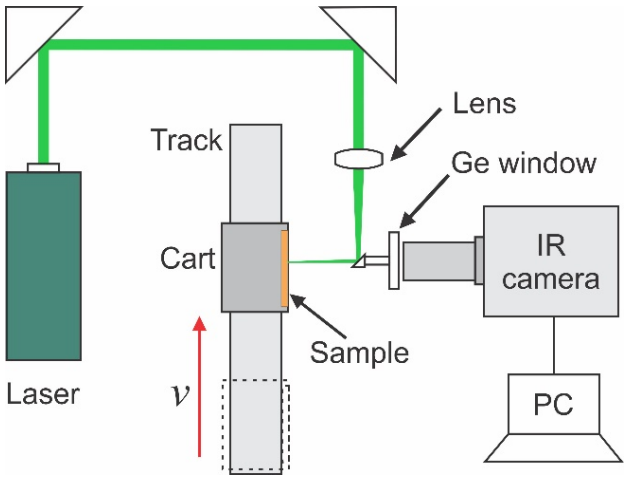

Figure 6.7 Schematic diagram for measurements with a moving sample and the laser spot at rest.

The speed of the sample is measured by counting the number of frames between the entrance and the exit of one end of the sample in the field of view of the camera and taking into account the length of the sample and the frame rate of the camera. In this way, the sample speed is measured with an uncertainty of less than 0.5%. We worked at the maximum frame rate allowed by the IR camera: 330 frames/s at full frame and up to 2000 frames/s applying a subwindowing (320 × 70 pixels). On the other hand, in order to enhance the signal to noise ratio, several hundred of thermograms are averaged after reaching the steady-state. For a comparison, in Figure 6.8 it is shown on the left side a single thermogram and on the right side an average thermogram corresponding to a AISI-304 (a), PEEK (b), and NICKEL (c) samples moving along the horizontal axis. This remarkable noise reduction will allow us to retrieve the sample thermal diffusivity with high accuracy.

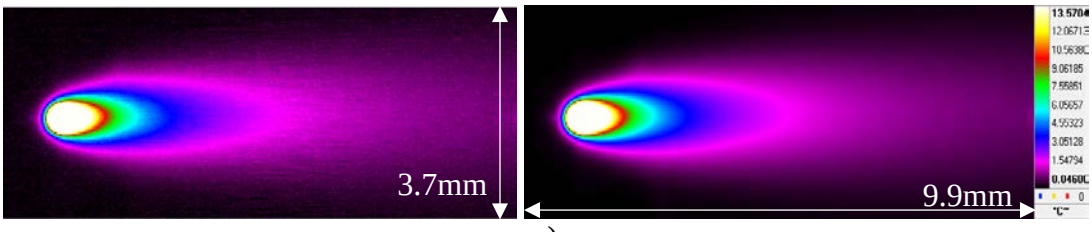

a)

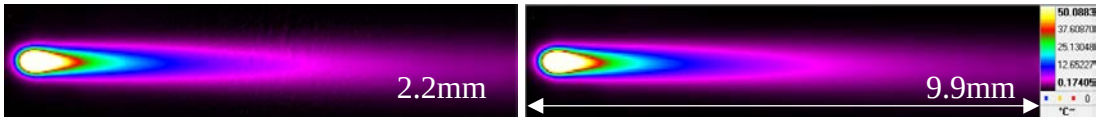

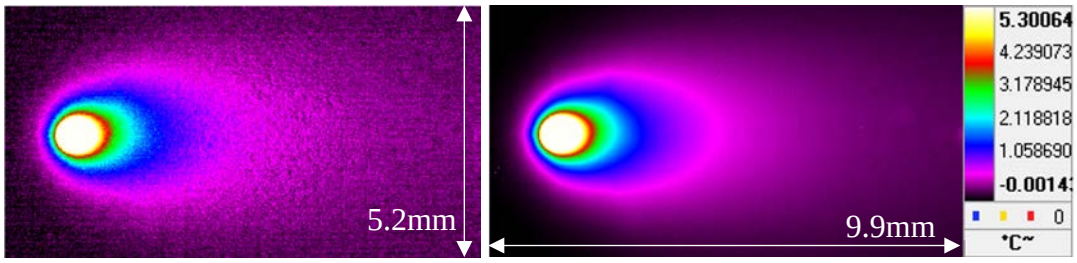

Figure 6.8 Single thermograms and averaged thermograms, respectively for an a) AISI-304, b) PEEK, and c) NICKEL samples moving to the right.

To verify the validity of the three methods proposed in this work we have tested them on some calibrated samples covering a wide range of thermal diffusivity values, from thermal insulators (polymers) to good thermal conductors (metals): Polyether-ether-ketone (PEEK), AISI-304, Ni, Zn and Al 2024-T6 alloy. We have also measured the anisotropic thermal diffusivity of balsa wood. All these materials have been covered by a thin graphite layer to enhance both the absorption to the laser and the IR emissivity. The method was also tested on two semitransparent samples: orange coloured Polymethyl-methacrylate (PMMA) and grey BK7 glass. Moreover, three thin samples have also been tested: 0.25 mm thick PEEK and 0.20 mm thick AISI-304 and Zn. Regarding the sample speed, for bad thermal conductors (polymers and glass) sample speeds in the lower range of our track, 1.5 - 2.5 cm/s, were used. Contrarily, for good thermal conductors higher speeds are better adapted: 6 cm/s for AISI-304 up to 15 cm/s for Al alloy. As a rule of thumb, we can say that the most appropriate speed for thermal diffusivity measurements produces a thermogram with an aspect ratio of the pseudo-ellipses around 3:1, similar to that found in Figure 6.8a.

Figure 6.9 shows the transverse profiles of $\ln(T)$ as a function of distance y corresponding to the three samples shown in Figure 6.8. For the sake of clarity, only eight transverse profiles, separated by 1 mm, are shown. Dots are the experimental data and the continuous lines are the parabolic fits. As can be observed, the experimental

profile at x = 1 mm, very close to the laser spot, differs from a parabola. Actually, according to Equation 6.7, the minimum distance from the laser spot to fulfil a parabola is $x_{min} \approx 1.3$ mm. This means that only transverse profiles at distances larger than 1.3 mm will be used in the parabolas method.

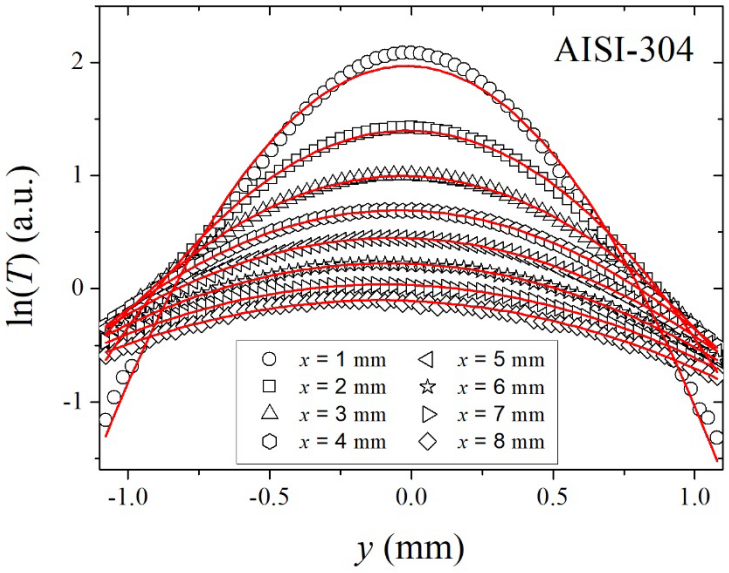

a)

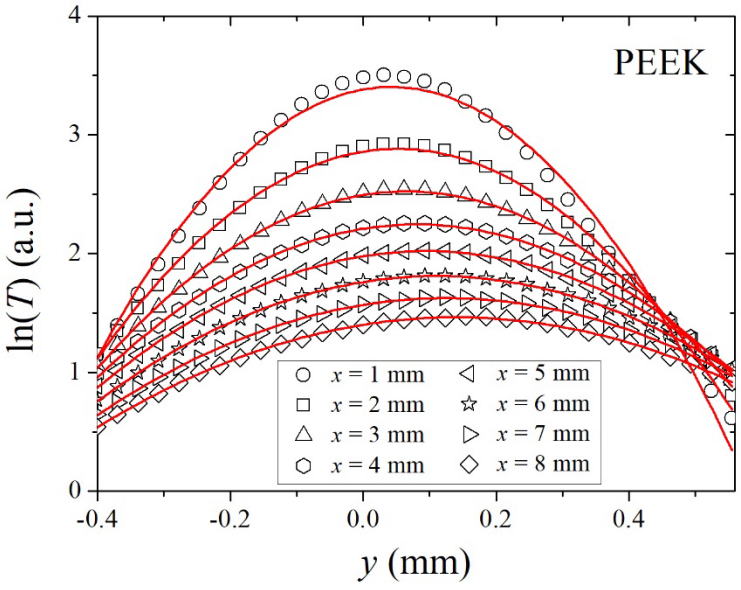

b)

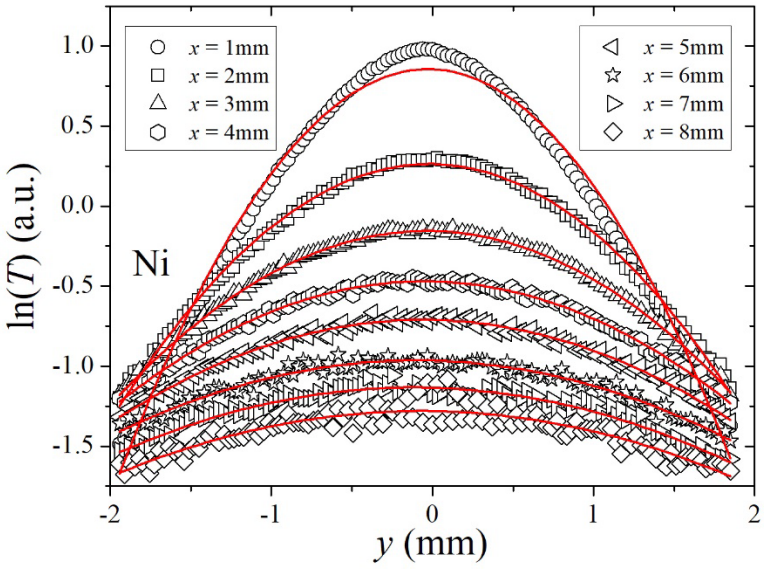

c)

Figure 6.9 Transverse profiles of $ln(T)$ at eight distances from the laser spot centre (x) for the a) AISI-304, b) PEEK, and c) NICKEL average thermograms shown in Figure 6.8. Dots are the experimental data and the continuous lines are the parabolic fits.

Figure 6.10 shows the inverse of the second order coefficient of the parabolas versus the longitudinal distance for some of the calibrated materials used in this work. Dots are the experimental data and the continuous lines are the linear fits. Figure 6.10a shows the results for thermal insulators, which are very clean and Figure 6.10b for good thermal conductors, for which the noise increases as the thermal diffusivity does. In fact, we were unable to measure the thermal diffusivity of a copper sample due to the poor signal to noise ratio. Then, using Equation 6.6 the thermal diffusivity is obtained. The results, summarized in Table 6.1, agree with the literature values and confirm the validity of the parabolas method. The uncertainty in the α values varies from less than 3% in thermal insulators up to 5-6% for good thermal conductors. It should be noted that, according to Equation 6.5, the intercept of the linear fits in Figure 6.10 gives the laser radius. Actually, for thermal insulators we obtain a laser radius in the range 0.2-0.3 mm, very close to the optically measured value. For good thermal conductors, instead, the sensitivity is not good enough to estimate the laser radius.

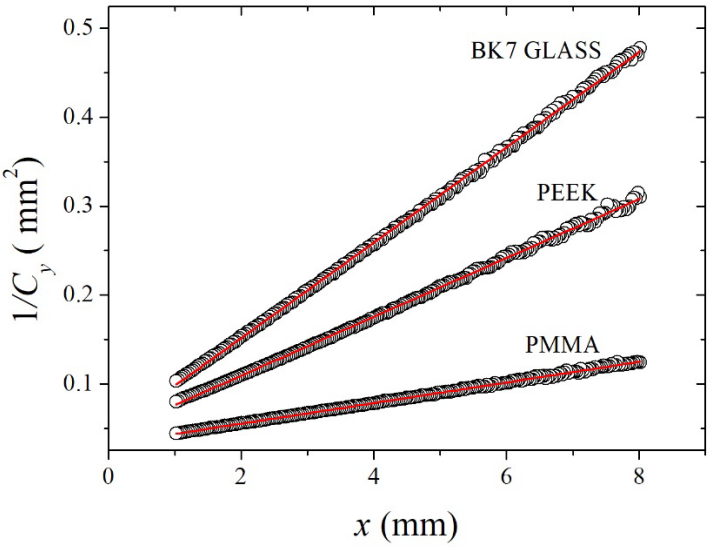

a)

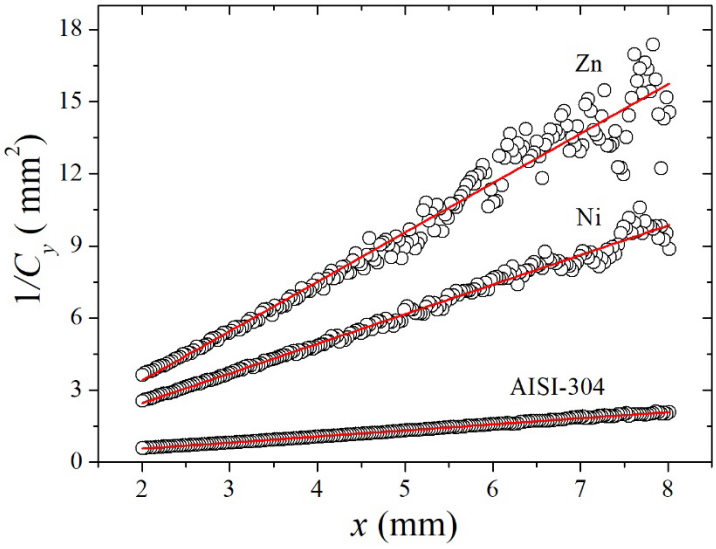

b)

Figure 6.10 Inverse of the parabolic coefficient versus the longitudinal distance for some of the calibrated materials used in this work. Dots are the experimental data and the continuous lines are the linear fits. a) Poor and b) good thermal conductors.

Tests on a piece of Balsa wood were done, which is a soft, low-density heterogeneous material. As its thermal transport properties are anisotropic, measurements have been performed in the direction perpendicular to the growth rings ($\perp$) and in the direction parallel ($\parallel$) to them. The retrieved values of the thermal diffusivity are given in Table 6.1. It is worth noting that for this heterogeneous material there are differences in the

physical properties from tree to tree depending on the age, climate and moisture [126,127]. That is the reason for the large dispersion of the literature values given in Table 6.1. Anyway, a thermal anisotropy factor above 2, similar to that found in this work, has been already reported [128].

Then, the central transverse profile method was tested. It was analysed on the same averaged thermograms as those used for the parabolas method. Figure 6.11a shows the central transverse profiles of $\ln(Ty)$ for a thick Zn sample and of $\ln(Ty^{0.5})$ for two thin plates (L = 0.2 mm) of Zn and AISI-304. Dots are the experimental data and the continuous lines are the linear fits. By applying Equation 6.2, the transverse thermal diffusivity is obtained. The results, which agree with the literature values, are summarized in Table 6.1.

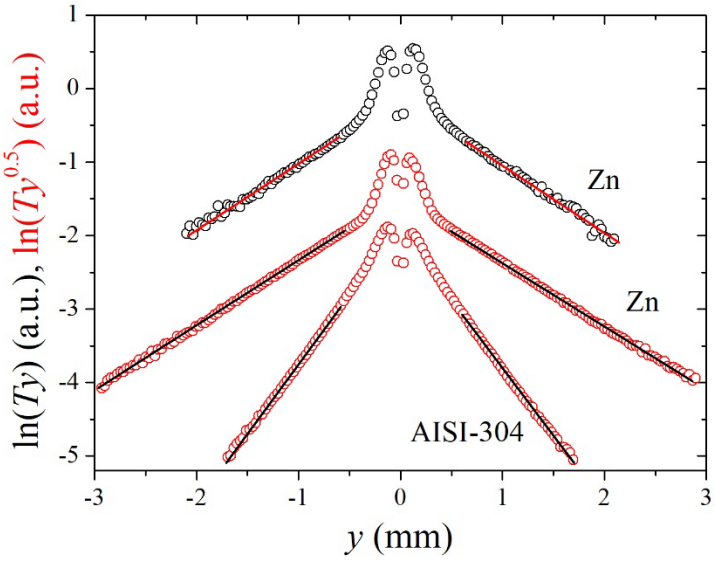

a)

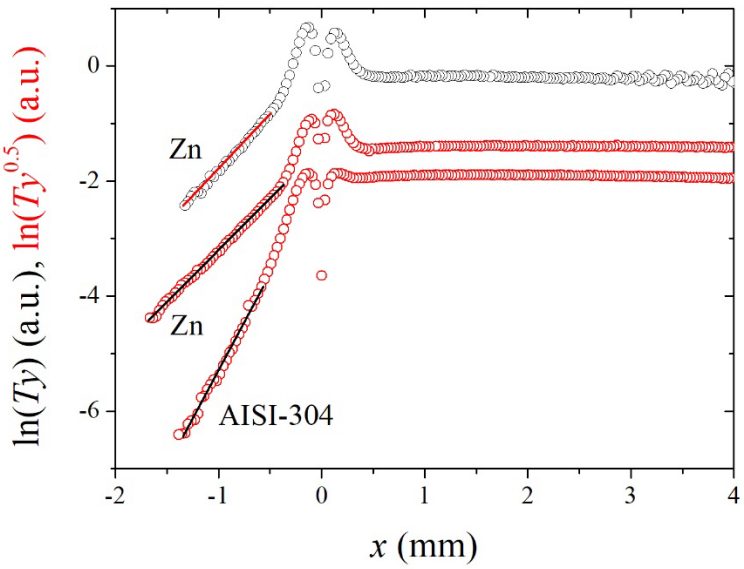

b)

Figure 6.11 a) Transverse profiles and **b**) longitudinal profiles in natural logarithm scale for thick Zn (black curve) and for thin Zn (L = 0.2 mm) and AISI-304 (L = 0.2 mm) in red. Dots are the experimental data while the continuous lines are the linear fits.

Finally, the central longitudinal profile method was tested. Figure 6.11b shows the longitudinal profiles of $\ln(Tx)$ and $\ln(Tx^{0.5})$ for the same three samples as in Figure 6.11a. Dots are the experimental data and the continuous lines are the linear fits. As predicted by the theory (see Figure 6.5), for $x > 0$ there is a flat behaviour without any information on the thermal diffusivity. For $x < 0$ there is a linear relation whose slope gives the longitudinal thermal diffusivity by applying Equation 6.3. The results are summarized in Table 6.1.

Table 6.1. Retrieved thermal diffusivities using the three methods proposed in this manuscript. The uncertainty varies from less than 3% for thermal insulators up to 5-6% for good thermal conductors.

Sample	α [$\times 10^{-6}$ m^2s^{-1}] (Parabolas method)	α [$\times 10^{-6}$ m^2s^{-1}] (Transverse profile)	α [$\times 10^{-6}$ m^2s^{-1}] (Longitudinal profile)	α [$\times 10^{-6}$ m^2s^{-1}] (Literature) [3,7,126, 127,128,129,130]
PEEK	0.19	-	-	0.18
AISI-304	4.0	4.0	4.1	4.0
Ni	21	22	20	22
Zn	43	43	40	42
Al 2024-T6	70	73	70	73
Balsa wood ∥	0.44	-	-	0.30-0.51
Balsa wood ⊥	0.22	-	-	0.14-0.25
Colored PMMA	0.12	-	-	0.11
BK7-glass	0.56	-	-	0.5-0.6
PEEK (L = 0.25 mm)	0.20	-	-	0.18
AISI-304 (L = 0.2 mm)	3.9	3.9	4.0	4.0
Ni (L = 0.2 mm)	-	20	20	22
Zn (L = 0.2 mm)	-	45	45	42

As can be observed in Table 6.1, no results are given for insulators using both central profiles methods. The reason for that is not a limitation of the method itself, but it is related to the lower velocity limit of our setup (1.5 cm/s). At this speed the number of points is too small to provide reliable thermal diffusivity values. For those materials either velocities of a few mm/s or a higher spatial resolution are needed.

Before concluding, let us remark some drawbacks of the methods proposed in this work. a) On the one hand, they are valid for quite big samples, since the steady state must have been reached. Anyway, as these methods are addressed to in-line production or in-line quality control processes, this is not a real limitation. b) On the other hand, the two central profiles methods require a high spatial resolution to have enough experimental data to clearly define the linear region. Accordingly, IR cameras with high resolution (640 × 512 pixels or higher) and/or microscope lenses, leading to a spatial resolution better than 30 μm, are highly recommended. Note that the parabolas method does not suffer from this limitation, since even with few data the second order coefficient of the parabolas can be obtained accurately [131]. c) Besides, the central

profiles methods are not valid when the thermal thickness of the specimen is intermediate, i.e. neither thick nor thin. This issue can be overcome by selecting, whenever it is possible, the appropriate velocity range: increasing the speed for the sample to behave as thick or reducing it to approach the thermally thin limit. d) One of the potential applications of these methods is to detect heterogeneities in-line production. This application requires local thermal diffusivity measurement methods. For this purpose, it is worth noting that the central profiles methods are preferable to the parabolas method since the former only requires taking temperature data a few millimetres around the laser spot, whereas the latter requires analysing the temperature along a centimetre or more in the direction of the sample movement.

6.5 Conclusions

In this work three methods to measure the in-plane thermal diffusivity of isotropic and anisotropic solids samples moving at constant velocity by analyzing the surface temperature field in logarithmic scale were proposed. These methods are based on simple linear relations, which avoid complex multiparametric fitting procedures. Moreover, they are valid not only for opaque samples, but also for semitransparent ones and they are not affected by heat losses by convection and radiation.

GENERAL CONCLUSION

It was demonstrated that the photoacoustic, the photopyroelectric and the IR thermography photothermal techniques are suitable for non-destructive characterization of materials in applications related to inspection, certification and quality control of products, which promote their use in the fields of agriculture, oil and manufacturing industry, as innovative methods or to support those already standardized and regulated. It has been shown that discrimination between organic and inorganic/conventional coffee farming is possible by means of the IR photoacoustic spectroscopy spectra and thermal effusivity values of oil extracted from coffee, being this thermophysical parameter measured by the front photopyroelectric technique. The same technique was used for thermal effusivity measurement in heptane/isooctane liquids mixtures. Using the thermal conductivity of these samples obtained by the transient hot wire technique, the thermal diffusivity and the heat capacity per unit volume were determined using well-known relationships existing between these parameters, so that a complete thermal characterization was possible. These parameters shown to be sensitive to the possible non-associative effects between the components of the mixtures. There is a correlation between the values of these parameters and the octane number, that suggest alternative ways for hydrocarbons rating. Lastly, the IR thermography technique was used to characterize vertical interface or cracks in a non-destructive way (sizing of the cracks and thermal conductivity determination of the fluid that they may contains) and for measurement of thermal diffusivity in samples in motion, so that this parameter could be introduced as a control criterion in production lines.

LIST OF PUBLICATIONS

1. A. Bedoya, S. Alvarado, A. Calderón, E. Marín, “Thermal transport properties of heptane-isooctane mixtures”. **Thermochimica Acta** 666, pp 190-196, 2018. **Q1** DOI: https://doi.org/10.1016/j.tca.2018.07.003

2. A. Bedoya, F. Gordillo-Delgado, Y.E. Cruz-Santillana, J. Plazas, E. Marin, “Thermal effusivity measurement of conventional and organic coffee oils via photopyroelectric technique”. **Food Research International**, 102, pp 419-424, 2017. **Q1** DOI: https://doi.org/10.1016/j.foodres.2017.09.013

3. J. González, A. Bedoya, A. Mendioroz and A. Salazar, “Measuring the thermal resistance of vertical interfaces separating two different media using lock-in infrared thermography with laser spot heating”. **International Journal of Thermal Sciences** 135, pp 410-416, 2018. **Q1** DOI: https://doi.org/10.1016/j.ijthermalsci.2018.09.026

4. A. Bedoya, J. González, J. Rodríguez-Aseguinolaza, A. Mendioroz, A. Sommier, J.C. Batsale and C. Pradere, A. Salazar, “Measurement of in-plane thermal diffusivity of solids moving at constant velocity using laser spot infrared thermography”. **Measurement** 134, pp 519-526, 2018. **Q1** DOI: https://doi.org/10.1016/j.measurement.2018.11.013

5. L. Gaverina, M. Bensalem, A. Bedoya, J. Gonzalez, A. Sommier, J.L. Battaglia, A. Salazar, A. Mendioroz, A. Oleaga, J. C. Batsale, C. Pradere, “Constant Velocity Flying Spot for the estimation of in-plane thermal diffusivity in anisotropic materials”. **International Journal of Thermal Science** 145, pp 1-13, 2019. **Q1** DOI: https://doi.org/10.1016/j.ijthermalsci.2019.106000

Publications pending acceptance

6. A. Bedoya, M. Colom, A. Mendioroz, A. Salazar, E. Marín, “Measurement of the thermal conductivity of fluids using laser spot lock-in thermography”. **Measurement (submitted for publication)**

7. M. Colom, A. Bedoya, A. Mendioroz, A. Salazar, “Measuring the in-plane thermal diffusivity of moving samples using laser spot lock-in thermography”. **International Journal of Thermal Science**. **(submitted for publication)**

Communications to conferences

8. A. Bedoya, J. González, A. Mendioroz and A. Salazar, “Measuring the thermal resistance of vertical interfaces separating two different media using lock-in infrared thermography with laser spot excitation”. **QIRT 2018 Proceedings**, pp 806-807, 2018. DOI: https://doi.org/10.21611/qirt.2018.100

9. A. Bedoya J. Gonzalez, A. Mendioroz, C. Pradere, A. Sommier, J.C. Batsale, A. Salazar, “Flying-spot thermography: measuring the in-plane (an)isotropic thermal diffusivity of large and complex parts”. **Proceedings Thermosense: Thermal Infrared Applications XLI** 11004, 2019. DOI: https://doi.org/10.1117/12.2518623

BIBLIOGRAPHICAL REFERENCES

[1] P.J. Shull, Nondestructive Evaluation Theory, Techniques, and Applications. 1st Edition, CRC Press, Boca Raton, 2002.

[2] F.P. Incropera, D.P. Dewitt, Fundamentos de transferencia de calor. 4th Edition. Prentice Hall, México, 1999.

[3] Y. A. Cengel, Transferencia de Calor y Masa, un enfoque práctico. 3rd Edition, McGraw-Hill, Mexico, 2007.

[4] J. Fourier, Theorie Analytique de La Chaleur. , Edition Jaques Gabay, France, 1988.

[5] J. H. Lienhard IV and J.H. Lienhard V, A Heat Transfer Textbook. 3rd Edition, Phlogiston Press, U.S.A., 2006.

[6] E. Marin, Thermal Wave Physics Photothermal Techniques: Basic Principles an Recent Developments-Basic principles of thermal wave physics and related techniques. Transworld Research Network, India, 2009.

[7] D. P. Almond, P. M. Patel, Photothermal Science and Techniques. 1st Edition, Chapman & Hall, London, 1996.

[8] E. Marín, Thermal Physics Concepts: The Role of the thermal Effusivity. The Physics Teacher 44, pp 432-434, 2006.

[9] A. Salazar, On thermal diffusivity. European Journal of Thermophysics 24, pp 351-358, 2003.

[10] G. Nibu, C. Vallabhan, V. Nampoori, A. George, P. Radhakrishnan, Open-cell photoacoustic investigation of the thermal effusivity of liquids crystals. Opt. Eng. 40 7, pp 1343-1347, 2001.

[11] N. W. Pech May, Analysis of the thermal properties of semitransparent materials and characterization of vertical cracks in opaque solids using infrared thermography. Thesis of Doctorate, Merida, Yucatan Mexico, September 2016.

[12] Manual of DSP Lock-in Amplifier, Model SR830-Standard Research Systems. https://www.thinksrs.com/downloads/pdfs/manuals/SR830m.pdf (Visited at 08-23-2019).

[13] A. G. Bell, Telephone United States Patent No 174, 1876.

[14] A. Rosencwaig, A. Gersho, Theory of the photoacoustic effect with solids. J. Appl. Phys, 47 1, pp 64-69, 1976.

[15] D. W. Vidrine, Photoacoustic Fourier Transform Infrared Spectroscopy of solid Samples. Applied Spectroscopy 34 3, pp 314-319, 1980.

[16] C. Sampaio Mangolim, C. Moriwaki, A. C. Nogueira, F. Sato, M. L. Baesso, A. Medina Nieto, G. Matioli, Curcumin-B-cyclodextrin inclusion complex: Satbility, slubility, characterization by FT-IR, FT-Raman, X-ray diffraction and photoacoustic spectroscopy, and food application. Food chemistry 153, pp 361-370, 2014.

[17] M. Pawlaczyk, S. Pasieczna-Patkowska J. Ryczkowski, G. Schroeder, Photoacoustic infrared spectroscopic studies of silica surface functionalized by dendrimers. Vibrational Spectroscopy 103, 2019.

[18] L.F. Perondi, L.C.M. Miranda, "Minimal-volume photoacoustic cell measurement of thermal diffusivity: Effect of the thermoelastic sample bending" J. Appl. Phys. 62 7 , pp 2955-2959, 1987.

[19] A. McDonald and G. C. Wetsel, Jr., "Generalized theory of the photoacoustic effect". J. Appl. Phys. 49 4, pp 2313-2322, 1978.

[20] S. O. Ferreira, C. Ying An, I.N. Bandeira, L.C.M. Miranda, "Photoacoustic measurement of the thermal diffusivity of $Pb_{1-x}Sn_xTe$ alloys". Phys. Rev. B. 39 11, pp 7967-7970, 1989.

[21] A. Bedoya, E. Marín, A.M. Mansanares, M.A. Zambrano-Arjona. I. Riech, A. Calderón, "On thermal characterization of solids by photoacoustic calorimetry: thermal diffusivity and linear thermal expansion coefficient". Thermochimica Acta 614, pp 52-58, 2015.

[22] M. Chirtoc, R.M. Candea, V. Mercea, Operation theory f pyroelectric detectors. I. A New physical model and the resulting operation modes. Ferroelectric 56, pp 283-291, 1984.

[23] H. Coufal, Photothermal spectroscopy using a pyroelectric thin film detector. Appl. Phys. Lett. 44, pp 59-61, 1984.

[24] A. Mandelis, Frequency-domain photopyroelectric spectroscopy of condensed phases (PPES): A new, simple and powerful spectroscopic technique. Chemical Physics Letters 108 4, pp 388-392, 1984.
[25] A. Mandelis, M.M. Zver, Theory of photopyroelectric spectroscopy of solids. Journal applied physics 57, p 4421-4430, 1985.
[26] M. Chirtoc, G. Mihailescu, Theory of the photopyroelectric method for investigation of optical and thermal material properties. Physical review B 40 14, pp 9606-9616, 1989.
[27] S. Delenclos, M. Chirtoc, A. H. Sahraoui, C. Kolinsky, J.M. Buisine, Assessment of calibration procedures for accurate determination of thermal parameters of liquids and their temperature dependence using the photopyroelectric method. Review of Scientific Instruments 73 7, pp 2773-2780, 2002.
[28] D. Dadarlat, M. Chirtoc, C. Neamtu, R.M. Candea, D. Bicanic, Inverse Photopyroelectric detection Method. Phys. Stat. sol. (a) K121, K231, 1990.
[29] D. Dadarlat, C. Neamtu, High Performance Photopyroelectric Calorimetry of Liquids. Acta Chim. Slov. 56, pp 225-236, 2009.
[30] C. Meola, Infrared thermography, recent advances and future trends. Bentham Science publishers. P 2012.
[31] G. M. Carlomagno and P. G. Berardi, Unsteady Thermotopography in Non-Destructive Testing, in Proc III Infrared Inf. Exch., C. Warren, St Louis, 1976.
[32] G. Busse, D. Wu, W. Karpen, Thermal wave imaging with phase sensitive modulated thermography, J. Appl. Phys. 71, pp 3962–3965, 1992.
[33] O. Breitenstein, M. Langenkamp, Lock-in Thermography Basics and Use for Functional Diagnostics of Electronic Components, Springer Science & Business Media, Berlin, 2013.
[34] B. Zhang, R.E. Imhof, Theretical analysis of the surface thermal wave technique for measuring the thermal diffusivity of thin slabs. Appl. Phys. A 62, pp 323-334, 1996.
[35] A. Mendioroz, R. Fuente-Dacal, E. Apiñaniz, and A. Salazar. Thermal diffusivity measurement of thin plates and filaments using lock-in thermography. Review of scientific instrument 80, p 074904, 2009.
[36] K. Martínez, E. Marín, C. Glorieux, A. Lara-Bernal, A. Calderón, G. Peña Rodríguez, R. Ivanov. Photothermal determination of the thermal diffusivity of low thermal conductivity solids by infrared radiometry in frequency domain: influence of convection-radiation heat losses." International Journal of Thermal Sciences 98, pp 202-207, 2015.
[37] N. W. Pech-May, A. Oleaga, A. Mendioroz, A.J. Omella, R. Celorrio, A. Salazar, Vertical Cracks characterization using lock-in thermography: I infinite cracks. Meas. Sci. Technol. 25 pp 1-10, 2014.
[38] F. Cernushi, A. Russo, L. Lorenzoni, A. Figari, In-plane thermal diffusivity evaluation by infrared thermography. Review of Scientific Intruments 72, pp 3988-3995, 2001.
[39] P. Bison, F. Cernushi, S. Capelli, A thermographic technique for the simultaneous estimation of in-plane and in depth thermal diffusivities of TBC. Surface & Coatings Technology 205, pp 3128-3133, 2011.
[40] N.W. Pech-May, A. Mendioroz, A. Salazar, Simultaneous measurement of the in-plane and in-depth thermal diffusivity of solids using pulsed infrared thermography with focused illumination, NDT&E Int. 77, pp 28–34, 2016.
[41] A. Bedoya, J. Gonzales, J. Rodriguez-Aseguinolaza, A. Mendioroz, A. Sommier, J.C. Batsale, C. Pradere, A. Salazar, Measurement of in-plane thermal diffusivity of solids moving at constant velocity using laser spot infrared thermography. Measurement 134, pp 519-526, 2019.
[42] B. Stalhane and S. Pyk, Ny Metod for Bestamning Av Varmelednings-Koefficienter. Teknisk TidsKrift 61, pp 389-398, 1931.
[43] S. Alvarado, E. Marin, A.G. Juarez, A. Calderon, R. Ivanov, A hot wire method based thermal conductivity measurement apparatus for teaching purposes. Eur. J. Phys. 33, pp 897-906, 2012.
[44] S. Alvarado, E. Marín, A. G. Juárez, A. Calderón, R. Ivanov, Sistema automatizado para la medición de la conductividad térmica de líquidos mediante el metodo del alambre caliente. Rev. Mex. Física, 57 3, pp 259-265, 2011.
[45] A. Perdih, F. Perih, Chemical Interpretation of Octane Number Acta Chim. Solv. 53, pp 306-315, 2006.

[46] S.L. Cardoso, M.G. da Silva, J.A.P. Lima, M.S. Sthel, E. Marin y H. Vargas, Application of the thermal wave resonator cavity sensor to the characterization of automotive fuels: motor octane number (MON), Anal. Sci. 17, pp 479-481, 2001.

[47] J. A. P. Lima, S. L. Cardoso, M. G. Silva, M. S. Sthel, C. E. N. Gatts, H. Vargas, L. C. M. Miranda, Thermal Diffusivity as an Automotive Fuel Characterization Parameter: Correlation with Motor Octane Number, Ind. Eng. Chem. Res. 40, pp 6207-6212, 2001.

[48] J. Shen and A. Mandelis, Thermal-wave resonator cavity, Rev. Sci. Instrum. 66, pp 4999 -5005, 1995.

[49] https://www.fishersci.es/es/es/brands/IPF8MGDA/jt-baker.html (Visited at 04-04-2019).

[50] https://www.sigmaaldrich.com/united-states.html (Visited at 04-04-2019).

[51] R.C. Reid, J.M. Prausnitz, B.E. Poling, The Properties of Gases and Liquids, McGraw Hill, New York, 1987.

[52] Piezo Film Sensors-Technical Manual, downloaded from https://www.te.com/usa-en/products/brands/meas.html?tab=pgp-story (visited at 10-03-2019).

[53] J.A.P. Lima, E. Marin, O. Correa, M. G. da Silva, S. L. Cardoso, C. Gatts, C. E. Rezende, H. Vargas, L.C.M. Miranda, Measurement of the thermal properties of liquids using a thermal wave interferometer,
Meas. Sci. Technol. 11, pp 1522—1526, 2000.

[54] GESTIS Substance Database of the Institute for Occupational Safety and Health. http://gestis-en.itrust.de/nxt/gateway.dll/gestis_en/010040.xml?f=templates$fn=default.htm$3.0
(Visited at 09-02-2019).

[55] J.A.P. Lima, E. Marín, M.G. da Silva, M.S. Sthel, S. L. Cardoso, D. Takeuti, C. Gatts, H. Vargas, C.E. Rezende, L.C.M. Miranda, On the use of the thermal wave resonator cavity sensor for monitoring hydrocarbon vapors, Rev. Sci. Instrum. 71, pp 2928-2932, 2000.

[56] H. Bendiab, G. Roux-Desgranges, A.H. Roux, J.P.E Grolier, D. Patterson, Excess heat capacities of ternary systems containing chlorobenzene or chloronaphthalene. J. Solution Chem. 23, pp 307-323, 1994.

[57] R. L. Rowley, S.C. Yi, D. Vernon-Gubler, J.M. Stoker, Mutual diffusivity, thermal conductivity, and heat of transport in binary liquid mixtures of alkanes in chloroform. J. Chem. Eng. Data 33, pp362-366, 1988.

[58] H. Watanabe, D.J. Seong, The Thermal Conductivity and Thermal Diffusivity of Liquid ***n***-Alkanes: C n H2n+2 (n=5 to 10) and Toluene. Int. J. Thermophys. 23, pp 337-356, 2002.

[59] H. Watanabe, Thermal Conductivity and Thermal Diffusivity of Sixteen Isomers of Alkanes: CnH2n+2 (n = 6 to 8). J. Chem. Eng. Data 48, pp 124-136, 2003.

[60] U.N. Gaitonde, D.D. Deshpande, S.P. Sukhatme, The Thermal Conductivity of Liquid Mixtures. Ind. Eng. Chem. Fund. 17, pp 321-325, 1978.

[61] J.C.G. Calado, J.M.N.A. Fareleira, C.A. Nieto de Castro, W.A. Wakeham, Thermal conductivity of five hydrocarbons along the saturation line. Int. J. Thermophys. 4, pp193-208, 1983.

[62] D.Y. Naziev, A.M. Aliev, Teplofiz. Vys. Temp. 30 (1992) 294.

[63] A. Sikorska, D. Dadarlat, B.B.J. Linde, M. Streza, C. Neamtu, A. Sliwinski, Photoacoustic and photopyroelectric investigations of thermal parameters in water mixed with organic liquids, J. Phys. IV France 137, pp 341-345, 2006.

[64] D. Dadarlat, C. Neamtu, V. Tosa, M. Streza, Accurate Photopyroelectric Calorimetry Applied to Isotopic Liquid Mixtures. Acta Chim. Slov. 54, pp149-153, 2007.

[65] M. Chirtoc, V. Tosa, D. Bicanic, P. Torfs, The Inverse Photopyroelectric Technique for the Measurement of Concentration and Transport Properties in Binary Systems: The Thermal Effusivity of Ethanol-Water Mixtures. Ber. Bunsenges. Phys. Chem. 95 7, pp 766 -769, 1991.

[66] C. Neamtu, D. Dadarlat, M. Chirtoc, A. Hadj Sahraoui, S. Longuemart, D. Bicanic, Evidencing Molecular Associations in Binary Liquid Mixtures via Photothermal Measurements of Thermophysical Parameters. Instrum. Sci. Technol. 34, pp 225-234, 2006.

[67] M. N. Pop, D. Dadarlat, M. Streza, V. Tosa, Photopyroelectric Investigation of Thermal Effusivity of Binary Liquid Mixtures by FPPE-TWRC Method. Acta Chim. Slov. 58, pp 549-554, 2011.

[68] A. O. Guimaraes, F.A.L. Machado, E.C. da Silva, A.M. Mansanares, Investigating thermal properties of biodiesel/diesel mixtures using photopyroelectric technique. Thermochi. Acta 527, pp 125-130, 2012.
[69] T. Gomiero, D. Pimentel, M.G Paoletti, Environmental impact of different agricultural management practices: Conventional vs. organic agriculture. Critical Reviews in Plant Sciences, 30 1–2, pp 95–124, 2011.
[70] D. Gabriel, S.M. Sait, W.E. Kunin, T.G. Benton. Food production vs. biodiversity: Comparing organic and conventional agriculture. Journal of Applied Ecology 50 2, pp 355–364, 2013.
[71] L. Kleemann, A. Abdulai, M. Buss. Certification and access to export markets: Adoption and return on investment of organic-certified pineapple farming in Ghana. World Development 64, pp 79–92, 2014.
[72] W.B. Sunarharum, D.J. Williams, H.E. Smyth. Complexity of coffee flavor: A compositional and sensory perspective. Food Research International 62, pp 315–325, 2014.
[73] L.F. Guedes Pinto, T. Gardner, C.L. McDermott, K.O. Lara Ayub. Group certification supports an increase in the diversity of sustainable agriculture network–rainforest alliance certified coffee producers in Brazil. Ecological Economics 107, pp 59–64, 2014.
[74] F. Gordillo-Delgado, E. Marín, D.M. Cortes-Hernández, C. Mejía-Morales, A. J. García-Salcedo. Discrimination of organic coffee via Fourier transform infraredphotoacoustic spectroscopy. Journal of the Science of Food and Agriculture 92 11, pp 2316–2319, 2012.
[75] R. Rasool, S.S. Kukal, G.S. Hira. Soil organic and physical properties as affected by long-term application of FYM and inorganic fertilizers in maize-wheat system. Soil & Tillage Research 101 1–2, pp 31–36, 2008.
[76] M.I. Saldaña y Hernandez, R. Gomez-Alvarez, M. Rivera-Cruz, J.D. Alvarez-Solis, J.M. Pat-Fernandez, C.F. Ortiz-Garcia. Influencia de abonos orgánicos en las propiedades químicas de la suelos y producción de Alpinia purpurata. Ciencia e Investigación Agraria 41 2, pp 215–224. 2014.
[77] I. Telci, O.G. Toncer, N. Sahbaz. Yield, essential oil content and composition of Coriandrum sativum varieties (var. vulgare Alef and var. microcarpum DC.) grown in two different locations. Journal of Essential Oil Research 18 2, pp 189–193, 2011.
[78] E. Marín. The role of thermal properties in periodic time-varying phenomena. European Journal of Physics 28, pp 429–445, 2007.
[79] D. Dadarlat, J. Gibkes, D. Bicanic, A. Pasca. Photopyroelectric (PPE) measurement of thermal parameters in food products. Journal of Food Engineering 30 (1–2), pp 155–162, 1996.
[80] G. Szafner, D. Bicanic, R. Kulcsar, O. Doka. Direct measurement of thermal effusivity of foods by front configuration of the photopyroelectric method. Journal of Food Physics 26, pp 4–10, 2013.
[81] M. Chirtoc, I. Chirtoc, D. Bicanic, J. Pelzl. Photopyroelectric (PPE) spectroscopy: Absorption, transmission, or reflectance?. Ferroelectrics 165, pp 27–38, 1995.
[82] L.M. Cervantes-Espinosa, F.D.L. Castillo-Alvarado, G. Lara-Hernández, A. Cruz-Orea, C. Hernández-Aguilar, A. Domínguez-Pacheco. Thermal effusivity of vegetable oils obtained by a photothermal technique. International Journal of Thermophysics 35, pp 1940–1945, 2014.
[83] S. Longuemart, A. Garcia-Quiroz, D. Dardalat, A. Hadj-Sahraoui, C. Kolinsky, J. Marc-Buisine, C. Neamtu. An application of the front photopyroelectric technique for measuring the thermal effusivity of some foods. Instrumentation Science & Technology 30 2, pp 157–165, 2002.
[84] F.A.L. Machado, E.B. Zanelato, A.O. Guimares, E.C. da Silva, A.M. Mansanares. Thermal properties of biodiesel and their corresponding precursor vegetables oils obtained by photopyroelectric methodology. International Journal of Thermophysics 33, pp 1848–1855, 2012.
[85] G.H. Dunteman. Principal components analysis. Sage University paper series on quantitative application in the social sciences, series no. 07-069. Newbury Park, CA: Sage, 1989.
[86] K. Wojcicki, I. Khmelinskii, M. Sikorski, E. Sikorska. Near and mid infrared spectroscopy and multivariate data analysis in studies of oxidation of edible oils. Food Chemistry 187, pp 416–423, 2015.
[87] J. Montilla-Pérez, J. Arcila-Pulgarín, M. Aristizábal-Loaiza, E.C. Montoya-Restrepo, C.I. Puerta-Quintero, C.E. Oliveros-Tascón, G. Cadena-Goméz. Caracterización de algunas

propiedades físicas y factores de conversión del café durante el proceso de beneficio húmedo tradicional. Cenicafé 59 2, pp 120–142, 2008.

[88] Z. Al-Hamamre, S. Foerster, F. Hartmann, M. Kroger, M. Kaltschmitt. Oil extracted from spent coffee grounds as a renewable source for fatty acid methyl ester manufacturing. Fuel 96, pp 70–76, 2012.

[89] NTC 336 (2016). Grasas y aceites animales y vegetales. Método de la determinación de la densidad (masa por volumen convencional). https://tienda.icontec.org/producto/ntc336-2/?v=0b98720dcb2c (Visited at 09-03-2019).

[90] NTC 218 (2011). Grasas y aceites vegetales y animales. Determinación del índice de acidez y de la acidez. https://tienda.icontec.org/producto/ntc218-2/?v=0b98720dcb2c (Visited at 09-03-2019).

[91] NTC 4967 (2014). Grasas y aceites animales y vegetales. Cromatografía de gases de esters metílicos de ácidos grasos. parte 2: Preparación de esteres metílicos de ácidos grasos. https://tienda.icontec.org/producto/ntc4967/?v=0b98720dcb2c (Visited at 09-03-2019).

[92] J.F. McClelland, R.W Jones, L.M. Seaverson. A practical guide to FTIR photoacoustic spectroscopy. FT-IR photoacoustic spectroscopy. pp. 2–22, 1992. http://www.mtecpas.com/Docs/Prac%20Guide%20to%20FTIR%20Photoacoustic.pdf (Visited at 09-03-2019).

[93] A.B.A. de Azevedo, T.G Kieckbush, A.K. Tashima, R.S. Mohamed, P. Mazzafera, S.A.B. Vieira de Melo. Extraction of green oil using supercritical carbon dioxide. Journal of Supercritical Fluids 44, pp 186–192, 2008.

[94] M.M.R. de Melo, H.M.A. Barbosa, C.O. Pasos, C.M. Silva. Supercritical fluid extraction of spent coffee grounds: Measurement of extraction curves, oil characterization and economic analysis. Journal of Supercritical Fluids 86, pp 150–159. 2014.

[95] N.S. Caetano, V.F.M. Silva, T.M. Mata, T. M. Valorization of coffee grounds for biodiesel production. Chemical Engineering Transactions 26, pp 267–272, 2012.

[96] A. Deligiannis, A. Papazafeiropoulou, G. Anastopoulos, F. Zannikos. Waste coffee grounds as an energy feedstock. Proceedings of the 3rd international CEMEPE & SECOTOX conference, Skiathos, Greece, pp. 617–622, 2011.

[97] L.S. Oliveira, A.S. Francia, J.C.F. Mendoca, M.C. Barros-Junior. Proximate composition and fatty acids profile of green and roasted defective coffee beans. LWT-Food Science and Technology 39 3, pp 235–239, 2006.

[98] E. Alexa, A. Dragomirescu, G. Pop, C. Jianu, D. Dragos. The use of FT-IR spectroscopy in the identification of vegetable oils adulteration. Journal of Food, Agriculture and Environment 7 2, pp 20–24, 2009.

[99] Q. Zhang, C. Liu, Z. Sun, X. Hu, Q. Shen, J. Wu. Authentication of edible vegetable oils adulterated with used frying oil by Fourier transform infrared spectroscopy. Food Chemistry 132, pp 1607–1613, 2012.

[100] D.N. Raba, M.A. Poiana, A. Breica-Borozan, M. Stef, F. Radu, M.V Popa. Investigation on crude and high-temperature heated coffee oil by ATR-FTIR spectroscopy along with antioxidant and antimicrobial properties. PloS One, 10 9, 1–20,2015.

[101] B.M. Elliot, K. Sung, C.E. Miller. FT-IR spectra of ^{18}O-, and ^{13}C-enriched CO_2 in the v_3 region: High accuracy frequency calibration and spectroscopic constants for $^{16}O^{12}C^{18}O$, $^{18}O^{12}C^{18}O$, and $^{16}O^{13}C^{16}O$. Journal of Molecular Spectroscopy 312, pp 78–86, 2015.

[102] A.P. Craig, A.S. Franca, L.S. Oliveira, J. Irudayaraj, K. Ileleji. Application of elastic net and infrared spectroscopy in the discrimination between and non-defective roasted coffees. Talanta 128, pp 393–400, 2014.

[103] J.V. Link, A.L. Guimaraes-Lemes, I. Marquetti, M.B. dos Santos-Scholz, E. Bona. Geographical and genotypic classification of Arabica coffee using Fourier transform infrared spectroscopy and radial-basis function networks. Chemometrics and Intelligent Laboratory Systems 135, pp 150–156, 2014.

[104] O. Kazeem, O. Taiwo, A. Kaeem, D. Mondiu. Determination of some physical properties of castor (Ricirus communis) oil. International Journal of Scientific Engineering and Technology, 3 12, pp 1503–1508, 2014.

[105] E.J. Kubiak, Infrared detection of fatigue cracks and other near-surface defects. Appl. Opt. 7 9, pp 1743–1748, 1968.

[106] A. Mendioroz, K. Martinez, R. Celorrio, A. Salazar. Characterizing the shape and heat production of open vertical cracks in burst vibrothermography experiments. NDT and E International 102, pp 234-243, 2019.
[107] S. D. Holland. Thermographic signal reconstruction for vibrothermography. NDT and E International 44 8, pp 736-739, 2011.
[108] B. Oswald-Tranta, Thermoinductive investigations of magnetic materials for surface cracks, QIRT J. 1, pp 33–46, 2004.
[109] P. Jackel, U. Netzelmann, The influence of external magnetic fields on crack contras in magnetic steel detected by induction thermography, QIRT J. 10 (2013) 237–247.
[110] K.R. Grice, L.J. Inglehart, L.D. Favro, P.K. Kuo, R.L. Thomas, Thermal wave imaging of closed cracks in opaque solids, J. Appl. Phys. 54, pp 6245–6255, 1983.
[111] T. Li, P. Almond, D. Andrew, S. Rees, Crack imaging by scanning pulsed laser spot thermography, NDT&E Int. 44, pp 216–225, 2011.
[112] J. Schlichting, C. Maierhofer, M. Kreutzbruck, Crack sizing by laser excited thermography, NDT&E Int. 45 1, pp 133–140, 2012.
[113] M. Streza, Y. Fedala, J.P. Roger, G. Tessier, C. Boue, Heat transfer modelling for surface crack depth evaluation, Meas. Sci. Technol. 24, 045602, 2013.
[114] W. A. Wakeham, M. J. Assael, Thermal conductivity measurement, In: Measurement, Instrumentation, and Sensors Handbook, J. G. Webster and H. Eren, CRS Press, 66, 2018.
[115] R.H. Bogaard, Thermal Conductivity of Selected Stainless Steels, In: Ashworth T., Smith D.R. (eds) Thermal Conductivity 18. Springer, Boston, MA, pp 175-185, 1985.
[116] C.L. Choy, K.W. Kwok, W.P. Leung, F. P. Lau, Thermal conductivity of Poly (ether Ether Ketone) and its Short-Fiber Composites, J. Polym. Sci. Pol. Phys. 32, pp 1389-1397, 1994.
[117] R.H. Bogaard, P.D. Desai, H. H. Li, C. Y. Ho, Thermophysical properties of stainless steel, Themochim. Acta 218, pp 373-393, 1993.
[118] P.J. Shaw, D.J. Rawlins, The point-spread function of a confocal microscope: its measurement and use in deconvolution of 3-D data, J. Microsc. 163, pp 151–165,1991.
[119] Reported thermal conductivities of materials measured by different techniques can span a wide percentual range, as can be see for example in Y. S. Touloukian et al. Thermophysical properties of matter, v. 1. Thermal conductivity: metallic elements and alloys, (IFI/PLENUN: NY, 1970)
[120] H. Xie, J. Wang, T. Xi, Y.Liu, F. Ai, Q. Wu, Thermal conductivity enhancement of suspensions containing nanosized alumina particles. J. Appl. Phys. 91 7, pp 4568-4572, 2002.
[121] B. Abad, D.A. Borca-Tasciuc, M.S. Martin-Gonzalez, Non-contact methods for thermal properties measurements, Renew. Sustain. Energy Rev. 76, pp 1348–1370, 2017.
[122] L. Gaverina, J.C. Batsale, A. Sommier and C. Pradere, Pulsed flying spot with the logarithmic parabolas method for the estimation of in-plane thermal diffusivity fields on heterogeneous and anisotropic materials, J. Appl. Phys. 121, pp 115105, 2017.
[123] E.J. Kubiak, Infrared detection of fatigue cracks and other near-surface defects, Appl. Opt. 7, pp 1743–1747, 1968.
[124] L. Gaverina, A. Sommier, J.L. Battaglia, J.C. Batsale, C. Pradere, Pulsed flying spot elliptic method for the estimation of the thermal diffusivity field of orthotropic materials, Int. J. Therm. Sci. 125, pp 142–148, 2018.
[125] A. Thiam, J.C. Kneip, E. Cicala, Y. Caulier, J.M. Jouvard, S. Mattei, Modeling and optimization of open crack detection by flying spot thermography, NDT&E Int. 89, pp 67–73, 2017.
[126] N.J. Kotlarewski, B. Ozarska and B.K. Gusamo, Thermal conductivity of Papua New Guinea balsa wood measured using the needle probe procedure, Bioresources 9, pp 5784-5793, 2014.
[127] R. Hrčka, Variation of thermal properties of beech wood in the radial direction with moisture content and density, in Wood Structure and Properties 10, Ed. J. Kúdela and R. Lagana, Arbora Publishers, Zvolen, Slovakia, pp 111-116, 2010.
[128] P.Niemz, W. Sonderegger and S. Hering, Thermal conductivity of Norway spruce and European beech in the anatomical directions, Annals of Warsaw University of Life Sciences, Forestry and Wood Technology 72, pp 66-72, 2010.
[129] Goodfellow catalogue at http://www.goodfellow.com (Visited at 09-29-2019).
[130] L.R. Touloukian, R.W. Powell, C.Y. Ho and M.C. Nicolasu, Thermal Diffusivity (IFI/Plenum, New York, 1973).

[131] L. Gaverina, M. Bensalem, A. Bedoya, J. González, A. Sommier, J.L. Battaglia, A. Salazar, A. Mendioroz, A. Oleaga, J.C. Batsale and C. Pradere, Constant Velocity Flying Spot for the estimation of in-plane thermal diffusivity on anisotropic materials. International Journal of Thermal Sciences 145, 106000, 2019.